MINISTRY OF EDUCATION AND SCIENCE OF UKRAINE

ODESSA STATE ACADEMY OF CIVIL ENGINEERING AND ARCHITECTURE

Pysarenko A. N.

APPLICATION OF WAVELET TRANSFORMS FOR INHOMOGENEOUS STRUCTURES

Monograph

2024

UDC 539.3

Author:

A.N. Pysarenko, Associate Professor, Head of the Department of Physics of Odessa State Academy of Civil Engineering and Architecture

Reviewers:

A. Gokhman Professor of the Department of Applied Mathematics and Informatics of South Ukrainian National Pedagogical University named after K.D. Ushynsky

V. Goczul'skij Professor, Head of the Department of Physics and Astronomy of Odessa I.I. Mechnikov National University,

Recommended for publication by the Academic Council of Odessa State Academy of Civil Engineering and Architecture

(protocol No. dated April 12, 2024.)

Application of wavelet transforms for inhomogeneous structures [Monograph] / A.N. Pysarenko, Odesa: OSACEA, 2024. 134 p.

The monograph examines the theoretical and experimental aspects of wavelet analysis of deformation fields of laminar composites. The results of pulsed impact of acoustic emission on samples of fiber-filled composites are analyzed in detail. The features of using wavelets to detail the space of intra-volume damage have been studied. Modifications of the Haar wavelet transform are presented as a basis for the study of functionally graded composite structures. A comparative analysis of wavelet transformation techniques for describing the dynamic response and simulating damage in laminated piezoelectric composites was carried out. Spectral dependences are presented for symmetric and asymmetric modes of Lamb waves in laminated composites. The monograph is intended for specialists in the field of wavelet analysis, materials science and physics of composite materials.

CONTENTS

PREFACE

Industrial composite materials consist of a large number of microstructural components with different characteristics, the combination of which determines the properties of the material as a whole. The processes occurring in composite materials are described by differential equations with rapidly oscillating coefficients, the numerical solution of which requires significant computational effort, since it involves the use of a very small grid size.

This led to the development of a new area of mathematical research, the goal of which is to construct methods for averaging partial differential operators such that the solutions of the resulting equations with averaged coefficients are close to the solutions of the original equations and adequately describe the behavior of the composite. The averaged (effective) characteristics of composite materials are determined experimentally or numerically, and there are also a number of analytical estimates.

Existing analytical estimates of the properties of composites (for example, Hashin-Shtrikman estimates and Voigt-Reuss estimates for elastic constants, thermal and filtration properties), as a rule, provide a fairly wide range of possible values of material properties and can only be used for rough estimates.

Currently, numerical methods have been developed for obtaining effective characteristics of materials with a periodic structure in problems of linear elasticity, thermal conductivity, diffusion, etc. - this is the asymptotic averaging technique.

However, in this case it is necessary to solve problems in the class of functions that are periodic on a cell, which complicates the implementation of this method.

Only in the case of a certain symmetry of the sample and material under study can periodic boundary conditions be replaced by non-periodic boundary conditions. The insufficiency of classical averaging methods encourages the development of new mathematical approaches. The basis of one of the approaches was the use of wavelets - a class of basis functions that are used in digital signal processing, information compression, pattern recognition, etc.

One of the main advantages of the wavelet transform is the ability to obtain a representation of quantities at the scale level of interest. Using the wavelet transform, an averaged representation of the function is obtained (coarse scale - “low resolution”) and its local components are isolated (fine scale - “high resolution”). This transformation property allows the introduction of multiscale or variable resolution analysis of the function under study.

The properties of wavelets suggest that the wavelet transform will also be useful in averaging solutions to partial differential equations.

This work is devoted to some basic wavelet analysis methods used to diagnose the spatial structure and analyze the dynamics of mass and energy flows of composites.

The first chapter deals with the analysis of general features and problems of using continuous and discrete wavelet transforms.

The second chapter is devoted to the peculiarities of using acoustic sounding of composite structures and subsequent wavelet processing.

The use of wavelets for identifying damage in composite structures is discussed in the third chapter.

Features of the use of Haar wavelets in the study of compositional structures are discussed in the fourth chapter.

An analysis of the specifics of using wavelet transformations for the study of composite materials is given in the fifth chapter.

The sixth chapter is devoted to the theoretical and experimental study of composites using Lamb waves.

CHAPTER 1
INTRODUCTION

The term "wavelet" was introduced by Grossman & Morlet in the mid-80s in connection with the analysis of the properties of seismic and acoustic signals [1]. The subject of the study was signal analysis, and the set of basis functions was redundant. Meyer showed the existence of wavelets that form an orthonormal basis in L^2 *(R)* [2]. Discretization of the wavelet transform was described in Daubechies' paper [3], which built a bridge between mathematicians and signal processing specialists. Daubechies developed a family of wavelet filters that have maximum smoothness for a given filter length. The popularity of wavelets increased after Mallat introduced the concept of multiple-scale analysis [4]. He was apparently the first to use wavelets for image encoding. Some ideas of wavelet theory were partially developed a very long time ago. For example, Haar published a complete orthonormal system of basis functions with local domain in 1910. These functions are now called Haar wavelets [5].

The word wavelet (from the French “ondelette”) literally translates as “short (small) wave. Despite the fact that the theory of wavelet transform has already been largely developed, there is, as far as is known, no precise definition of what a “wavelet” is and what functions can be called wavelets. Usually, wavelets are understood as functions whose shifts and dilations form the basis of many important spaces, including L^2 *(R)*. These functions are compact in both the time and frequency domains. Wavelets are directly related to multi-scale signal analysis.

The continuous wavelet transform T_f is the scalar product of *f(x)* and basis functions

$$\psi_{a,b}(x)\,\psi^{-1}(x') = \sqrt{a}\,,\ a \in R^{+},\ b \in R\,,\ x' = ax + b\,, \tag{1.1}$$

so

$$T_f(a,b) = \sqrt{a}\int_{-\infty}^{+\infty}\psi(x')\,f(x)dx. \tag{1.2}$$

The basis functions $\psi_{a,b} \in L^2(R)$ are real and oscillate around the *x*-axis. They are defined over a certain interval. These functions are called wavelets and can be thought of as scaled and shifted versions of the prototype function $\psi(x)$.

When analyzing signals, it is often useful to represent a signal as a set of its successive approximations. For example, when transmitting a signal, you can first transmit a rough version of it, and then successively refine it. This transfer strategy is beneficial, for example, when selecting signals from a database, when you need to quickly scan a large number of files.

In most applications we deal with discrete signals. Therefore, from a practical point of view, discrete analogs are of interest, which convert a discrete signal into continuous and discrete signals, respectively.

Wavelet analysis is a rapidly developing technique that covers such practical applications as pattern recognition problems, processing and synthesis of various signals, image analysis of various natures, studying the properties of turbulent fields, convolution (packing) of large amounts of information, and in many other cases.

In many areas, significantly better results can be expected by using wavelets. Let's list some of them: the use of wavelet transform for signal compression, the use of wavelet transform for multiple-scale curves, the use of wavelet transform for surfaces, wavelets are successfully used in quantum physics, in the study of atomic structure, in laser technology, problems of analysis of non-stationary signals (this kind of problem arises in medicine (tomography, electrocardiography), hydroacoustics and other fields), removing noise from noisy signals.

Wavelets can be orthogonal, semi-orthogonal, biorthogonal. These functions can be symmetrical, asymmetrical or non-symmetrical. There are wavelets with a compact domain of definition and those without one. Some functions have an analytical expression, others have a fast algorithm for calculating the associated wavelet transform. Wavelets also differ in the degree of smoothness. For practice, it would be desirable to deal with orthogonal symmetric (asymmetric) wavelets.

It seems important to carry out a preliminary comparative analysis of the Fourier and wavelet transforms. The wavelet transform of a one-dimensional signal consists of its expansion into a basis constructed from a soliton-like function (wavelet) with certain properties through scale changes and translations. Each function of this basis can be characterized as a certain spatial (temporal) frequency and its localization in physical space-time. Thus, in contrast to the Fourier transform traditionally used for signal analysis, the wavelet transform provides a two-dimensional sweep of the one-dimensional signal under study. A necessary condition for such a procedure is to consider frequency and position as independent variables. As a result, it becomes possible to analyze the properties of a signal simultaneously in physical (time, coordinate) and frequency spaces.

The scope of application of wavelets is not limited to the analysis of the properties of signals and fields of various natures obtained numerically, experimentally, or through observations. Wavelets are beginning to be used for direct numerical modeling - as a hierarchical basis well suited for describing the dynamics of complex nonlinear processes characterized by the interaction of disturbances in wide ranges of spatial and temporal frequencies.

The results of numerous experiments indicate that at large values of the Reynolds number, a significant part of the volume of the turbulent fluid remains passive with respect to energy dissipation and, consequently, with respect to its inverse cascade. Wavelet analysis turns out to be very convenient for analyzing

processes with intermittency. This analysis allows us to identify the spatiotemporal properties of the object being studied, determine the presence of intermittency and the distribution of dissipation regions, and obtain local high-frequency and global large-scale information about the object.

Processing short high-frequency signals or signals with localized frequencies is a difficult procedure. The wavelet transform turns out to be a convenient tool for adequately deciphering such data, since the elements of its basis are well localized and have a moving time-frequency window.

Another example is the application of the wavelet transform to the turbulent velocity field in a wind tunnel at high Reynolds numbers, which for the first time provided visual confirmation of the presence of the Richardson cascade.

The application of wavelet analysis to invariant measures of some well-known dynamical systems that model the situations of transition to chaos observed in dissipative systems turned out to be even more effective.

For practical application, it is important to know both the basic definition and the characteristics that a function must have in order to be a wavelet.

Any localized R- function $\psi \in L^2(R)$ is called a wavelet if for it there is a function $\psi^* \in L^2(R)$ such that the families $\{\psi_{jk}\}$ and $\{\psi^*_{jk}\}$, constructed according to the relations

$$\psi_{jk}(t) = 2^{j/2}\psi\left(2^j t - k\right), \quad \left\|\psi_{jk}\right\|_2 = \left\|\psi\right\|_2 = 1, \quad j,k \in I \tag{1.3}$$

$$\psi^{jk}(t) = \psi^*{}_{jk}(t) = 2^{j/2}\psi^*\left(2^j t - k\right), \; j,k \in I \tag{1.4}$$

are paired bases of the function space $L^2(R)$.

Each wavelet ψ, defined in this way, regardless of whether it is orthogonal or not, allows any function $f \in L^2(R)$ to be represented as a series

$$f(t) = \sum_{j,k=-\infty}^{\infty} c_{jk}\psi_{jk}(t). \tag{1.5}$$

whose coefficients are determined by the integral wavelet transform f with respect to ψ^*.

The orthogonality of the wavelet and the presence of an orthogonal basis presupposes the following relations: $\psi^* \equiv \psi$, $\{\psi_{jk}\} \equiv \{\psi^*_{jk}\}$.

For many practical purposes, it is sufficient that the wavelet ψ has the property of semi-orthogonality, i.e. so that its Riesz basis $\{\psi_{jk}\}$ satisfies the condition $\langle \psi_{jk}, \psi_{lm} \rangle = 0$ for $j = l,\ j, k, l, m \in I$.

A wavelet is called non-orthogonal if it is not a semi-orthogonal wavelet. However, being an *R*-wavelet, it has an analogue ψ^* and the pair (ψ, ψ^*) allows us to form families $\{\psi_{jk}\}$ and $\{\psi^*_{jk}\}$, that satisfy the biorthogonality condition $\langle \psi_{jk}, \psi_{lm} \rangle = \delta_{jl}\delta_{km}$, $j, k, l, m \in I$ and allowing to construct a full-fledged wavelet series and reconstruction formula.

Most of the restrictions imposed on the wavelet are associated with the need to have an inverse wavelet transform (or reconstruction formula).

he wavelet transform, unlike the Fourier transform, uses a localized basis function. The wavelet must be localized both in time and in frequency.

Often for practical use it turns out to be necessary that not only the zero

$$\int_{-\infty}^{\infty} \psi(t)dt = 0 \tag{1.6}$$

but also all the first *m* moments

$$\int_{-\infty}^{\infty} t^m \psi(t)dt = 0 \tag{1.7}$$

were equal to zero.

Such a wavelet is called a wavelet of order *m*. Wavelets with a large number of zero moments allow, ignoring the most regular polynomial components of the signal, to analyze small-scale fluctuations and high-order features.

An assessment of such a necessary property as localization and boundedness of a wavelet can be presented in the following form

$$|\psi(t)| < \left(1 + |t|^n\right)^{-1} \tag{1.8}$$

or

$$|\hat{\psi}(\omega)| < \left(1 + |k - \omega_0|^n\right)^{-1}, \tag{1.9}$$

where ω_0 is the dominant frequency of the wavelet, the number n should be as large as possible.

A characteristic feature of a wavelet transform basis is its self-similarity. All wavelets of a given family $\psi_{lm}(t)$ have the same number of oscillations as the basic wavelet $\psi(t)$.

As an orthogonal discrete wavelet generating an orthonormal basis, we can specify the Haar wavelet

$$\psi^{H}(t)=\begin{cases}1, & 0\le t<1/2\\ -1, & 1/2\le t<1\\ 0, & t<0,\ t\ge 1\end{cases} \tag{1.10}$$

The disadvantages of this wavelet are its non-smoothness, i.e. the presence of sharp boundaries in *t*-space. As a result, there is no symmetry of shape in *k*-space and infinite (decreasing as k^{-1}) «tails» appear. However, for some analysis tasks these disadvantages are insignificant, and sometimes the one-sidedness of the wavelet even becomes an advantage.

Often, a very similar, also discrete, but symmetrical *FHAT* wavelet is used to describe the signal function

$$\psi(t)=\begin{cases}1, & |t|\le 1/3\\ -1/2, & 1/3<|t|\le 1\\ 0, & |t|>1\end{cases} \tag{1.11}$$

$$\hat{\psi}(k)=3\Theta(k)\left(\frac{\sin k}{k}-\frac{\sin 3k}{3k}\right), \tag{1.12}$$

where Θ(k) is the Heaviside function (Θ(k) = 1 for k > 0 and Θ(k) = 0 for k ≤ 0.

The *FHAT* wavelet, which is irregular in time space and does not decay quickly enough in frequency space, and the *LP* wavelet (Littlewood & Paley), on the contrary, which has sharply defined boundaries in *k*-space and does not decay quickly enough in *t*-space, can be considered as intermediate cases between which Almost all wavelets are found.

The wavelet transform can be thought of as a dot product that analyzes the wavelet at a given scale and the signal being analyzed. The choice of analyzing wavelet is usually determined by what information needs to be extracted from the signal. Each wavelet has characteristic features both in time and in frequency space, so sometimes with the help of different wavelets it is possible to more fully identify and emphasize certain properties of the analyzed signal.

Real bases are quite often constructed on the basis of derivatives of the Gaussian function

$$\psi_m(t) = (-1)^m \partial_t^m \left[\exp\left(-\frac{t^2}{2} \right) \right], \tag{1.13}$$

$$\hat{\psi}_m(k) = m(ik)^m \exp\left(-\frac{t^2}{2} \right), \tag{1.14}$$

where $\partial_t^m = \partial^m [\ldots]/\partial t^m$, $m \geq 1$.

Higher derivatives have more zero moments and allow you to extract information about higher order features of the signal.

In particular, the parameters $m = 1$ and $m = 2$ can be associated with a *MHAT* wavelet. The *MHAT* wavelet has a narrow energy spectrum and two moments equal to zero (zero and first). These circumstances make it possible to analyze complex signals. The *MHAT* wavelet generalized to the two-dimensional case is often used to analyze isotropic fields. Calculating the derivative in only one direction results in a non-isotropic basis with good angular selectivity.

The well-known *Dog* wavelet is also constructed based on the Gaussian function

$$\psi(t) = \exp\left(-\frac{|t|^2}{2} \right) - 0.5\exp\left(-\frac{|t|^2}{8} \right), \tag{1.15}$$

$$\hat{\psi}(k)\frac{1}{(2\pi)^{1/2}}\left[\exp\left(-\frac{|k|^2}{2} \right) - \exp\left(-2|k|^2 \right) \right]. \tag{1.16}$$

The most commonly used complex basis is based on the well-known Morlet wavelet in *k*- and *r*-space

$$\psi(r) = \exp(ik_0 r)\exp\left(-\frac{r^2}{2} \right), \tag{1.17}$$

$$\hat{\psi}(k) = \Theta(k)\exp\left(-\frac{(k-k_0)^2}{2} \right), \tag{1.18}$$

in which the plane wave is modulated by a Gaussian of unit width. As k_0 increases, the angular selectivity of the basis increases, but the spatial selectivity deteriorates.

In quantum mechanics, the Paul wavelet is often used

$$\psi(t) = \Gamma(m+1)\frac{i^m}{(1-it)^{m+1}}, \tag{1.19}$$

$$\hat{\psi}_m(k) = \Theta(k)\cdot(k)^m \exp(-k). \tag{1.20}$$

A large numerical value of the parameter *m* corresponds to an increased number of zero moments of this wavelet.

Wavelet analysis allows you to obtain objective information about the signal being analyzed, since some properties of the wavelet transform do not depend on the choice of the analyzing wavelet, which makes these properties very important. Let's point out some of these basic properties.

The wavelet transform *W* [*f*] = *W* (*a, b*) of the vector function *f*(*t*) is a vector with components representing the wavelet transform of each component of the analyzed vector separately

$$W[\alpha\ f_1(t) + \beta\ f_2(t)] = \alpha W[f_1] + \beta W[f_2] = \\ = \alpha W_1[a,b] + \beta W_2[a,b]\ . \tag{1.21}$$

Invariance under shift and, as a consequence, commutativity of differentiation

$$W[f(t-b_0)] = W(a, b-b_0). \tag{1.22}$$

Conditions (1.21) and (1.22) lead to the commutability property for derivatives of vector analysis.

The wavelet differentiation operation can be represented as follows

$$W[\partial_t^m f] = (1)^m \int_{-\infty}^{\infty} f(t)\partial_t^m[\psi^*_{ab}(t)]dt\,. \tag{1.23}$$

Thus, to ignore, for example, large-scale polynomial terms and analyze high-order features or small-scale variations of the function *f*, it makes no difference whether to differentiate the analyzing wavelet or the function itself the required

number of times. This property is very useful considering that often the function *f* is a series of numbers, and the analyzing wavelet is given by a formula.

Invariance under stretching (compression) or the property of scale invariance is described by the relation

$$W\left[f\left(\frac{t}{a_0} \right) \right] = \frac{1}{a_0} W\left(\frac{a}{a_0}, \frac{b}{a_0} \right). \tag{1.24}$$

Consider the function $f \in C^m(t_0)$. Such a function is continuously differentiable at the point t_0 up to a derivative of order m. The wavelet transform coefficients of this function at $b = t_0$ must satisfy the inequality

$$W(a, t_0) \le a^{m+3/2}, \; a \to 0 \; . \tag{1.25}$$

If $f \in \Lambda^{\alpha}(t_0)$, i.e. the analyzed function belongs to the space of Holder functions with exponent α (f is continuous, $| f(t+t_0) - f(t) | = c|t_0|^{\alpha}$, $\alpha < 1$, c = const > 0), then the coefficients of its wavelet transform at $b = t_0$ can be written in the form of the formula

$$W(\alpha, t_0) \approx c\, a^{\alpha+1/2}, \;\; a \to 0. \tag{1.26}$$

All information about a possible feature of *f(t)* (localization t_0, intensity c, exponent α) is contained in the asymptotic behavior of the coefficients W(a, t_0) for small a. If the coefficients diverge on small scales, then f has a singularity at t_0 and the singularity index α is determined by the slope of the dependence log $|W(a, t_0)|$ to log a. If, on the contrary, they are close to zero in the vicinity of t_0 on small scales, then f at the point t_0 is regular.

The signal energy E_f can be calculated through the amplitudes (coefficients) of the wavelet transform (analogous to Parseval's theorem)

$$\int f_1(t) f_2^*(t) dt = C_{\psi}^{-1} \iint W_1(a,b) W_2^*(a,b) \frac{da db}{a^2}, \tag{1.27}$$

$$E_f = \int f^2(t) dt = C_{\psi}^{-1} \iint W^2(a,b) \frac{da db}{a^2}. \tag{1.28}$$

The energy density of the signal $E_W(a,b) = W^2(a,b)$ characterizes the energy levels (excitation levels) of the signal *f (t)* under study in space *(a, b)* = (scale, time).

Knowing the energy density $E_W(a,b)$, we can determine the local energy density at point b_0 (or t_0)

$$E_{\xi}(a,t_0)=\int E_W(a,b)\cdot\xi\left(\frac{b-t_0}{a}\right)db. \tag{1.29}$$

The window function ξ "maintains" a range around t_0 and satisfies the equality

$$\int\xi(b)db=1. \tag{1.30}$$

If we choose the Dirac function as ξ then the local energy spectrum takes the form

$$E_{\delta}(a,t_0)=W^2(a,t_0). \tag{1.31}$$

This characteristic makes it possible to analyze the time dynamics of the energy transfer of a process by scale - the exchange of energy between the components of the process of different scales at any given point in time.

Most often, studies concerning the practical use of the wavelet transform contain the results of calculations in which discrete wavelets are used. This preference is due to the fact that commonly used continuous wavelet bases are not, strictly speaking, orthonormal, since the elements of the basis are infinitely differentiable and decay exponentially at infinity, which contradicts strict orthonormality. There are no such problems with discrete wavelets. Because of this, discrete wavelets usually lead to more accurate transformation and representation of the signal and, in particular, its reverse recovery after the compression procedure.

The wavelet coefficients h_k and g_k an be uniquely determined within a multiscale analysis. They can be calculated directly, knowing the definition

$$\varphi(x)=\sqrt{2}\sum_k h_k\varphi(2x-k) \tag{1.32}$$

$$\psi(x)=\sqrt{2}\sum_k g_k\varphi(2x-k) \tag{1.33}$$

and properties of orthogonality of scale functions

$$\int\varphi(x)\varphi(x-m)dx=\delta_{0m}\ . \tag{1.34}$$

From (1.34) and the orthogonality of wavelets to scale functions, we obtain the following equation for the coefficients

$$\sum_k h_k h_{k+2m} = \delta_{0m} \tag{1.35}$$

$$\sum_k h_k g_{k+2m} = 0. \tag{1.36}$$

In a particular case, we can get a well-known filte

$$h_0 = \frac{1}{4\sqrt{2}}\left(1+\sqrt{3}\right), \quad h_1 = \frac{1}{4\sqrt{2}}\left(3+\sqrt{3}\right)$$

$$h_2 = \frac{1}{4\sqrt{2}}\left(3-\sqrt{3}\right), \quad h_3 = \frac{1}{4\sqrt{2}}\left(1-\sqrt{3}\right). \tag{1.37}$$

These coefficients define the simplest wavelet D^4 from the well-known property of orthonormal Daubechies wavelets with finite support. D^4 wavelets appear to be smoother at some points than others. Choosing the sign in the expression for h_3 will not change the general form of the scaling function, but will only renumber the coefficients.

Daubechies wavelets with zero moments, the number of which is equal to M, have μM continuous derivatives. Numerical calculations show that for large M we have $\mu \approx 0.2$. This shows that about 70 – 80% of zero moments cannot be used for further analysis. As the smoothness of a wavelet increases, the size of its domain of definition usually increases. For sufficiently smooth functions, Daubechies wavelets are much smaller (by a factor of 2^{Mj}) than the Haar wavelet coefficients. Therefore, using Daubechies wavelets the signal can be compressed much more. Since these wavelets are noticeably smoother, the inverse transformation (synthesis) is also more efficient.

The presence of relationships at two scales for multiscale analysis is a characteristic feature of the construction of wavelet packages. The main idea of their creation is to sequentially iterate the frequency band splitting while maintaining the same pair of filters. Let us denote the scaling function by the symbol ω_0, then the wavelet packet can be constructed using the following relations

$$\omega_{2n}(x) = \sum_k h_k \omega_n(2x-k), \tag{1.38}$$

$$\omega_{2n+1}(x)=\sum_k g_k\omega_n(2x-k)\,. \tag{1.39}$$

For the “mother wavelet” the symbol ω_1 *is used.* This family of wavelets forms an orthonormal basis in $L^2(R)$ called the fixed-scale wavelet packet basis.

Wavelets with a scale factor of 2 are most convenient for numerical calculations. However, within the framework of multiscale analysis, this factor can be any rational number. Therefore, it is possible to construct circuits with other integer or fractional scale factors. Sometimes their use can lead to better frequency localization.

Multiscale analysis can also be carried out with multidimensional functions, for example, by constructing tensor products. The tensor product method represents a direct path to the development of *r*- regular multiscale decomposition, which, in turn, leads to the appearance of multidimensional wavelets with compact support. This makes it possible to analyze any space of ordinary or generalized functions in *n* dimensions with a regularity of up to *r*.

The usual way to construct a two-dimensional orthogonal wavelet basis $\psi_{j,k}(x) = 2^{j/2}\psi(2^j x-k)$ is to form the corresponding functions from two one-dimensional bases using the tensor product

$$\psi_{j_1k_1;j_2k_2}(x_1,x_2)=\psi_{j_1,k_1}(x_1)\psi_{j_2,k_2}(x_2). \tag{1.40}$$

In this basis, two variables x_1 and x_2 are compressed differently.

For many applications, a technique is used in which the resulting orthonormal wavelet basis is scaled across both variables in the same way and the two-dimensional wavelets are given by the following expression

$$2^j\psi\left(2^j x-k,2^j y-l\right),\quad j,k,l\in Z\,, \tag{1.41}$$

but ψ is no longer the only function; on the contrary, it will be formed from three elementary wavelets. To create an orthonormal basis W_0, we now have to use three families

$$\varphi(x-k)\psi(y-l),\ \psi(x-k)\varphi(y-l),\ \ \psi(x-k)\psi(y-l). \tag{1.42}$$

Then two-dimensional wavelets will be written in the form

$$2^j\varphi\left(2^j x-k\right)\psi\left(2^j y-l\right),\ 2^j\psi\left(2^j x-k\right)\varphi\left(2^j y-l\right),$$

$$2^j \psi\left(2^j x - k\right)\psi\left(2^j y - l\right). \quad (1.43)$$

As an intermediate step, analysis can be performed on a two-dimensional plane along horizontals, verticals and diagonals with the same resolution in accordance with three wavelets (1.42).

There are $2n-1$ functions that form an orthonormal basis and perform multiscale analysis of any function from $L^2(R)$ in the general n-dimensional case. The normalization factor is equal to $2^{nj/2}$.

Wavelets are used both in purely theoretical work in functional analysis (regularization of gauge theories, conformal field theory, nonlinear chaos theory) and in the analysis of observational data (experimental work on quasi-crystals, meteorology, acoustics, seismology, nonlinear dynamics in accelerators, fluid dynamics and turbulence, surface structure, cosmic ray fluxes, solar wind, galaxy structure, density fluctuations in cosmology, properties of dark matter, gravitational waves, etc.).

In this paper we will consider the problems associated with the use of wavelets to study the structure of such complex systems as composites. The widespread use of polymer composites in the mechanical engineering, aviation, aerospace, shipbuilding and automotive industries has created the need to develop suitable structural diagnostic methods and tools that will be applicable to heterogeneous materials. Due to the increasing requirements for the technical condition of composite structural elements in the above-mentioned industries, diagnostic methods must be non-destructive and non-contact if possible. These methods should be sensitive to different types of damage in fiber composites and should provide damage detection, possibly at an early stage. Modal methods, together with advanced signal processing methods, satisfy all these requirements in most cases. Among other methods including random decrement signature analysis, Hilbert-Huang transform, temperature analysis and Poincaré maps of damaged structures, wavelet analysis is the most promising method. The most commonly used wavelet methods include collocation procedures [6 - 9], calculation formalism based on finite elements [10 - 19], analysis of heat flows in composite structures [20 - 29], multiscale analysis [30 - 36], application of algorithms for spaces with Riesz potential [37, 38], wavelet filtering of wave numbers [39].

CHAPTER 2
ACOUSTIC EMISSION

A large number of experimental techniques (Oskouei, Qi, Qiao and others [40 - 72]) are used to study the process of strain accumulation in composites. These techniques are usually divided into two main groups: active techniques and passive techniques. In the case of active methods, the composite structure is excited by an external source. The superiority of passive methods over active methods lies in their ability to perform structural health monitoring during the operation of a composite structure. The most common passive technique is acoustic emission.

Acoustic emission is defined as the transmission of an elastic stress wave through a material that is subjected to stress.

Mechanical stress usually arises from an internal source such as crack initiation and growth.

The necessary equipment for monitoring acoustic emissions consists of:

- structures under load;
- a network of acoustic emission sensors to record the slightest vibrations of the surface during testing of a composite structure and convert these vibrations into analog signals.
- preamplifiers, which increase the intensity of analog signals;
- acquisition and recording sections, where amplified signals are recorded and converted from analogue to digital;
- data processing sections where recorded digital acoustic emission signals are analyzed.

Acoustic emission analysis is typically performed using signals or features extracted from waveforms. Figure 1 shows a typical acoustic emission waveform. The following are the most important features of acoustic emission:

- presence of a threshold: only acoustic emission signals with an intensity above the threshold are recorded by the system;
- amplitude, namely the maximum voltage of the signal. It is usually indicated in units of dB;
- duration, i.e. time interval between the first and last crossing of the threshold (indicated in μs);
- rise time, namely the time interval between the first crossing of the threshold and the maximum amplitude (indicated in μs);
- counters that index the number of times a signal crosses a threshold in an increasing direction within the duration of the signal;
- energy, which is proportional to the area of the area under the rectangular signal within the duration of the signal. usually stated in attojoules (aJ) (1 aJ = 10^{-18} Joules);

- peak frequency, corresponding to the highest value in the frequency distribution obtained as a result of the fast Fourier transform of the signal (indicated in units of kHz).

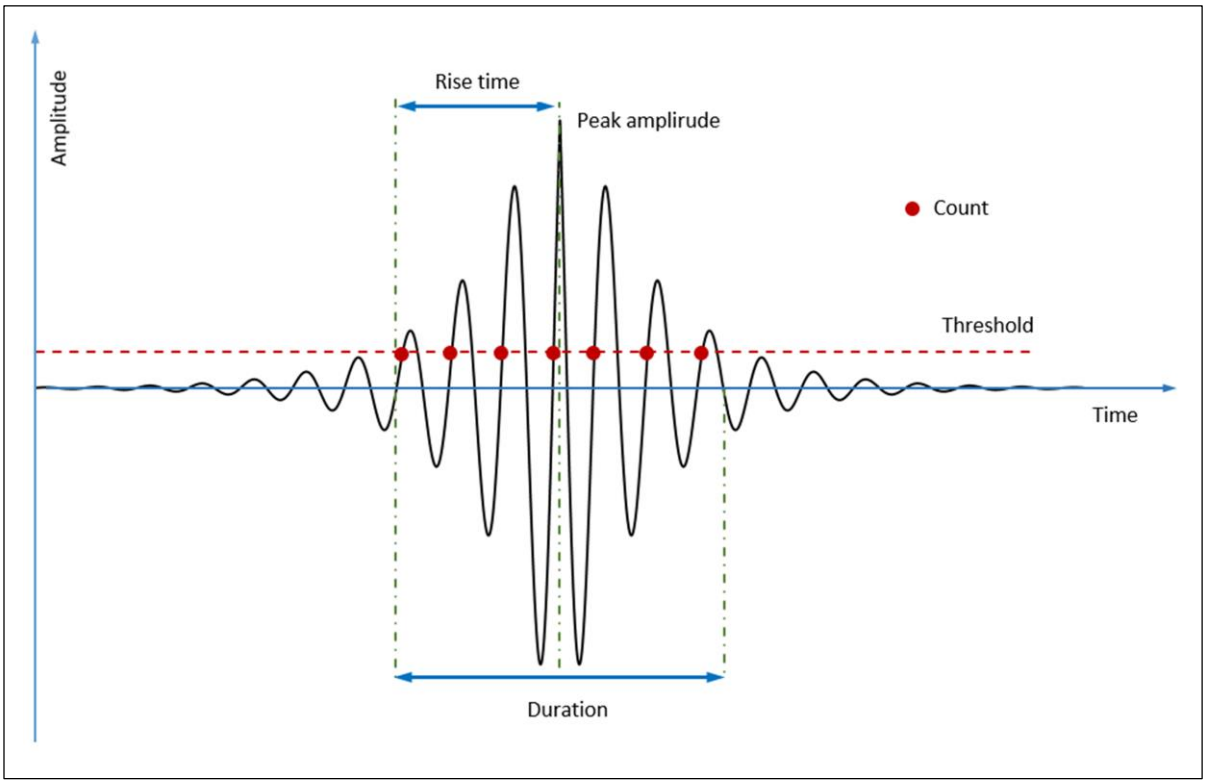

Figure 1. Typical acoustic emission.

Acoustic emissions can be divided into two main groups: damage diagnosis and damage prediction. The first group consists of three subgroups: detection of damage occurrence, localization of damage and identification of damage. The second group contains studies related to predicting the residual service life and residual strength of composite structures using acoustic emission.

Quite often, the acoustic emission technique is used to detect the onset of damage to layered composites. The studies cover a variety of loading conditions and configurations of composite structures: tension, compression, double cantilever beam stress, end-notch bending, mixed bending, 3-point and 4-point bending, buckling, quasi-static transverse indentation, low-velocity loading and compression after impact on a real composite structure subjected to arbitrary loading. Research covers a wide range of composite materials, including thermosets; glass/epoxy and carbon/epoxy, thermoplastic material; glass/polyester and glass/polyamide, sandwich and hybrid composites.

The sensitivity of damage detection is usually improved by combining acoustic emission data and mechanical data by introducing a so-called watchdog function. The sentinel function is defined as the logarithm of the mechanical energy to the acoustic emission energy:

$$f(x)=\ln\left[\frac{E_m(x)}{E_{AE}(x)}\right], \tag{2.1}$$

where
$E_m(x)$ is the mechanical energy (area under the load-displacement curve);
$E_{AE}(x)$ is the cumulative acoustic emission energy;
x is the displacement.

Depending on the damage state of the composite structure, the function f(x) can change as follows: 1) increase: i.e. the function shows that the structure is still intact and no damage or any microdamage has occurred in the material; 2) a sharp decrease in function: this trend shows that the material has suffered enormous damage; 3) constant trend: this shows that there is a balance between the mechanisms of destruction and the mechanisms of bridging in the fibers; 4) gradual decrease in $f(x)$: it is emphasized that the load-bearing capacity of the composite structure is gradually lost. Accordingly, the moment of onset of damage is considered to be the first large drop in the guard function curve.

The term “significant acoustic emission activity” is defined using the so-called historical indicator. The calculation of the historical index is preceded by determining the tensile strength of the sample using monotonic loading until its final destruction. A similar sample is then subjected to several load/overload cycles. During these cycles, acoustic emission signals are recorded until the maximum load of the previous cycle is reached. The historic index is defined as follows:

$$H(t)=\frac{N}{N-K}\cdot\frac{\sum_{i=K=1}^{i=N}S_{Oi}}{\sum_{i=1}^{i=N}S_{Oi}}, \tag{2.2}$$

where
$H(t)$ is the historic index at time t;
N is the number of acoustic emission hits up to time t;
S_{Oi} is the amplitude value of *i-th* hit;
K is a parameter that is depended to the number of hits.

Factors such as amplitude, pulse duration, rise time, center frequency, peak frequency and energy, and specimen geometry affect the reliability and repeatability of acoustic emission results in assessing damage in laminated composites.

The uncertainty of the probability amplitude distribution of the acoustic emission signal shape can be described by Shannon's entropy. An increase in Shannon's entropy indicates the occurrence of an internal change in the composite material, which may be associated with the occurrence of damage. The Shannon's entropy of each waveform is calculated using the following formula

$$H = \sum_{i=1}^{n} p(x_i) \cdot \log_2 [p(x_i)], \tag{2.3}$$

where

H is the Shannon's entropy;

$p(x_i)$ is the probability mass associated with waveform's numerical values x_i.

The second level of damage assessment of composite structures is the separation of acoustic emission signals from different damage mechanisms. This process is typically performed in one of four ways: 1) manual recognition of acoustic emission data, 2) unsupervised clustering, 3) supervised classification, and 4) signal processing.

However, sometimes different mechanisms of damage are not fully differentiated using only one acoustic emission signature. In this situation, it is better to use several acoustic emission functions simultaneously to determine the type of damage with greater confidence. In this case, due to the complex relationships between different acoustic emission functions, the data separation process is usually performed using machine learning methods: unsupervised and supervised methods.

Unsupervised clustering methods such as *k*-means, genetic *k*-means, fuzzy *c*-means, Gaussian mixture distribution, self-organizing map, and hierarchical models are often used to cluster damage in composites. Typically, all unsupervised clustering methods attempt to separate a set of acoustic emission signals $\{X_1, X_2, \ldots, X_n\}$. Each signal can contain *p* features $X_i = [x_1, x_2, \ldots, x_p]$, $i = 1, 2, \ldots, n$ in *k* ($k \leq n$) clusters $\{C_1, C_2, \ldots, C_k\}$.

Among the unsupervised clustering methods, *k*-means is widely used in numerical experiments to distinguish between different damage mechanisms in laminated composites. The K-means calculation technique involves clustering acoustic emission data in two stages. At the first stage, the centroid of the initial clusters should be randomly selected. Each data point is then assigned to a cluster with the centroid of the nearest cluster. In the second step, the new centroid of each cluster is updated to the average of all data points within the cluster

$$C_i^t = \left\{ X_n : \left\| X_n - m_i^{(t)} \right\|^2 \leq \left\| X_n - m_j^{(t)} \right\|^2 \quad \forall\, j, 1 \leq j \leq k \right\}$$

$$m_i^{(t+1)} = \frac{1}{\left|C_i^t\right|} \sum_{X_j \in C_i^{(t)}} X_j \,, \tag{2.4}$$

where
$C_i^{(t)}$ is the *i*-cluster;
$m_i^{(t)}$ is the center of *i*-cluster at *t*-iteration.

Although this method is simple and requires little computational effort, there is no guarantee that it will always produce optimal results. In other words, there is a possibility that the algorithm is not partitioning the data correctly. This is due to the random selection of the centroids of the initial clusters.

Overcoming this limitation can be achieved by adding a fuzzy parameter to *k*-means, which is called fuzzy *c*-means, or by combining *k*-means with a genetic algorithm, which is called genetic *k*-means algorithm. The process of clustering using *k*-means algorithm is similar to *k*-means with the difference that in the said procedure a membership parameter is defined which allows a data point to belong to more than one cluster at the same time with different membership values ranging from 0 to 1. To find the best clustering, for *k*- means algorithm needs to minimize the objective function $J(X; C)$

$$J(X, C) = \sum_{i=1}^{k} \sum_{j=1}^{n} \left(\gamma_{ij}\right)^{\alpha} \left\| X_j - C_i \right\|^2$$

$$D_{ij}^2 = \left\| X_j - C_i \right\|^2 = \left(X_j - C_i\right)^T \left(X_j - C_i\right), \tag{2.5}$$

where
γ_{ij} is the membership parameter;
α is the fuzzier.

The conditions for the minimum of the objective function can be represented as

$$\gamma_{ij} = \left[\sum_{m=1}^{k} \left(\frac{D_{ij}}{D_{mj}} \right)^{2/(\alpha-1)} \right]^{-1} ; 1 \le i \le k, 1 \le j \le n \tag{2.6}$$

and

$$C_i = \frac{\sum_{j=1}^{n} (\gamma_{ij})^{\alpha} X_j}{\sum_{j=1}^{n} (\gamma_{ij})^{\alpha}}; \; 1 \le i \le k. \tag{2.7}$$

Genetic *k*-means algorithm is used to create the best clusters associated with the centroids in new iterations by intersecting the centroids of previous clusters.

It should be noted that the Gaussian mixture distribution algorithm assumes that the entire data set can be expressed as a weighted sum of several Gaussian densities with unknown parameters $p(x)$

$$p(x) = \sum_{k=1}^{K} \omega_k \, g(X \,|\, \mu_k, \Sigma_k) \tag{2.8}$$

$$g(X \,|\, \mu_k, \Sigma_k) = \frac{1}{\sqrt{(2\pi)^k |\Sigma_k|}} \exp\left[\frac{-0.5 \cdot (X - \mu_k)^T}{\Sigma_k (X - \mu_k)} \right] \tag{2.9}$$

$$\sum_{k=1}^{K} \omega_k = 1. \tag{2.10}$$

where

g is the Gaussian density function with mean vector μ_k and covariance matrix Σ_k;

X is data;

ω_k is the mixture weight function.

The algorithm first estimates random initial numerical values for the mean vectors and covariance matrices of the density distributions. It then calculates the weighting function values for all data points and mixture distributions. After this, new mean vectors and covariance matrices are updated. This process is repeated until the stopping criterion is met, which can be the maximum number of iterations

$$\mu'_k = N_k^{-1} \sum_{i=1}^{n} \omega_{ik} X_i, \qquad 1 \le k \le K \tag{2.11}$$

$$\Sigma'_k = N_k^{-1} \sum_{i=1}^{n} \omega_{ik} (X_i - \mu'_k) \cdot (X_i - \mu'_k)^T, \qquad 1 \le k \le K \tag{2.12}$$

$$\omega_k' = N_k N^{-1}, \qquad 1 \le k \le K, \tag{2.13}$$

where
N_k is sum of membership weight for k^{th} component defined as $N_k = \Sigma\omega_{ik}$.

A frequently used signal processing method for recognizing types of damage in composite materials is the wavelet transform, in which the signal is decomposed into low-frequency and high-frequency components.

Depending on the type of wavelet transform, both the low-frequency and high-frequency parts (batch wavelet transform) or only the low-frequency part (discrete wavelet transform) will be decomposed into other levels until the original signal is finally decomposed into several subcomponents with different frequencies. Then, depending on the frequency of the subcomponents, one or more subcomponents are correlated with specific types of damage. For acoustic emission type signals, the packet wavelet transform is usually preferred over the discrete wavelet transform because the valuable information is generally contained in the high frequency components (e.g. fiber damage signals).

The frequency range of each subcomponent in the wavelet wavelet transform tree is calculated using the following formula

$$\left[n f_S \, 2^{-(i+1)}, (n+1) \, f_S \, 2^{-(i+1)} \right], \tag{2.14}$$

where
f_S is the acoustic emission sampling rate, index i shows the level of decomposition, and index n shows the label of subcomponent, which is equal to n = 0, 1, …, 2^{i-1} for decomposition level i.

The relative energy of each subcomponent, compared to the original signal, can be related to the damage mode in the composite structure using a system of equations

$$E_i^n = \sum_{T=t_0^n}^{t_1^n} \left[f_i^n(T) \right]^2 \tag{2.15}$$

$$P_i^n = \frac{E_i^n}{\sum_i \sum_n^{2^{i-1}} E_i^n}, \tag{2.16}$$

where
E_i^n is the energy of subcomponent n located in level i;

f_i^n is the wavelet subcomponent;
t_o^n and t_1^n show its time period;
P_i^n represents the energy percentage of the subcomponent respect to the original signal.

An analysis of the effectiveness of the wavelet technique was carried out using experimental results on acoustic emission [58]. The theoretical part included a study of the shift in the spectral density of the signal during damage to a composite sample, the use of entropy as a basis for selecting the wavelet transform of the most effective form and, as a final stage, the implementation of this transformation to identify damage to the composite structure.

The spectral density of the signal can be determined in the following form

$$S(f) = \gamma A^{2+\beta}\left(N_e f^{\alpha}\right)^{-1} \quad , \tag{2.17}$$

where
A is the signal amplitude;
N is the number of structural elements;
f is the frequency;
α, β, γ are the constants.

Without loss of generality, S can be represented as a value inversely proportional to the value f

$$S(f) = \frac{\gamma}{f^{\alpha}}. \tag{2.18}$$

Let's transform the value S

$$\log[S(f)] = \log\gamma - \alpha\log(f). \tag{2.19}$$

The characteristics of the signal and its shift can be classified by the slope coefficient, which is determined by the coefficient α.

The shift in spectral density and signal characteristics based on different types of noise is also used to analyze composite materials. Fluctuations recorded in these systems have a low-frequency component. The term *1/f* noise or flicker noise is usually used for fluctuations of a specified type or shift.

The entropy of the waveform is used as the main identifier to select the appropriate wavelet for analysis. For a signal having a random amplitude distribution as $\{s_1, s_2, s_3, \ldots, s_n\}$, the generalized form of entropy $H_a(S)$ can be written as

$$H_a(S) = \log\left\{\sum_{k=1}^{n}\left[P(S_k)\right]^a\right\}^{1/(1-a)}, \quad (2.20)$$

where
$P(S_k)$ is the discrete probability distribution of the amplitude.

The generalized form of entropy defined in equation (2.20) can be described as Rényi entropy. The value of the parameter a ($a > 1$ or $a < 1$) is related to the distribution of the analyzed data. For the case $a \to 0$ equation (2.20) is transformed to obtain the maximum entropy or Hartley entropy

$$H_0(S) = \log n. \quad (2.21)$$

Shannon entropy corresponds to the case $a = 1$

$$H_1(S) = \sum_{k=1}^{n} P(S_k)\log\left[P(S_k)\right]. \quad (2.22)$$

And, accordingly, the Rényi entropy corresponds to the value $a = 2$

$$H(S) = -\log\left\{\sum_{k=1}^{n}\left[P(S_k)\right]^2\right\}. \quad (2.23)$$

The selection of the optimal wavelet for processing acoustic signals in this work is performed using Rényi entropy. Maximum information about the waveforms in their time-frequency domain and the distribution of spectral energy in different frequency ranges is based on the selection of the best wavelet.

Waveform entropy is a measure of the randomness or instability of the waveform and therefore it is safe to assume that a lower entropy value determines the stability of the acoustic waveform. In addition, the case of maximum energy can be analyzed using certain wavelet transforms of the energy coefficients of the acoustic signal. The mathematical form of these trends is the relation

$$\eta = \frac{E_{WT}}{H(S)}, \quad (2.24)$$

where
E_{WT} is the energy coefficient of the waveform measured using wavelet transform.

A brief description of the procedure for calculating the quadratic Rényi entropy can be expressed as follows. The E_{WT} and *H(S)* values are calculated using the discrete wavelet transform.

The acoustic waveform *f(t)* can be expressed as follows

$$f(t) = \{S_q, S_2, ..., S_n\}^T, \tag{2.25}$$

where
n is the length of the waveform.

If the waveform *f(t)* is decomposed using the wavelet $\psi(t)$, then the deformation wavelet transform can be expressed as

$$WT_j = f(t), \psi_j(t), \tag{2.26}$$

where
j is the number of the selected wavelet.

The result of the wavelet transform is the operator relation

$$WT_j = \{\omega t_1, \omega t_2, ..., \omega t_n\}^T. \tag{2.27}$$

The energy factor E_{WT} is calculated as follows

$$E_{WT} = \sum_{k=1}^{n} \left|\omega t_{j,k}\right|^2. \tag{2.28}$$

The discrete probability for calculating the quadratic Rényi entropy is

$$p(x_k) = \frac{\left|\omega t_k\right|^2}{\sum_{i=1}^{n} \left|W T_{i,j}\right|^2}. \tag{2.29}$$

However, the choice of the value of η must be carried out quite accurately, because this quantity represents the coefficient of entropy and energy, which can generally be measured from the transient and unstable waveform of the acoustic signal.

The wavelet transform uses 3 wavelets to decompose the acoustic signal for three different levels *N*. In this case, the spectral energy with the number of

components equal to $C = 2^N = 8$ is necessarily obtained. Namely, the functional meaning

$$WPT_j = f(t), \psi_j(t) \tag{2.30}$$

corresponds to form

$$WPT_j = \left| W_{j,1}, W_{j,2}, \ldots, W_{j,8} \right|, \tag{2.31}$$

where

$W_{j,c}$ is the spectral energy of the waveform distributed in the component C.

The wavelet that recovered the maximum spectral energy in the dominant frequency band, max $W_{j,c}$ {for C = 1, 2, … , 8} can be selected as the best wavelet for further analysis.

In this work, the best wavelet was determined from a list of 24 wavelets using the procedures described earlier. The result of the decomposition of the acoustic waveform was the appearance of eight components. Each of these components contains the spectral energy of the signal distributed in the time domain of a specific frequency band. Generally, in the CFRP material used in this research work, the macroscopic damage modes can be generalized into matrix cracking, delamination, matrix-fiber bond failure, fiber rupture, fiber pullout, and through-laminar (interlaminar) crack growth.

The characteristic frequency ranges depended on the nature of the deformation. In particular, cracking or delamination of the matrix results in a characteristic frequency range of 150–200 kHz. At the same time, a fiber break corresponds to a frequency above 300 kHz or 350 kHz. Three samples of composite material *A1*, *A2* and *A3* were analyzed with test durations in the range (390 ÷ 440) s and the number of acoustic shocks, respectively, in the range $(1.9 \div 2.1) \cdot 10^3$.

The wavelet family included Haar- (*Haar k* = 1); Daubechies- (*db k*, *k* = 2, …, 11); Symlet- (*sym k*, *k* = 12, …, 18) and Coiflet- (*coif k*, *k* = 19, …, 23) Dmeyers- (*Dmey k* = 24); wevelets. The results of determining the average entropy, average energy, as well as η values are presented, respectively, in Figures 2,3 and 4.

The diagrams display the results of assessing the critical values of the threshold values for selecting the maximum and minimum parameters “threshold max” and “threshold min”. In addition, for a series of wavelets, the distribution density of wavelets in the min-max band was estimated using the formula

$$\varphi_{Wk} = \frac{N_{Wk} - \sum_{\min,\ \max}}{N_{Wk}}, \qquad k = H, E_W, \eta, \tag{2.32}$$

where
N_W is the total number of wavelets in the series;
$\Sigma_{min,max}$ is the number of wavelets, the corresponding parameters are outside the threshold values.

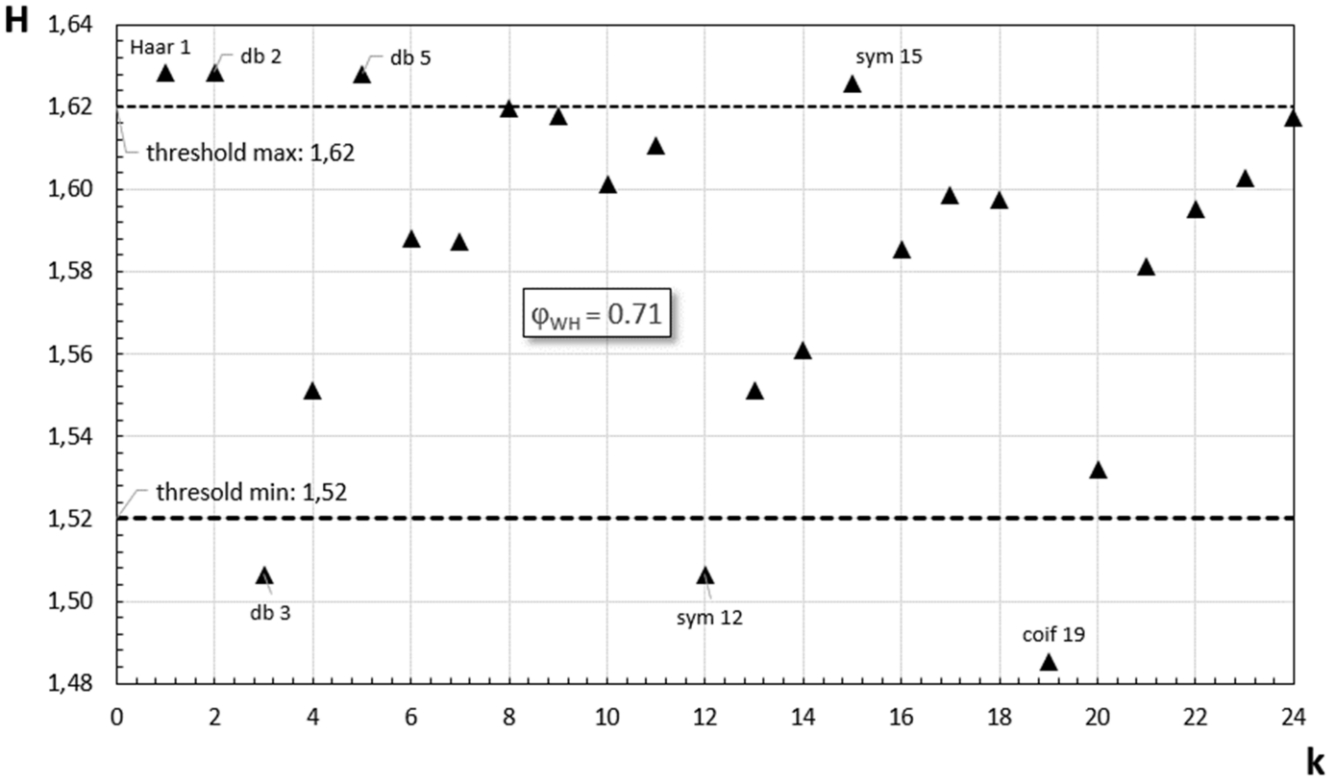

Figure 2. H-distribution for wavelets according to the average entropy parameter.

The H-distribution is characterized by a sufficiently large number of wavelets, the average entropy of which is outside the threshold values.

In particular, the following wavelets are located above the maximum threshold: Haar- and Daubechies- (subseries *db k*, *k* = 2, 5, 15). Three wavelets, namely: Daubechies- (*db 3*), Symlet- (*sym 12*) and Coiflet- (*coif 19*) have an average entropy value less than the minimum threshold value (= 1.52). It is quite natural that preference in terms of the min-max parameter for entropy should be given to Daubechies wavelets with indices k = 2, 3 and 5. Accordingly, Haar- and Coiflet wavelets should be excluded from further analysis in terms of the entropy parameter.

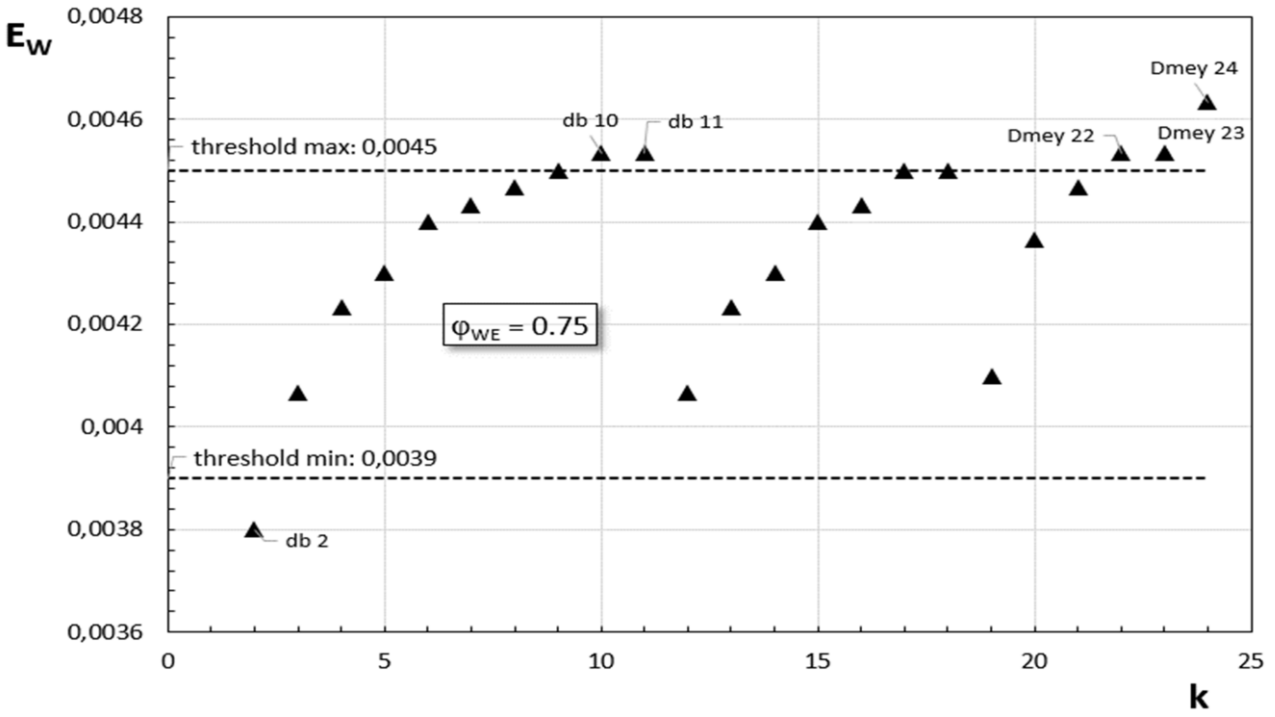

Figure 3. E-distribution for wavelets according to the average energy parameter.

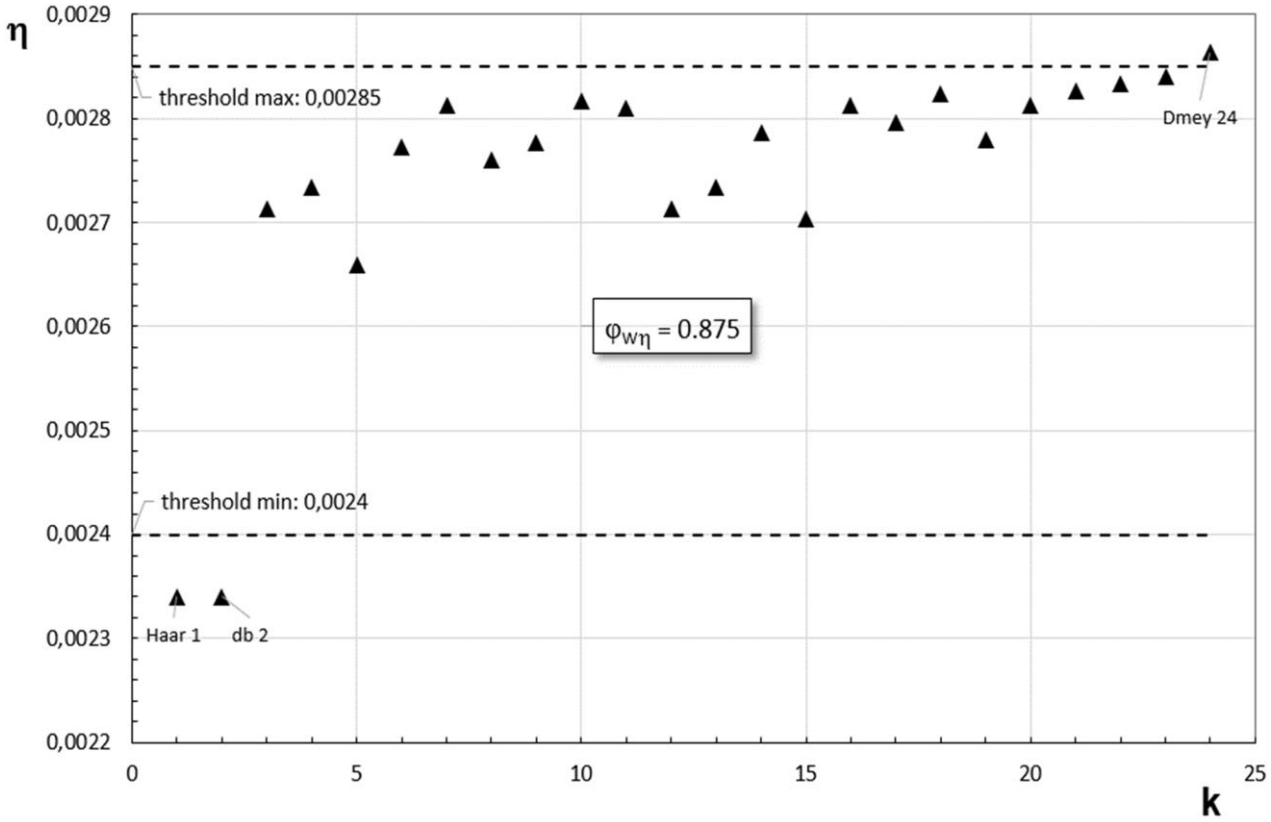

Figure 4. η-distribution for wavelets.

The average energy distribution is characterized by a maximum difference Σ_{max} - Σ_{min} = 4. Exceeding the maximum threshold for average energy is typical for

wavelets: Daubechies- (db *k* subseries, k = 10, 11) and Dmeyers- (Dmey *k* subseries, *k* = 22 - 24). Below the minimum threshold for average energy there is only one wavelet: Daubechies- (db 2). Preference for the min-max parameter for the average energy should be given to the Daubechies wavelet with index *k* = 2. Accordingly, Dmeyers wavelets with indices *k* = 22, 23 and 24 should be excluded from further analysis for the average energy parameter.

In turn, only one wavelet, namely, Dmeyers- (db 24), exceeds the maximum threshold in the η-parameter. Wavelets: Haar 1 and Daubechies- (db 2) are located below the minimum threshold in the η-parameter. The absence of repeating wavelets from one, fixed series makes it difficult to select wavelets based on the min-max parameter for the value η.

As a result of the analysis, recommendations for choosing the optimal wavelet having average energy, average entropy and η-parameter, that satisfy the min-max parameter should be pointed to Daubechies-wavelet (db 2). Ranking the distribution density of wavelets within threshold values for average energy and entropy, as well as the η-parameter, leads to the following chain:
$\varphi_{W\eta}$ (=0.875) > φ_{WE} (=0.75) > φ_{WH} (=0.71).

The generation and propagation of acoustic waves strictly depends on the properties of the material and the specific configuration.

Using a transform with wavelets dmey, coif5 and coif4, acoustic signals can be decomposed into 8 components WF_i, *i* = 1, 2, ..., 8. Processing of the responses of composite structures to acoustic emission signals was carried out for each WF_i component separately for eight frequency ranges in interval 0 ÷ 500 kHz. The width of each subband was 62.5 kHz.

The dominant frequency of each waveform is different from each other. Because each of these dominant frequency bands represents different types of damage from which acoustic signals are emitted.

The spectral distribution of dimensionless relative energy was studied for wavelets of three characteristic shapes, namely: Dmey-, coif 4- and coif 5 wevelets. The results are presented in Fig. 5, 6 and 7.

The Dmey-wavelet recovered most of the spectral energy in all selected waveforms. However, the coif5-wavelet recovered most of the spectral energy, although it is not observed among all the selected 8 signals. When comparing the spectral energy of a large number of signals, it can be noted that a significantly larger number of signals that recovered most of the spectral energy occur when they are decomposed using a dmey-wavelet. Therefore, dmey-wavelet is selected as the best wavelet for acoustic signal processing in this study.

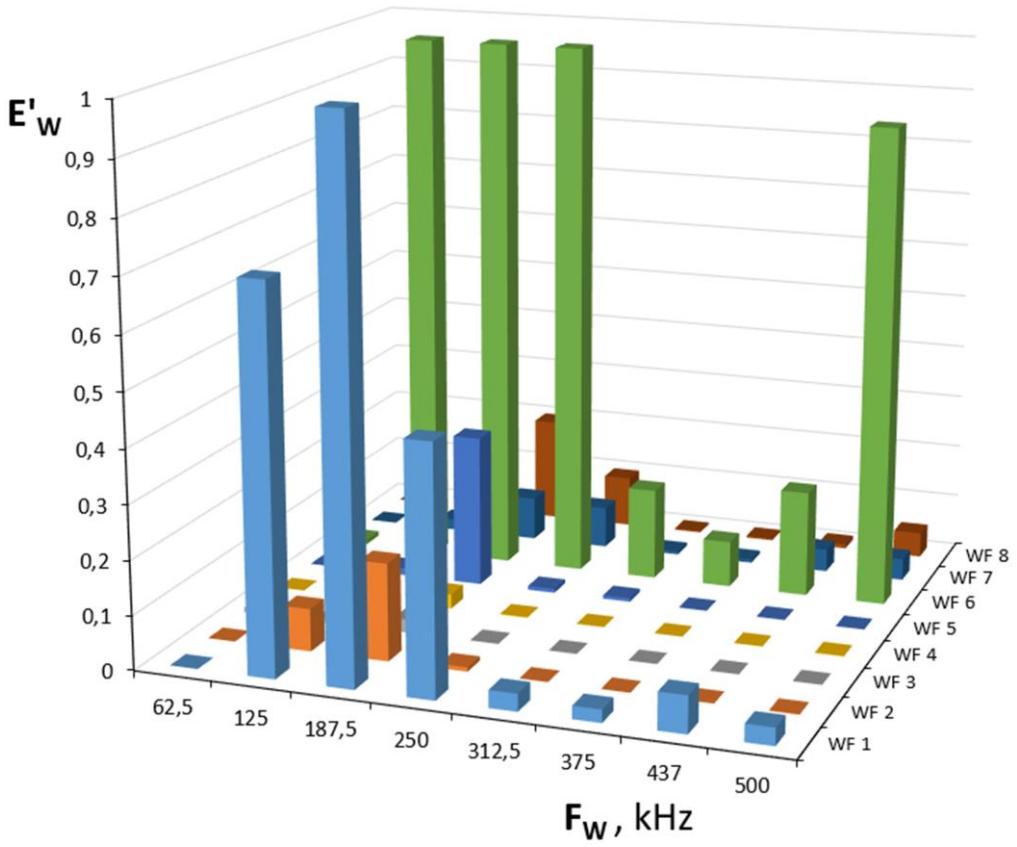

Figure 5. Spectral distribution $E'_W = f(F_W)$ for dmey-wavelet.

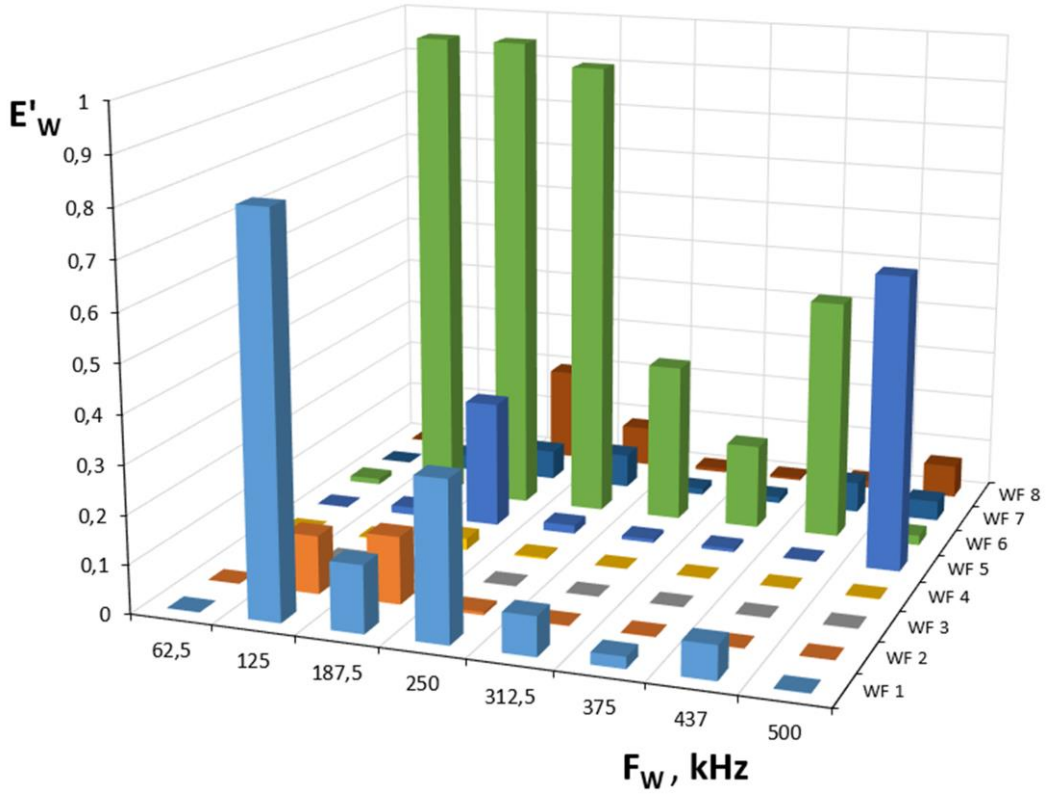

Figure 6. Spectral distribution $E'_W = f(F_W)$ for coif 4-wavelet.

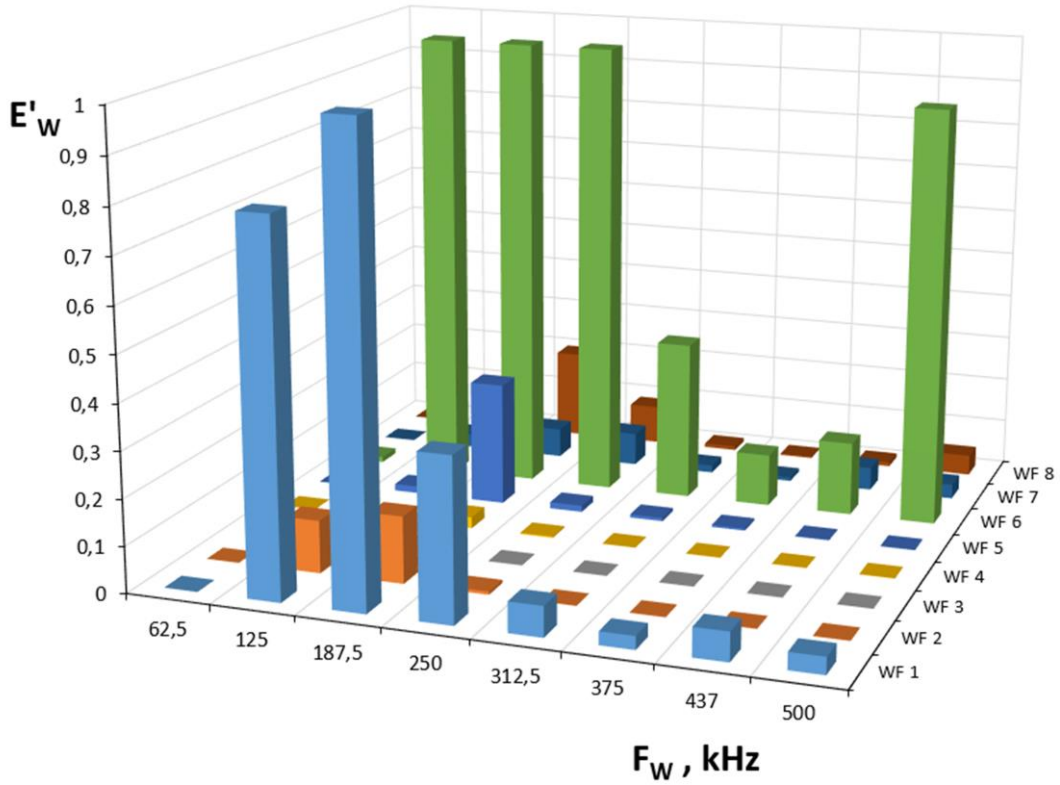

Figure 7. Spectral distribution $E'_W = f(F_W)$ for coif 5-wavelet.

The resulting spectral distribution for dmey- and coif-wavelets indicates the predominant contribution of the *WF k* components ($k = 1, 6$). Based on these facts, a separate analysis of the frequency dependence in matrix form was carried out for *WF k*

$$E'^{(k)}_W = \alpha^{(i,k)}\, F^{(i)}{}_W, \;\; i = 0,1,...,5; \quad k = 1,6. \tag{2.33}$$

The explicit form of the matrix coefficients $\alpha(i,k)$ is presented below for Dmey-wavelt

$$\alpha(i,k) = \begin{pmatrix} -3.2\cdot10^{-1} & -1.2\cdot10^{-2} & 4\cdot10^{-4} & -3\cdot10^{-6} & 6\cdot10^{-9} & -5\cdot10^{-12} \\ 3.32 & -2.7\cdot10^{-1} & 4.9\cdot10^{-3} & -3\cdot10^{-5} & 6\cdot10^{-8} & -5\cdot10^{-11} \end{pmatrix} \tag{2.34}$$

for coif 4-wavelet:

$$\alpha(i,k) = \begin{pmatrix} -4 & 1.1\cdot10^{-1} & -9\cdot10^{-4} & 3\cdot10^{-6} & -6\cdot10^{-9} & 4\cdot10^{-12} \\ -7.3 & 4.2\cdot10^{-2} & 1.9\cdot10^{-3} & -2\cdot10^{-5} & 4\cdot10^{-8} & -3\cdot10^{-11} \end{pmatrix} \tag{2.35}$$

and for coif 5-wavelet:

$$\alpha(i,k)=\begin{pmatrix} -1.5 & 2.2\cdot10^{-2} & 9\cdot10^{-5} & -1\cdot10^{-6} & 4\cdot10^{-9} & -3\cdot10^{-12} \\ -6.7 & 2.9\cdot10^{-2} & 2\cdot10^{-3} & -2\cdot10^{-5} & 4\cdot10^{-8} & -3\cdot10^{-11} \end{pmatrix}. \quad (2.36)$$

From the above observations, it can be concluded that wavelet analysis of acoustic emission response signals has the potential to identify the damage process of composite structures since it can distinguish acoustic signals based on frequency and time domain characteristics. However, it should be emphasized that these waveforms are representative of load stages. Extracting the dominant frequency band using the wavelet transform using the best wavelet still makes it possible to distinguish the process of damage to the internal structure of two-component composites, the inclusions for which differ in size by no more than an order of magnitude.

CHAPTER 3
DAMAGE IDENTIFICATION

The widespread use of polymer composites has created the need to develop suitable methods and tools for structural diagnostics applicable to heterogeneous composite materials. In connection with the increasing requirements for the technical condition of composite structural elements in a wide variety of industrial sectors, diagnostic methods [73 - 89] must meet a number of conditions: they must be sensitive to various types of damage occurring in fiber composites and must provide damage detection [90 - 102], possibly at an early stage of their distribution, and, finally, they must allow testing under environmental conditions [103 - 112] and be inexpensive. Among the works devoted to damage detection, studies Ashory, Katunin, Yan should be highlighted.

Classical modal analysis, that is, the analysis of natural frequencies and modal shapes, can only detect large damage, which is confirmed by numerous experimental studies. Given the fact that polymer-fiber composites are characterized by high variability in their mechanical properties, and the fact that these properties can be influenced by many factors (for example, changes in environmental and working conditions), natural frequency analysis is ineffective. when assessing damage in these materials.

Continuous wavelet transform with vibration signal analysis was first used to detect and localize cracks in beams. The first application of discrete wavelet transforms (Daubeches wavelets) was aimed at detecting damage in composite laminates.

Improving the sensitivity of wavelet methods for solving damage identification problems is directly related to the high accuracy of assessing the presence and position of damage. In particular, the technique of using the zero-order energy moment to identify damage based on continuous wavelet transforms using 8th order Daubechies wavelets is quite popular. *B*-spline wavelets are used in the development of discrete wavelet transform-based algorithms for identifying damage in composite beams and plates. Despite the limitations of the discrete wavelet transform, where only compactly supported orthogonal wavelets could be applied, the application of *B*-spline wavelets shows the highest sensitivity to damage compared to all other compactly supported orthogonal wavelets.

Improving damage identification algorithms also involves the use of auxiliary methods. In particular, researchers have widely used a damage detection algorithm based on continuous wavelet transform supported by artificial neural networks. This technique is used to detect delaminations in composite beams. The 2D discrete wavelet transform, together with particle system optimization in composite structures, constitutes a two-stage damage detection mechanism. In turn, structural diagnostics often rely on discrete wavelet transform using *B*-spline wavelets. This technique can be improved by using fractional *B*-spline wavelets.

Qualitative analysis of these wavelets makes it possible to select their most appropriate parameters in order to increase the sensitivity of the method. Fractional wavelet transforms allow for a combination procedure with a genetic algorithm, which was used to select the optimal parameters of fractional *B*-spline wavelets.

The continuous wavelet transform is based on the integration of square-integrable functions $f(x) \in L^2(\boldsymbol{R})$ into Hilbert space. This transformation can be viewed as the convolution of a wavelet function $\psi(a, b)$, where $a \in \boldsymbol{Z}$, $a > 0$ and $b \in \boldsymbol{R}$ denote the scaling and shift parameters, respectively. The transformation can be represented by the following equation

$$W\ f(a,b,s) = s^{-2} \int_{-\infty}^{\infty} f(s)\psi\left(\frac{x-b}{a}\right)dx, \tag{3.1}$$

where
$Wf(a, b, s)$ is a set of wavelet coefficients.

It should be noted that the continuous wavelet transform does not have such a strong restriction on the type of wavelet function, i.e. these functions can be almost arbitrary. The only condition that must be satisfied is the admissibility condition

$$\int_{-\infty}^{\infty} \psi(a,b)dx = 0. \tag{3.2}$$

In the vast majority of cases, wavelets can be characterized by the following points

$$\int x^{\alpha}\psi(x)dx = 0. \tag{3.3}$$

Representing a discrete transform as a signal with variable resolution forms a descending sequence of function spaces $V_j \subset L^2(\boldsymbol{R})$

$$\ldots V_3 \subset V_2 \subset V_1 \subset V_0 \subset V_{-1} \subset V_{-2} \subset V_{-3} \ldots \tag{3.4}$$

which have the following properties

$$\bigcup_{j\in Z} V_j = L^2(R), \quad \bigcap_{j\in Z} V_j = \{0\}. \tag{3.5}$$

The orthogonal complement in the space V_j for any j in the space V_{j-1} is a space with an orthonormal base ψ_{jk}, $j, k \in Z$. Thus, there is a constraint on the wavelet and the scaling function: they must be orthonormal or (semi-, bi-) orthogonal. During the discrete wavelet transform, the signal *f(x)* is decomposed into a set of approximation coefficients and a set of detail coefficients at each level of decomposition, the signal can be represented in the following form

$$f(x) = \sum_{n=-\infty}^{\infty} f_n^0 \varphi(x-n), \tag{3.6}$$

where

$\varphi(x\text{-}n)$ denotes the scalable function translation procedure.

The discrete wavelet transform decomposition can be represented by a set of filters. In this case, the resulting sets of approximation and detailing coefficients can be represented in the form

$$f_n^{(j)}(x) = \sum_l \tilde{h}_{2n-l}\, f_l^{(j-1)}, \tag{3.7}$$

$$d_n^{(j)}(x) = \sum_l \tilde{g}_{2n-l}\, d_l^{(j-1)}, \tag{3.8}$$

where

$\tilde{h}$, $\tilde{g}$ are the impulse responses of the low-pass and high-pass filters, respectively.

The downsampling procedure during the discrete wavelet transform causes the resulting sets of coefficients to be half the length of the original signal in the case of single-level decomposition. In turn, as a result, with each subsequent level of decomposition, a half decrease in the resulting length of the sets of obtained coefficients is observed.

The stationary wavelet transform can be considered as a redundant transform. Therefore, the downsampling procedure is omitted during decomposition. Therefore, expansion relations (3.7) and (3.8) take the form

$$f_n^{(j)}(x) = \sum_l \tilde{h}_l\, f_{n+2^{jl}}^{(j-1)}, \tag{3.9}$$

$$d_n^{(j)}(x) = \sum_l \tilde{g}_l\, d_{n+2^{jl}}^{(j-1)}, \tag{3.10}$$

and the length of the resulting sets of coefficients remains the same as for the original signal.

Lifting wavelet-transform is a two-stage wavelet transform that starts with a decomposition based on the classical discrete wavelet transform and then preliminarily performs a lifting procedure. Lifting is based on the prediction of one part of the signal based on a set of filters applied to that part, in accordance with the fact that these parts are correlated. The decomposition procedure represented by filters is as follows

$$f_{j_0,k_0}^{(j)}(x)=\sum_l h_{j_0,k_0,l}\, f_{j_0+1,l}^{(j)}\,, \tag{3.11}$$

$$d_{j_0,k_0}^{(j)}(x)=\sum_l g_{j_0,k_0,l}\, d_{j_0+1,l}^{(j)}\,, \tag{3.12}$$

This operation causes problems in the frequency domain. To resolve this issue, an update procedure is performed that updates the first signal based on the second.

Fractional scaling functions do not have compact support and are not symmetric unless their order is integer. This means that they could not be used in discrete wavelet transforms. However, to avoid this problem, the fractional wavelet transform algorithm can be constructed based on Fourier series. The general difference between discrete and fractional wavelet transforms is that the detailed wavelet transform is defined by fractional order filters. The orthogonal high-pass filter and low-pass filters in the *z*-domain for the fractional wavelet transform are as follows

$$H_{\perp}^{\alpha}\left(e^{j\omega}\right)=H^{\alpha}\left(e^{j\omega}\right)\sqrt{\frac{A^{2\alpha+1}\left(e^{j\omega}\right)}{A^{2\alpha+1}\left(e^{2j\omega}\right)}} \tag{3.13}$$

$$G_{\perp}^{\alpha}\left(e^{j\omega}\right)=e^{-j\omega}H_{\perp}^{\alpha}\left(-e^{-j\omega}\right), \tag{3.14}$$

where

$$H^{\alpha}\left(e^{j\omega}\right)=\sqrt{2}\left(\frac{1+e^{-j\omega}}{2}\right)^{\alpha+1} \tag{3.15}$$

it is a non-orthogonal scaling filter for fractional *B*-spline wavelet and

$$A^{\alpha}\left(e^{j\omega}\right)=\sum_{n\in Z}e^{-jn\omega}\int\beta^{\alpha}\left(x\right)\beta^{\alpha}\left(x+n\right)dx \qquad (3.16)$$

is an autocorrelation filter *B*-spline;
β is a scaling factor;
α means fractional order of the scaling function.

Let us consider the propagation of a pulse load wave of two types, which simulate the peak change in the stiffness of a composite material in the form of a rectangular beam. The first type of load is a narrow peak band sinusoidal base

$$f\left(t\right)=P\left[H\left(t\right)-H\left(t-\frac{N_P}{f_0}\right)\right]\cdot\left[1-\cos\left(\frac{2\pi\ f_0 t}{N_P}\right)\right]\sin\left(2\pi\ f_o t\right), \qquad (3.17)$$

where
H (t) is the unit step function,
f_0 is the constant frequency,
N_P = const$_1$, *B* = const$_2$,
$P = B \cdot N$.

The second type of load is a broadband pulse of a triangular shape, which can be represented in the following form

$$f\left(t\right)=P\left[H\left(t\right)-H\left(t-A_1\right)\right]\cdot\left[1-\left(t-0.5A_1\right)\frac{sign\left(t-0.5A_1\right)}{0.5A_1}\right], \qquad (3.18)$$

where
A_1 = const.

A narrowband pulsed load was used to demonstrate the non-dispersive characteristics of this type of load. The definition of narrow and wide bandwidth refers to the frequency spectrum of the signals and depends on the ratio of the bandwidth to the center frequency.

It makes sense to use the wavelet approach to find the shortest arrival time for various frequency components of the signal. The continuous wavelet transform of a function is defined by the formula

$$WT_f\left(a,b\right)=\frac{1}{\sqrt{a}}\int_{-\infty}^{\infty}f\left(t\right)\psi^{*}\left(\frac{t-b}{a}\right)dt, \qquad (3.19)$$

where a > 0.

The kernel of the wavelet transform

$$\psi_{a,b}(t) = \frac{1}{\sqrt{a}}\psi\left(\frac{t-b}{a}\right) \tag{3.20}$$

is determined by the shift and scaling of the mother wave $\psi(t)$.

The parameter *a* represents the scale variable in the wavelet transform, which is similar to the frequency variable in the Fourier transform. The value *b* represents the shift parameter. In the time domain, the quantity $\psi_{a,b}(t)$ is centered at *b* with a spread proportional to *a*. In this study, the relationship between the frequency ω and the scale variable *a* is $\omega = \omega_0/a$, where ω_0 is the center frequency, which is the dominant frequency of the mother wavelet. The function $\psi_{a,b}$ can be viewed as a window function in both the time and frequency domains, and we can change the size of the window by changing the variable a to obtain a suitable resolution. This multi-resolution is the main characteristic of wavelet analysis.

The wavelet function $\psi(t)$ satisfies the admissibility condition, which means that the integration C_ψ must be finite

$$C_\psi = \int_{-\infty}^{\infty} \frac{|\hat{\psi}(\omega)|^2}{|\omega|} d\omega < \infty, \tag{3.21}$$

where
$\hat{\psi}(\omega)$ denotes the Fourier transform of $\psi(t)$.

For further purposes, we can use the Garbor function

$$\psi_g(t) = \frac{1}{\pi^{0.25}}\sqrt{\frac{\omega_0}{\gamma}}\exp\left[-\frac{\left(\frac{\omega_0}{\gamma}\right)^2}{2}t^2\right]\cdot\exp(i\omega_0 t). \tag{3.22}$$

The Garbor function has good resolution in both the time and frequency domains.

The Fourier transform of the Garbor function can be represented as

$$\hat{\psi}_g(t) = \frac{\sqrt{2\pi}}{\pi^{0.25}} \sqrt{\frac{\gamma}{\omega_0}} \exp\left[-\frac{\left(\frac{\gamma}{\omega_0}\right)^2}{2} (\omega - \omega_0)^2 \right], \qquad (3.23)$$

where

$\gamma = \pi(2/ln2)^{0.5}$, $\omega_0 = 2\pi$.

The Garbor function can be thought of as a Gaussian window function centered at $t = 0$ in the time domain and at $\omega = \omega_0$ in the frequency domain.

If the Fourier transform $\hat{\psi}(\omega)$ has a center at $\omega = \omega_0$, and, accordingly, $\psi(t)$ is centered at $t = 0$, then the transform $\hat{\psi}_{a,b}(\omega)$ has a center corresponding to $\omega = \omega_0/a$ in the frequency domain and a center corresponding to b in the time domain.

Fourier transforms allow us to obtain the following relations

$$\hat{\psi}(\omega) = \int_{-\infty}^{\infty} \psi(t) \exp(-i\omega t) dt, \qquad (3.24)$$

$$\hat{\psi}_{a,b}(\omega) = \int_{-\infty}^{\infty} \frac{1}{\sqrt{a}} \psi\left(\frac{t-b}{a}\right) \exp(-i\omega t) dt. \qquad (3.25)$$

Considering this ratio, we can get

$$\hat{\psi}_{a,b}(\omega) = \frac{1}{\sqrt{a}} \int_{-\infty}^{\infty} \psi(\tau) \exp[i\omega(a\tau + b)] a\, d\tau =$$

$$= \sqrt{a}\, \hat{\psi}(a\omega) \exp(-i\omega b). \qquad (3.26)$$

Therefore, the maximum conversion value $\hat{\psi}(a\omega)$ corresponds to ω_0/a.

Let us consider the propagation of wave group velocity pulses. The transit times of samples made of composite materials, determined by the wavelet transform, are related to the group velocities. In general, the deformations at different points in response to a broadband load consist of a range of frequencies, so the wave can be assumed to propagate in an arbitrary direction, for example, x as follows

$$u(x,t)=\sum_{j=1}^{\infty}C_j\exp\left[-i\left(k_j x-\omega_j t\right)\right], \tag{3.27}$$

where
k_j is the wave number corresponding to each frequency ω_j of the j^{th} harmonic component.

Let us consider two harmonic waves of equal unit amplitude and several different frequencies ω_1 and ω_2, propagating in the direction x

$$u(x,t)=\exp\left[-i(k_1 x-\omega_1 t)\right]+\exp\left[-i(k_2 x-\omega_2 t)\right]. \tag{3.28}$$

The restrictions imposed on the wave numbers have the form

$$\frac{k_1+k_2}{2}=k_C,\quad \frac{k_1-k_2}{2}=\Delta k \tag{3.29}$$

$$\frac{\omega_1+\omega_2}{2}=\omega_C,\quad \frac{\omega_1-\omega_2}{2}=\Delta\omega. \tag{3.30}$$

Then equation (3.28) can be written as

$$\begin{aligned}u(x,t)&=\exp\left[-i(k_C+\Delta k)x-(\omega_C+\Delta\omega)t\right]+\\&+\exp\left[-i(k_C-\Delta k)x-(\omega_C-\Delta\omega)t\right]=\\&=2\cos(\Delta k\,x-\Delta\omega t)\exp\left[-i(k_C x-\omega_C t)\right].\end{aligned} \tag{3.31}$$

Formula (3.31) describes the base wave with frequency ω_C and phase velocity ω_C/k_C and modulation $cos\ (\Delta kx - \Delta\omega t)$ with frequency $\Delta\omega$ and propagation speed $\Delta\omega/\Delta k$. This wave can be described as a sequence of moving shocks (or groups, or wave packets). Phase and group velocities are designated c_P and c_g, respectively.

The relationships between these velocities correspond to the following situations: A) $c_g > c_P$: wavelets appear in front of the group and disappear at the end of the group; B) $c_g < c_P$: wavelets accumulate at the end of the group, move through the group and disappear at the front.

Now we can analytically specify the time it takes for the wavelet transform to pass through a sample of a composite material. The wavelet transform $u(x,t)$ provided that the Gabor wavelet is used as the mother wavelet, can be written as follows

$$WT_u(x,a,b)=\frac{1}{\sqrt{a}}\int_{-\infty}^{\infty}\psi_g\left(\frac{t-b}{a}\right)\exp\left[-i(k_1x-\omega_1t)\right]dt+$$

$$+\frac{1}{\sqrt{a}}\int_{-\infty}^{\infty}\psi_g\left(\frac{t-b}{a}\right)\exp\left[-i(k_2x-\omega_2t)\right]dt=$$

$$=\frac{1}{\sqrt{a}}\exp(-ik_1x)\int_{-\infty}^{\infty}\psi_g\left(\frac{t-b}{a}\right)\exp(i\omega_1t)dt+$$

$$+\frac{1}{\sqrt{a}}\exp(-ik_2x)\int_{-\infty}^{\infty}\psi_g\left(\frac{t-b}{a}\right)\exp(i\omega_2t)dt. \qquad (3.32)$$

Let us introduce the following notation: $\eta = (t - a)/b$.
Then for the wavelet transform WT_u (x, a, b) we can write:

$$WT_u(x,a,b)=\frac{1}{\sqrt{a}}\exp(-ik_1x)\int_{-\infty}^{\infty}\psi_g(\eta)\exp\left[i\omega_1(\eta a+b)\right]ad\eta+$$

$$+\frac{1}{\sqrt{a}}\exp(-ik_2x)\int_{-\infty}^{\infty}\psi_g(\eta)\exp\left[i\omega_2(\eta a+b)\right]ad\eta=$$

$$=\sqrt{a}\exp\left[-i(k_1x-\omega_1b)\right]\int_{-\infty}^{\infty}\psi_g(\eta)\exp(i\omega_1\eta a)d\eta+$$

$$+\sqrt{a}\exp\left[-i(k_2x-\omega_2b)\right]\int_{-\infty}^{\infty}\psi_g(\eta)\exp(i\omega_2\eta a)d\eta=$$

$$=\sqrt{a}\exp\left[-i(k_1x-\omega_1b)\right]\hat{\psi}_g(a\omega_1)+$$

$$+\sqrt{a}\exp\left[-i(k_2x-\omega_2b)\right]\hat{\psi}_g(a\omega_2). \qquad (3.33)$$

Now we can enter variables:

$$\varphi_1 = \omega_1 b - k_1 x, \qquad \varphi_2 = \omega_2 b - k_2 x. \tag{3.34}$$

Then we will get

$$\left|WT_u(x,a,b)\right| = \sqrt{a}\left|\hat{\psi}_g(a\omega_1)\exp(i\varphi_1) + \hat{\psi}_g(a\omega_2)\exp(i\varphi_2)\right|. \tag{3.35}$$

$$\left|WT_u(x,a,b)\right| = \sqrt{a}\ \Big|\ \left[\hat{\psi}_g(a\omega_1)\right]^2 + \left[\hat{\psi}_g(a\omega_2)\right]^2 +$$

$$+ 2\hat{\psi}_g(a\omega_1)\hat{\psi}_g(a\omega_2)\cos(\varphi_1 - \varphi_2)\ \Big|^{0.5} =$$

$$= \sqrt{a}\ \Big|\ \left[\hat{\psi}_g(a\omega_1)\right]^2 + \left[\hat{\psi}_g(a\omega_2)\right]^2 +$$

$$+ 2\hat{\psi}_g(a\omega_1)\hat{\psi}_g(a\omega_2)\cos(\Delta\omega b - \Delta k\, x)\ \Big|^{0.5}. \tag{3.36}$$

The following formulas should be considered valid

$$\hat{\psi}_g(a\omega_1) \cong \hat{\psi}_g(a\omega_2) \cong \hat{\psi}_g(a\omega_C). \tag{3.37}$$

In this case we can write:

$$\left|WT_u(x,a,b)\right| = \sqrt{a}\ \hat{\psi}_g(a\omega_C)\cdot\left[1 + 2\cos(\Delta\omega b - \Delta k\, x)\right]. \tag{3.38}$$

Calculating the peak values for $\hat{\psi}_g(a,\omega_C)$ and [1+*cos*(*Δω*b - *Δk* x*)*] allows us to obtain the peak value for the wavelet coefficient. The value $\hat{\psi}_g(a,\omega_C)$ is centered on the value $\omega = \omega_0/a$. Therefore, the argument in brackets will be maximum at $\Delta\omega/\Delta k = x/b$ or

$$c_g = \frac{x}{b}. \tag{3.39}$$

Therefore, we can conclude that the time shift b, maximizing the wavelet transform coefficient, should be the arrival time of the envelope wave at the circular frequency ω, related to the scale *a* by the relation $\omega = \omega_0/a$ for the coordinate *x*.

The results of calculating the arrival times of wavelet transform pulses of recoded signals are shown in the following Figures 8 - 9. Arrival times τ' and

frequencies f' are given in relative units for characteristic values $\tau_0 = 10^{-3}$ s and $f_0 = 9.5 \cdot 10^3$ Hz. The ratio of the dimensionless characteristic size of inclusions to the average distance between the nearest particles of a two-component composite (samples: *X1 – X3*, *X* = *A*, *B*, *C*) varied in the range $r' \in (1.6 – 2.2)$.

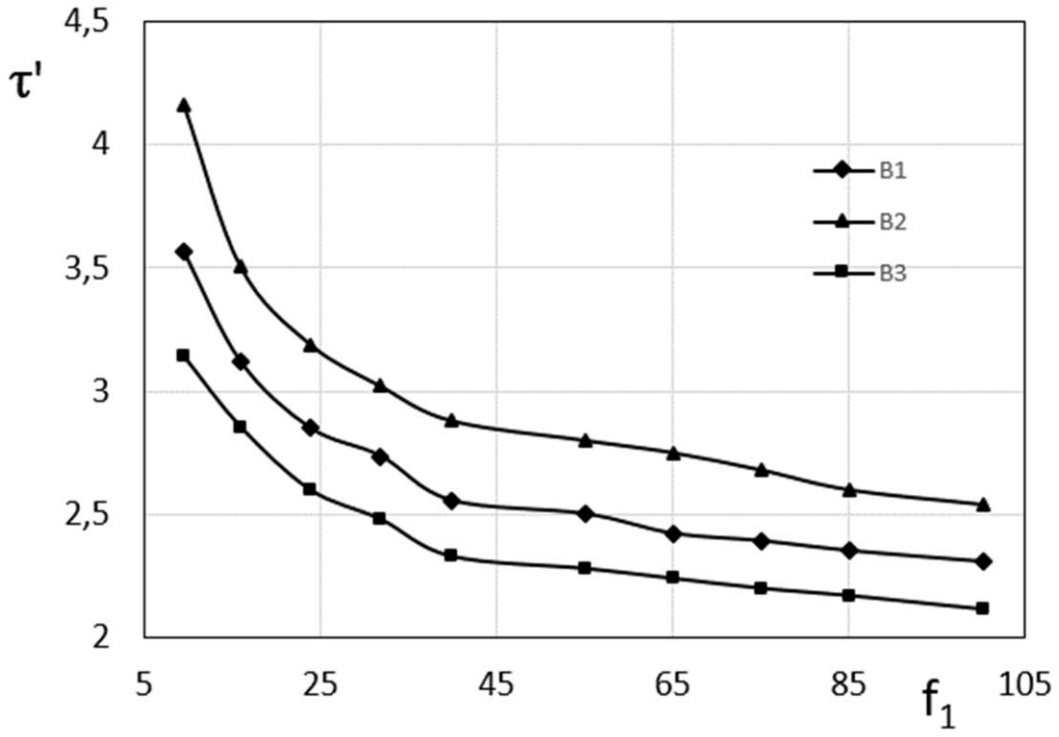

Figure 8. Spectral distribution of arrival time for a two-component composite with r′ = 1.9.

Solution of the inverse problem, i.e. estimating the location of a point load requires drawing up a set of nonlinear equations. Direct computational methods lead to difficulty in determining the location of the point load, the direction of the scattering waves, and the magnitude of the group velocities. Therefore, it is useful to study wave propagation in samples consisting of two-component composite materials and dispersion relations, as well as to find the relationship between the direction of propagating waves and velocities.

It follows that this technique requires a detailed check of the dispersion relationship in a plate or beam of a composite structure. Plate theories are the most common methods for deriving dispersion relations. One approach to solving the problem of wave scattering in plates is to represent the scattered field by expanding the wave function. To represent the scattered wave field as a wave function expansion, it is necessary to establish the eigenfunctions of displacement and voltage. Dispersion equation for a homogeneous isotropic plate using elasticity equations.

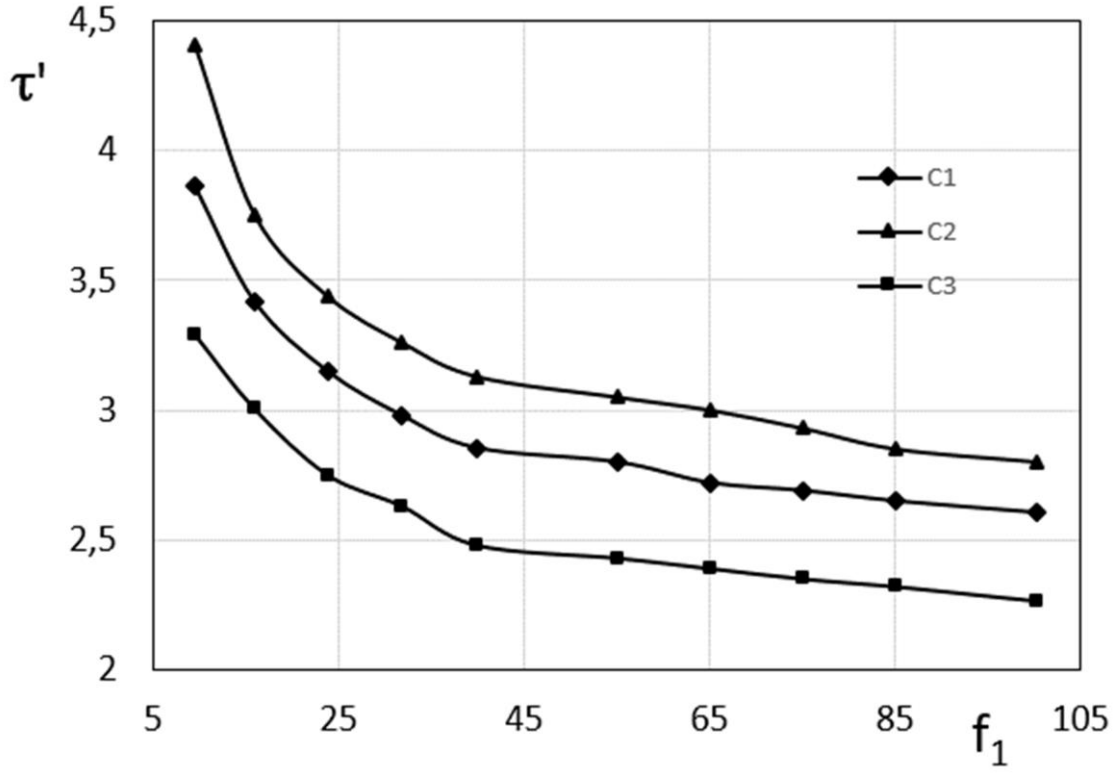

Figure 9. Spectral distribution of arrival time for a two-component composite with r′ = 2.2.

To represent the scattered wave field as a wave function expansion, it is necessary to establish the eigenfunctions of displacement and voltage.

Let us consider the dispersion wave relations in the plates according to Midlin's theory. Midlin's theory takes into account the effects of shear and rotational inertia. Here we consider a composite plate in the *x*-*y* plane without external loads. It is assumed that the displacements have the following coordinate components

$$u(x,y,z) = u^0(x,y,t) + z\psi_x(x,y,t) \tag{3.40}$$

$$v(x,y,z) = v^0(x,y,t) + z\psi_y(x,y,t) \tag{3.41}$$

$$w(x,y,z) = w^0(x,y,t)\,, \tag{3.42}$$

where

u, v, w are displacements of a point at (x,y,z) on the plate;

u^0, v^0, w^0 defines the displacements of the mid plane;

ψ_x, ψ_y are cross section rotations.

The generalized in-plane stress resultants (N_x, N_y and N_{xy}) and the generalized bending moments (M_x, M_y and M_{xy} are defined as in classical plate theory in vector form

$$\vec{N} = \begin{Bmatrix} N_x \\ N_y \\ N_z \end{Bmatrix}, \qquad \vec{M} = \begin{Bmatrix} M_x \\ M_y \\ M_z \end{Bmatrix}. \tag{3.43}$$

The relative dimensionless shift relations have the form

$$\varepsilon_x = \frac{\partial u}{\partial x}, \quad \varepsilon_y = \frac{\partial \nu}{\partial y}, \; \gamma_{xy} = \frac{\partial u}{\partial y} + \frac{\partial \nu}{\partial x}. \tag{3.44}$$

Now we can rewrite the equations (3.44)

$$\varepsilon_x = \varepsilon_x^0 + z\kappa_x \tag{3.45}$$

$$\varepsilon_y = \varepsilon_y^0 + z\kappa_y \tag{3.46}$$

$$\gamma_{xy} = \gamma_{xy}^0 + z\kappa_{xy}, \tag{3.47}$$

where

ε_x, ε_y, ε_z are strain components;

superscript 0 denotes the mid plane.

Strain (ε_x^0, ε_y^0 and γ_{xy}^0) and curvature (κ_x, κ_y and κ_{xy}) can be defined as

$$\varepsilon_x^0 = \frac{\partial u^0}{\partial x}, \quad \varepsilon_y^0 = \frac{\partial \nu^0}{\partial y}, \quad \gamma_{xy}^0 = \frac{\partial u^0}{\partial y} + \frac{\partial \nu^0}{\partial x} \tag{3.48}$$

$$\kappa_x = \frac{\partial \psi_x}{\partial x}, \quad \kappa_y = \frac{\partial \psi_y}{\partial y}, \quad \kappa_{xy} = \frac{\partial \psi_x}{\partial y} + \frac{\partial \psi_y}{\partial x}. \tag{3.49}$$

For further transformations it is necessary to introduce the following notation

$$\vec{\varepsilon} = \begin{Bmatrix} \varepsilon_x \\ \varepsilon_y \\ \varepsilon_z \end{Bmatrix}, \qquad \vec{\kappa} = \begin{Bmatrix} \kappa_x \\ \kappa_y \\ \kappa_z \end{Bmatrix}. \tag{3.50}$$

Then the ratio of mechanical stress and deformation in a sample of a two-component composite has the form

$$\begin{Bmatrix} \vec{N} \\ \vec{M} \end{Bmatrix} = \begin{bmatrix} \mathbf{A} & \mathbf{B} \\ \mathbf{B} & \mathbf{D} \end{bmatrix} \cdot \begin{Bmatrix} \vec{\varepsilon} \\ \vec{\kappa} \end{Bmatrix} \tag{3.51}$$

where submatrices ***A*** known as extensional stiffness, ***B***, bending-extension stiffness, and ***D*** bending stiffness are defined as

$$\mathbf{A} = \begin{bmatrix} A_{11} & A_{12} & A_{16} \\ A_{12} & A_{22} & A_{26} \\ A_{16} & A_{26} & A_{66} \end{bmatrix} \qquad \mathbf{B} = \begin{bmatrix} B_{11} & B_{12} & B_{16} \\ B_{12} & B_{22} & B_{26} \\ B_{16} & B_{26} & B_{66} \end{bmatrix}$$

$$\mathbf{D} = \begin{bmatrix} D_{11} & D_{12} & D_{16} \\ D_{12} & D_{22} & D_{26} \\ D_{16} & D_{26} & D_{66} \end{bmatrix}, \tag{3.52}$$

where

$$A_{ji} = \sum_{1}^{N} \left(\overline{Q}_{ij}\right)_k \left(Z_k - Z_{k-1}\right)$$

$$B_{ji} = \frac{1}{2} \sum_{1}^{N} \left(\overline{Q}_{ij}\right)_k \left(Z_k^2 - Z_{k-1}^2\right)$$

$$D_{ji} = \frac{1}{3} \sum_{1}^{N} \left(\overline{Q}_{ij}\right)_k \left(Z_k^3 - Z_{k-1}^3\right). \tag{3.53}$$

And $\overline{Q_{ij}}$ are the transformations of stiffness matrix Q_{ij}:

$$Q_{11} = \frac{E_1}{1-\nu_{12}\nu_{21}} \qquad Q_{12} = \frac{\nu_{12}E_2}{1-\nu_{12}\nu_{21}}$$

$$Q_{22} = \frac{E_2}{1-\nu_{12}\nu_{21}} \qquad Q_{66} = G_{12}$$

$$Q_{44} = G_{23} \quad Q_{55} = G_{31} \quad Q_{45} = G_{23} - G_{31}. \tag{3.54}$$

Applying the definition of the resultants of the transverse force, we obtain an additional constitutive relation that includes the transverse shear.

Let us introduce the parameter *k* into this defining relation for the transverse shear and obtain

$$\begin{Bmatrix} q_{yz} \\ q_{xz} \end{Bmatrix} = k \begin{bmatrix} A_{44} & A_{45} \\ A_{45} & A_{55} \end{bmatrix} \begin{Bmatrix} \gamma_{yz} \\ \gamma_{xz} \end{Bmatrix}, \tag{3.55}$$

where interlaminar shear strains are determined by the relations

$$\gamma_{xz} = \frac{\partial u}{\partial z} + \frac{\partial w}{\partial x} = \psi_x + \frac{\partial w}{\partial x}$$

$$\gamma_{yz} = \frac{\partial \nu}{\partial z} + \frac{\partial w}{\partial y} = \psi_y + \frac{\partial w}{\partial y}. \tag{3.56}$$

The shear correction factor (*k*) is chosen to be 5/6. Using the fundamental equations of motion in terms of resultant stresses and moments, we have

$$\frac{\partial N_x}{\partial x} + \frac{\partial N_{xy}}{\partial y} = \rho h \frac{\partial^2 u^0}{\partial t^2} \tag{3.57}$$

$$\frac{\partial N_{xy}}{\partial x} + \frac{\partial N_y}{\partial y} = \rho h \frac{\partial^2 \nu^0}{\partial t^2} \tag{3.58}$$

$$\frac{\partial M_x}{\partial x}+\frac{\partial M_{xy}}{\partial y}-q_{xz}=I\frac{\partial^2\psi_x}{\partial t^2} \tag{3.59}$$

$$\frac{\partial M_{xy}}{\partial x}+\frac{\partial M_y}{\partial y}-q_{yz}=I\frac{\partial^2\psi_y}{\partial t^2} \tag{3.60}$$

$$\frac{\partial q_{xz}}{\partial x}+\frac{\partial q_{yz}}{\partial y}=\rho h\frac{\partial^2 w}{\partial t^2}, \tag{3.61}$$

where *I* is the mass moment of inertia.

Using the equations of motion and previous formulas, we can obtain the following relations

$$A_{11}\frac{\partial^2 u^0}{\partial x^2}+2A_{16}\frac{\partial^2 u^0}{\partial x\partial y}+A_{66}\frac{\partial^2 u^0}{\partial y^2}+A_{16}\frac{\partial^2 v^0}{\partial x^2}+\left(A_{12}+A_{66}\right)\frac{\partial^2 v^0}{\partial x\partial y}+$$

$$+A_{26}\frac{\partial^2 v^0}{\partial y^2}+B_{11}\frac{\partial^2\psi_x}{\partial x^2}+2B_{16}\frac{\partial^2\psi_x}{\partial x\partial y}+B_{66}\frac{\partial^2\psi_x}{\partial y^2}+B_{16}\frac{\partial^2\psi_y}{\partial x^2}+$$

$$+\left(B_{12}+B_{66}\right)\frac{\partial^2\psi_y}{\partial x\partial y}+B_{26}\frac{\partial^2\psi_y}{\partial y^2}=\rho h\frac{\partial^2 u^0}{\partial t^2} \tag{3.62}$$

$$A_{16}\frac{\partial^2 u^0}{\partial x^2}+\left(A_{12}+A_{66}\right)\frac{\partial^2 u^0}{\partial x\partial y}+A_{26}\frac{\partial^2 u^0}{\partial y^2}+A_{66}\frac{\partial^2 v^0}{\partial x^2}+2A_{26}\frac{\partial^2 v^0}{\partial x\partial y}+$$

$$+A_{22}\frac{\partial^2 v^0}{\partial y^2}+B_{16}\frac{\partial^2\psi_x}{\partial x^2}+\left(B_{12}+B_{66}\right)\frac{\partial^2\psi_x}{\partial x\partial y}+B_{26}\frac{\partial^2\psi_x}{\partial y^2}+B_{66}\frac{\partial^2\psi_y}{\partial x^2}+$$

$$2B_{26}\frac{\partial^2\psi_y}{\partial x\partial y}+B_{22}\frac{\partial^2\psi_y}{\partial y^2}=\rho h\frac{\partial^2 v^0}{\partial t^2} \tag{3.63}$$

$$B_{11}\frac{\partial^2 u^0}{\partial x^2}+2B_{16}\frac{\partial^2 u^0}{\partial x\partial y}+B_{66}\frac{\partial^2 u^0}{\partial y^2}+B_{16}\frac{\partial^2 v^0}{\partial x^2}+\left(B_{12}+B_{66}\right)\frac{\partial^2 v^0}{\partial x\partial y}+$$

$$+B_{26}\frac{\partial^2 v^0}{\partial y^2}+D_{11}\frac{\partial^2 \psi_x}{\partial x^2}+2D_{16}\frac{\partial^2 \psi_x}{\partial x\partial y}+D_{66}\frac{\partial^2 \psi_x}{\partial y^2}+D_{16}\frac{\partial^2 \psi_y}{\partial x^2}+$$

$$+\left(D_{12}+D_{66}\right)\frac{\partial^2 \psi_y}{\partial x\partial y}+D_{26}\frac{\partial^2 \psi_y}{\partial y^2}-$$

$$-k\left[A_{55}\left(\psi_x+\frac{\partial w}{\partial x}\right)+A_{45}\left(\psi_y+\frac{\partial w}{\partial y}\right)\right]=I\frac{\partial^2 \psi_x}{\partial t^2} \qquad (3.64)$$

$$B_{16}\frac{\partial^2 u^0}{\partial x^2}+\left(B_{12}+B_{66}\right)\frac{\partial^2 u^0}{\partial x\partial y}+B_{26}\frac{\partial^2 u^0}{\partial y^2}+B_{66}\frac{\partial^2 v^0}{\partial x^2}+2B_{26}\frac{\partial^2 v^0}{\partial x\partial y}+$$

$$+B_{22}\frac{\partial^2 v^0}{\partial y^2}+D_{16}\frac{\partial^2 \psi_x}{\partial x^2}+\left(D_{12}+D_{66}\right)\frac{\partial^2 \psi_x}{\partial x\partial y}+D_{26}\frac{\partial^2 \psi_x}{\partial y^2}+$$

$$+D_{66}\frac{\partial^2 \psi_y}{\partial x^2}+2D_{26}\frac{\partial^2 \psi_y}{\partial x\partial y}+D_{22}\frac{\partial^2 \psi_y}{\partial y^2}-$$

$$-k\left[A_{45}\left(\psi_x+\frac{\partial w}{\partial x}\right)+A_{44}\left(\psi_y+\frac{\partial w}{\partial y}\right)\right]=I\frac{\partial^2 \psi_y}{\partial t^2} \qquad (3.65)$$

$$k\left[A_{55}\left(\frac{\partial \psi_x}{\partial x}+\frac{\partial^2 w}{\partial x^2}\right)+A_{45}\left(\frac{\partial \psi_x}{\partial y}+\frac{\partial \psi_y}{\partial x}+2\frac{\partial^2 w}{\partial x\partial y}\right)+\right.$$

$$\left.+A_{44}\left(\frac{\partial \psi_y}{\partial y}+\frac{\partial^2 w}{\partial y^2}\right)\right]=\rho h\frac{\partial^2 w}{\partial t^2}. \qquad (3.66)$$

In the case of harmonic wave propagation, it is further assumed that the displacement functions take the form

$$\left(u^0, v^0, w^0, \psi_x, w_y\right) = \left(U, V, W, \Psi_x, \Psi_y\right) \cdot$$

$$\cdot \exp\left[i\left(k_x x + k_y y - \omega t\right)\right], \qquad (3.67)$$

where
the capital letters are complex-valued constants;
k_x, k_y are the x and y-components of the wave vector, respectively;
ω is the circular frequency.

Substituting equation (3.65) into the equations of motion (in particular, into equations (3.60) – (3.64) for a laminated two-component composite gives the following generalized eigenvalue problem:

$$\left(\begin{bmatrix} K_{11} & K_{12} & K_{13} & K_{14} & K_{15} \\ K_{12} & K_{22} & K_{23} & K_{24} & K_{25} \\ K_{13} & K_{23} & K_{33} & K_{34} & K_{35} \\ K_{14} & K_{24} & -K_{34} & K_{44} & K_{45} \\ K_{15} & K_{25} & -K_{35} & K_{45} & K_{55} \end{bmatrix} - \right.$$

$$\left. -\omega^2 \begin{bmatrix} \rho h & 0 & 0 & 0 & 0 \\ 0 & \rho h & 0 & 0 & 0 \\ 0 & 0 & \rho h & 0 & 0 \\ 0 & 0 & 0 & \dfrac{\rho h^3}{12} & 0 \\ 0 & 0 & 0 & 0 & \dfrac{\rho h^3}{12} \end{bmatrix} \right) \begin{Bmatrix} U \\ V \\ W \\ \psi_x \\ \psi_y \end{Bmatrix} = \begin{Bmatrix} 0 \\ 0 \\ 0 \\ 0 \\ 0 \end{Bmatrix}, \qquad (3.68)$$

where ρ is the density that is assumed to be the same in all layers of a composite material sample;
h is the thickness of the laminar composite sample.

The K_{ij} coefficients depend on the wave vector and stiffening elements of the laminar composite sample and are determined by the following relations

$$K_{11} = A_{11}k_x^2 + 2A_{16}k_xk_y + A_{66}k_y^2,$$

$$K_{12} = A_{16}k_x^2 + (A_{12} + A_{66})k_xk_y + A_{26}k_y^2, \quad K_{13} = 0,$$

$$K_{14} = B_{11}k_x^2 + 2B_{16}k_xk_y + B_{66}k_y^2,$$

$$K_{15} = B_{16}k_x^2 + (B_{12} + B_{66})k_xk_y + B_{26}k_y^2,$$

$$K_{22} = A_{66}k_x^2 + 2A_{26}k_xk_y + A_{22}k_y^2, \quad K_{23} = 0,$$

$$K_{24} = B_{16}k_x^2 + (B_{12} + B_{66})k_xk_y + B_{26}k_y^2,$$

$$K_{25} = B_{66}k_x^2 + 2B_{26}k_xk_y + B_{22}k_y^2,$$

$$K_{33} = A_{55}kk_x^2 + 2A_{45}kk_xk_y + A_{44}kk_y^2,$$

$$K_{34} = -i(A_{55}kk_x + A_{45}kk_y),$$

$$K_{35} = -i(A_{44}kk_y + A_{45}kk_x),$$

$$K_{44} = D_{11}k_x^2 + 2D_{16}k_xk_y + D_{66}k_y^2 + A_{55}k,$$

$$K_{45} = D_{16}k_x^2 + (D_{12} + D_{66})k_xk_y + D_{26}k_y^2 + A_{45}k,$$

$$K_{55} = D_{66}k_x^2 + 2D_{26}k_xk_y + D_{22}k_y^2 + A_{44}k. \qquad (3.69)$$

For given wave vector components k_x and k_y the generalized eigenvalue problem of equation (3.66) gives five eigenfrequencies, which are real ω, since K is a Hermitian matrix. In addition, it should be borne in mind that the elements K_{34} and K_{35} are purely imaginary quantities.

Knowing the dependence of ω on k_x and k_y, the phase and group velocities are determined from the relations

$$c_P = \frac{\omega}{k}, \qquad c_g = \frac{d\omega}{dk}. \tag{3.70}$$

For the convenience of further calculations, the dimensionless phase velocity and circular frequency are defined as

$$\hat{c}_P = \frac{\omega}{k}\sqrt{\frac{\rho}{E_1}} \tag{3.71}$$

$$\hat{\omega} = \omega\sqrt{\frac{\rho h^2}{E_1}}\ . \tag{3.72}$$

The first three modes obtained in the calculations are acoustic modes, which can also propagate at lower frequencies. The lowest of them corresponds to the bending mode, the second to the planar shear, and the third to the tensile mode. The frequency at which the other two modes, known as optical modes, begin to propagate is called the cutoff frequency, and these modes are related to ψ_x and ψ_y, which are the rotations of the cross section.

In this study, the first acoustic mode, which is the lateral deflection W, was analyzed and its group and phase velocities are shown in Figures 10 to 13 for composite plates. For composite plate type 1 we have three axes of symmetry around $\vartheta = 0^0, 45^0, 90^0$, and for composite plate 2 we have two axes of symmetry around $\vartheta = 0^0, 90^0$, and this fact is clearly shown in these pictures.

The phase velocity for a composite of the first type ceases to change significantly at $\omega_s = 1.2\cdot10^6$. The phase velocities of the second type composite sample practically reach saturation at $\omega_s = 1.5\cdot10^6$. The numerical value of the saturation frequency for group velocity increases compared to the case of phase velocity and is $\omega_s = 3.2\cdot10^6$ for the first sample and $\omega_s = 4.3\cdot10^6$ for the second sample.

The components of the wave vector satisfy the equation

$$\theta = \arctan\left(\frac{k_y}{k_x}\right), \tag{3.73}$$

where

θ is the wave propagation angle.

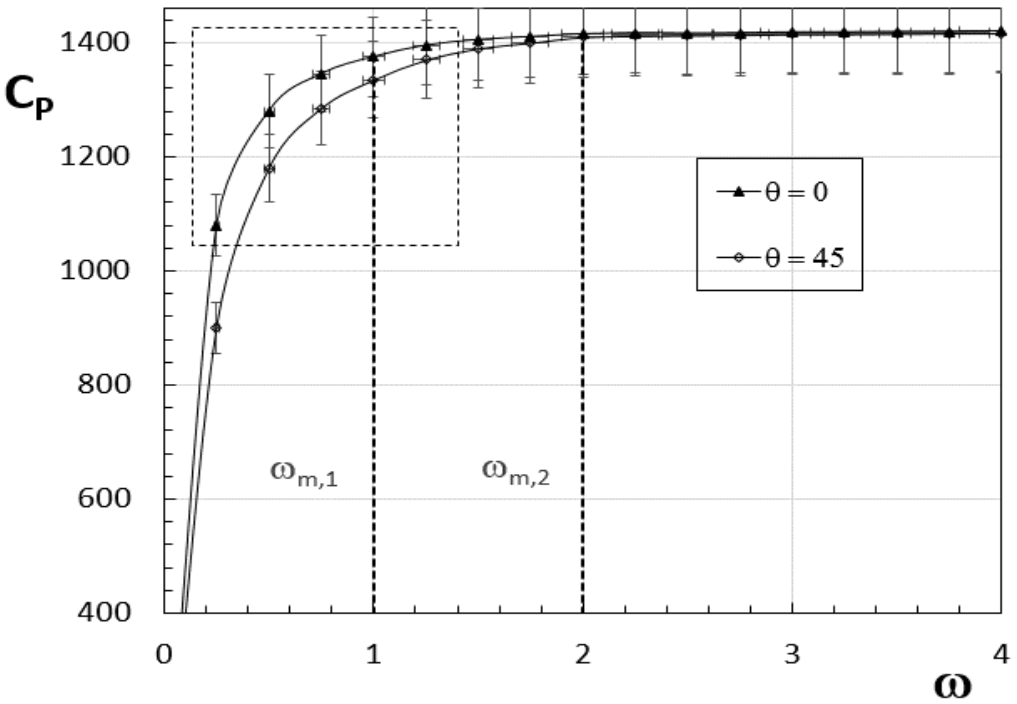

Figure 10. Phase velocity of the first acoustic mode in composite 1.

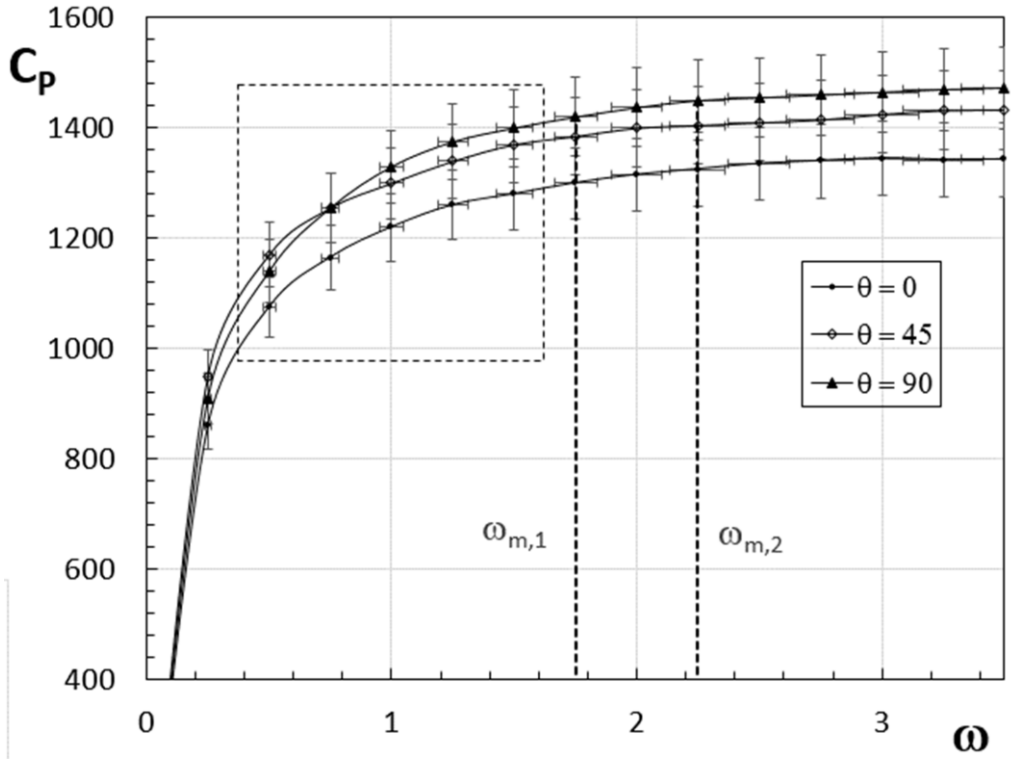

Figure 11. Phase velocity of the first acoustic mode in composite 2.

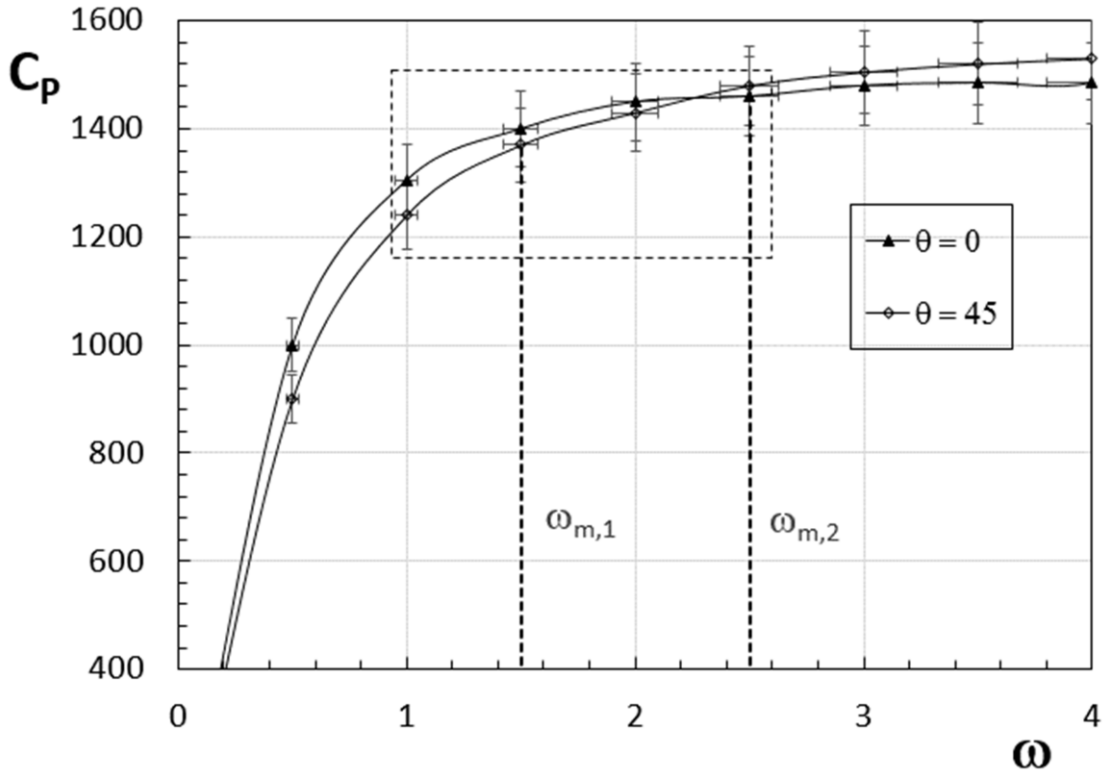

Figure 12. Group velocity of the first acoustic mode in composite 1.

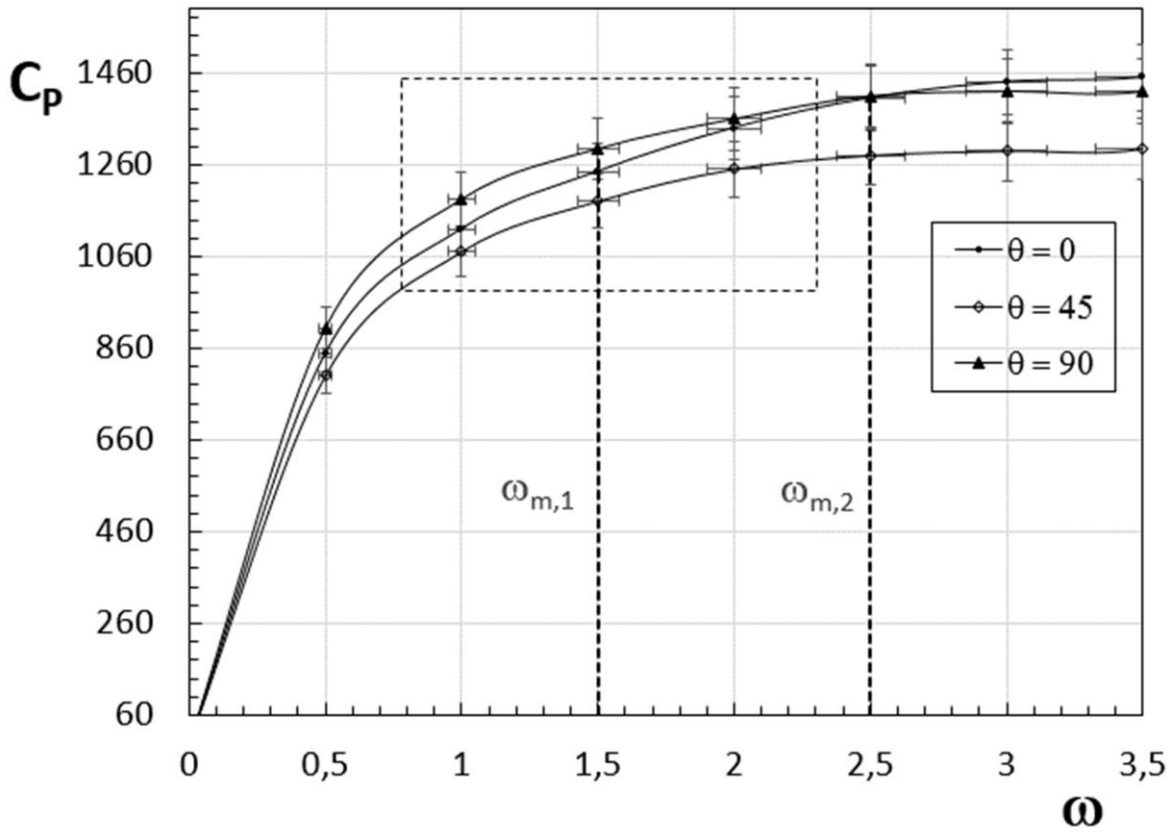

Figure 13. Group velocity of the first acoustic mode in composite 2.

Mathematically, the wavelet transform can be understood as the inner product of the recorded signal and the wavelet function in a function space that measures the similarity between the waveform and the wavelet function. When the parameters *a* and *b* are the values to which the waveform and wavelet function best fit, the calculations yield the maximum value of the wavelet coefficient. The time shift that maximizes the inner product of the wavelet function for scale a and the signal recorded at each sensor is the arrival time associated with the frequency associated with that scale, the relation

$$\omega = \frac{\omega_0}{a\,\Delta t} \quad \text{or} \quad f = \frac{f_0}{a\,\Delta t}. \tag{3.74}$$

To estimate the location of the applied load, it is necessary to use the arrival times of the dominant frequency content of the signal, specified using the presented wavelet approach, and also formulate a system of nonlinear equations. For the case of a composite plate, the velocities from the dispersion relations are used.

In addition, it is necessary to use a system of nonlinear equations and solve it with respect to the unknowns ϑ_i. Without loss of generality, the point load is shown within a triangular sensor arrangement. The same equations will apply for the non-triangular impact load case, taking into account the convention of the signs of the angles. Having found the time of arrival at each sensor S_i for frequency *f*, we can find

$$\Delta t_{12}(f) = t_1(f) - t_2(f) = \frac{l_1}{C_{g1}(f)} - \frac{l_2}{C_{g2}(f)} \tag{3.75}$$

$$\Delta t_{23}(f) = t_2(f) - t_3(f) = \frac{l_1}{C_{g2}(f)} - \frac{l_2}{C_{g3}(f)}, \tag{3.76}$$

where

l_i is the distance between sensor *i* and the impact location;

Δt_{ij} is the arrival time difference between points *i* and *j*;

t_i is the arrival time to point *i*;

C_{gi} is the group velocity in the θ_i direction.

The position of the composite material sample and the fixation of the wave arrival registration points is determined by the triple of angles θ_1, θ_2 and θ_3 for which we can write the relations

$$l_1 \sin(\theta_1) = l_2 \sin(\theta_2) \tag{3.77}$$

$$l_1 \cos(\theta_1) + l_2 \cos(\theta_2) = S_1 S_2 \tag{3.78}$$

from here we get

$$l_1 = \frac{S_1 S_2}{\sin(\theta_1) \cdot [\cot g(\theta_1) + \cot g(\theta_2)]} \tag{3.79}$$

$$l_2 = \frac{S_1 S_2}{\sin(\theta_2) \cdot [\cot g(\theta_1) + \cot g(\theta_2)]}, \tag{3.80}$$

where
S_iS_j is the distance between points *i* and *j*.

By writing the same equations for l_2, l_3, θ_2 and θ_3, we have

$$l_2' = \frac{S_2 S_3}{\sin(\hat{S}_2 - \theta_2) \cdot [\cot g(\theta_3) + \cot g(\hat{S}_2 - \theta_2)]} \tag{3.81}$$

$$l_3 = \frac{S_2 S_3}{\sin(\theta_3) \cdot [\cot g(\theta_3) + \cot g(\hat{S}_2 - \theta_2)]}. \tag{3.82}$$

Let's substitute equations (3.77) – (3.80) into equations (3.73), (3.74)

$$\frac{1}{\cot g(\theta_1) + \cot g(\theta_2)} \left(\frac{1}{\sin(\theta_1) c g_1} - \right.$$

$$\left. - \frac{1}{\sin(\theta_2) c g_2} \right) - \frac{\Delta t_{12}}{S_1 S_2} = 0 \tag{3.83}$$

$$\frac{1}{\cot g(\theta_3) + \cot g(\hat{S}_2 - \theta_2)} \left(\frac{1}{\sin(\hat{S}_2 - \theta_2)\ c g_2} - \right.$$

$$-\frac{1}{\sin(\theta_3)cg_3}\Bigg)-\frac{\Delta t_{23}}{S_2S_3}=0\ , \tag{3.84}$$

where

$$\cot g(\theta_3)=\frac{S_2S_3\sin(\theta_2)\cdot[\cot g(\theta_1)+\cot g(\theta_2)]}{S_1S_2\sin(\hat{S}_2-\theta_2)}-\cot g(\hat{S}_2-\theta_2). \tag{3.85}$$

Solving the resulting set of nonlinear equations allows us to find ϑ_1 and ϑ_2, from which we can determine x_p and y_p, i.e., the coordinates of the load location for each frequency f.

The results obtained for samples made of two-component composite material are shown in Table 1. The given values indicate a decrease in arrival time with increasing frequency due to an increase in group velocities. Moreover, the results are in good agreement with the actual location of the applied load in the case of an anisotropic plate. Note that the error in estimating the coordinates of the load location is less than 1.2% for all different types of loading of both isotropic and anisotropic samples.

Table 1. Spatial distribution of applied load for composite plates

Composite		Wide Band Load, 10^3 Hz					Narrow Band Load, 10^3 Hz
		9.6	15.8	23.6	31.6	39.6	100.4
Sample 1	x	0.4877	0.4847	0.5025	0.4881	0.4877	0.5025
	y	0.6864	0.7059	0.7002	0.7040	0.6864	0.7002
Sample 2	x	0.4847	0.5025	0.5025	0.4881	0.5025	0.5025
	y	0.7059	0.7002	0.7002	0.7030	0.7002	0.7002

It should be noted that the processed sensor signals can differ significantly from the numerical simulation signals, and this is due to the fact that the data is often distorted by measurement noise. Let's consider the effect of noise on the results. An analytical consideration of the influence of noise on the results obtained can be presented as follows

$$y(t)=x(t)+n(t), \tag{3.86}$$

where
x is the original signal;
y is the noised signal;
n(*t*) is the measurement noise which can be expressed as

$$n(t) = r\,ms \cdot s \cdot r(t), \tag{3.87}$$

where
rms is the root mean square of the signal *x*;
r(*t*) is a function which generates arrays of random numbers whose elements are normally distributed with mean 0;
s is the noise level, i.e. a quantity inversely proportional to the signal-to-noise ratio.

Adding a certain percentage of white noise to the system and denoising the signal using the usual moving average method allows the described method to be used to determine the location of the impact. The results were tested for different noise levels (2% and 5%) and are shown in Tables 2 – 4.

Table 2. Spectral distribution of arrival time of noisy signals (composite type 1)

Frequency	23.8	31.8	39.8	23.8	31.8	39.8
Point	Arrival times, 10^{-4} s					
	Level 2%			Level 5%		
S_1	2.74	2.59	2.49	2.65	2.455	2.73
S_2	3.025	2.97	2.83	3.015	2.805	2.995
S_3	2.435	2.435	2.2	2.31	2.275	2.455

Table 3. Spectral distribution of arrival time of noisy signals (composite type 2)

Frequency, 10^3 Hz	23.8	31.8	39.8	23.8	31.8	39.8
Point	Arrival times, 10^{-4} s					
	Level 2%			Level 5%		
S_1	2.725	2.485	2.81	2.725	2.575	2.82
S_2	3.05	2.85	3.165	3.045	2.84	3.21
S_3	2.45	2.33	2.57	2.405	2.395	2.545

Table 4. Spatial distribution of applied load for signals contaminated by noise

Frequency, 10^3 Hz		9.6	15.8	23.6	31.6	39.6	100.4
		Location, 10^{-2} m					
Composite		Noise level 2%			Noise level 5%		
Sample 1	x	0.5176	0.4976	0.4980	0.4985	0.4976	0.5176
	y	0.7140	0.6898	0.7130	0.7199	0.6898	0.7140
Sample 2	x	0.5123	0.4978	0.5125	0.5128	0.5170	0.4981
	y	0.7106	0.6966	0.7106	0.7170	0.6897	0.7130

A general approach to solving the inverse problem of detecting sudden structural damage in isotropic and composite plates can be formulated as follows. The impulse load is the cause of the damage, then the numerical response data is presented in matrix form. The deformation maps are subject to wavelet transform analysis and, accordingly, the wavelet coefficient map of each signal is used to estimate the arrival time of the flexural waves by determining the peak value of the wavelet coefficients. The final stage is to determine the location of the applied load using a system of nonlinear equations.

The spread of directions in which group velocities change complicates the numerical analysis procedure. Therefore, to solve the problem, calculated group velocities from the dispersion relations of wave propagation are used.

CHAPTER 4
HAAR-WAVELETS

Haar wavelet methods, used to solve differential and integro-differential equations, are known for their simple implementation as well as their ability to capture local effects. Haar wavelets are generated from pairs of piecewise constant functions and are not differentiable. In the case of differential and integro-differential equations, the latter disadvantage can be overcome by regularizing quadratic waves (for example, smoothing using interpolating splines) or by expanding the higher derivative involved in the differential equation, namely, into a series of Haar functions instead of a solution.

The Haar wavelet transform technique has been successfully implemented to solve a wide class of problems covering solid mechanics, mathematical physics, evolutionary equations, nuclear reactor dynamics, numerical integration of multidimensional strongly and smoothly oscillating integrands, nonlinear differential equations with nonlocal boundary conditions, as well as singular perturbed two-point boundary value problems [113 – 122]. Among the analytical works devoted to the use of Haar wavelets, one can point out the works of Kumar and Majak. Experimental studies were carried out by Kim, Xie, Fan, Dai and others.

Fractional differential, integrodifferential and integral equations can be considered as a challenging area of research for the development and adaptation of numerical methods. In particular, Haar transforms are used to solve Volterra and Fredholm fractional integral equations, as well as fractional order differential equations involving harmonic vibrations. The Haar wavelet transform has been adapted to solve partial differential and integro-differential equations, respectively.

A large number of both analytical and experimental works on the analysis of structures made of composite materials were based on the Haar wavelet transform. In particular, the free vibrations of a multilayer composite plate and the delamination of a composite beam, respectively, were analyzed in sufficient detail. The Haar wavelet transform allows one to study functionally graded structures. A wide range of studies is devoted to vibration analysis of conical and cylindrical shells. Vibration analysis allows one to generate a general approach to solving boundary conditions.

It is known that layered composite shells of cylindrical, conical, spherical and biconvex shapes are widely used in many fields of technology. Over the past decades, many accurate and effective methods for studying the vibration characteristics of cylindrical shells have appeared. A significant number of analytical and experimental studies are devoted to the study of free vibrations of both conical shell structures and spherical shell structures, as well as shell structures of double curvature. However, many mechanical structures are made by combining individual shells. Because these structures operate under challenging conditions and under varying loads, it is important to clearly understand their vibration characteristics.

Calculus of variations methods underlie the analysis of free vibrations of various shell structures connected by conical, cylindrical and spherical shells. The behavior of free vibrations of a coupled shell structure with an arbitrary boundary condition is simplified by applying the Jacobi-Ritz method. In addition, with the same method it is possible to analyze the free and forced vibration of a sealed vessel associated with a volume that has a shape with a double curvature and a cylindrical shell. A large amount of research is devoted to free vibration, which is associated with a composite laminated shell.

Analysis of free vibrations of a connected composite layered shell of a cylindrical-conical or cylindrical-spherical structure involves the use of the spectral collocation method.

A local-global *B*-spline approach is used to analyze the vibration characteristics of a conical-cylindrical coupled shell. The local-global *B*-spline can be extended by using a wave solution in combination with a power series expansion approach. The Fourier spectrum element method is used to analyze free vibrations of conical-cylindrical spherical coupled shells with arbitrary boundary conditions.

Recently, because the Haar wavelet discretization approach has high accuracy and computational simplicity, it has been widely used in vibration analysis of various structures such as beams, plates, and shells. Therefore, the Haar wavelet transform is applied to analyze the free vibration of double composite laminar structures. To generalize boundary and continuous conditions, the artificial spring method is used. Natural frequencies of laminar structures are subject to a detailed analysis procedure.

Let us consider a theoretical model for the analysis of free vibrations of laminar composite structures, the equation of motion of a coupled shell, and a discretization method using the Haar method. Among other reasons and assumptions for this model, it should be mentioned that the individual shells that make up the paired shell are made of the same material and have the same thickness.

This model describes the behavior of a double laminated shell. The orthogonal coordinate system of the laminated shell is fixed to the middle surface, which is the geometric middle surface. In the meridional, circumferential and radial directions (φ, θ, z) the displacement shells are u, v and w. The symbols R_φ and R_θ denote the radii of curvature of the meridian and normal surfaces of a doubly curved shell. The distance between the geometric axis of the meridian curve C_0C_1 and the z axis of rotation is defined as R_s, O_φ and O_θ - center points of the two main radii of curvature (R_φ, R_θ).

The doubly curved shell contains elliptic, parabolic and hyperbolic shells, which are commonly used in practice. The individual shells are connected by a continuous state. The quantities $\varphi_{l,r}$, $\theta_{l,r}$, $z_{l,r}$ serve as the basis for the coordinate system for the left and right shells of double curvature, and the quantities x_c, θ_c, z_c allow us to determine the coordinate system for the middle cylindrical shell, in which the indices l, c, r mean left, middle and right shells in a paired shell, respectively. The

displacements of individual shells in the direction φ, θ, z are equal to u_ζ, v_ζ, w_ζ (ζ= *l*, *c*, *r*). It is assumed that both ends of the connected shell are supported by artificial springs. There are three linear springs and two rotational springs at both end boundaries, and the boundary conditions are determined depending on the stiffness of these springs.

For an elliptical shell of double curvature, we can write the following relations

$$R_\varphi(\varphi)=\frac{a^2b^2}{\sqrt{\left(a^2\sin^2\varphi+b^2\cos^2\varphi\right)^3}}$$

$$R_\theta(\varphi)=\frac{a^2}{\sqrt{a^2\sin^2\varphi+b^2\cos^2\varphi}}+\frac{R_S}{\sin\varphi},\quad a=R_C,\qquad b=L_{l,r}, \tag{4.1}$$

where

a, *b* are the length of the semimajor and semiminor axes of the elliptic meridian, respectively.

Besides

$$\varphi_0=\arctan\left(\frac{bR_0}{a\sqrt{a^2-R_0^2}}\right),\quad \varphi_1=\arctan\left(\frac{bR_1}{a\sqrt{a^2-R_1^2}}\right). \tag{4.2}$$

For a parabolic shell of doubly curvature, we can write

$$R_\varphi(\varphi)=\frac{k}{2\cos^3\varphi},\qquad R_\theta(\varphi)=\frac{k}{2\cos\varphi}+\frac{R_S}{\sin\varphi}, \tag{4.3}$$

where *k* is the characteristic parameter of the parabolic meridian. Specially,

$$k=\frac{R_1^2-R_0^2}{L} \tag{4.4}$$

$$\varphi_0=\arctan\left(\frac{2R_0}{k}\right),\qquad \varphi_1=\arctan\left(\frac{2R_1}{k}\right). \tag{4.5}$$

For a hyperbolic shell of doubly curvature we can write

$$R_{\varphi}(\varphi)=\frac{-a^2b^2}{\sqrt{\left(a^2\sin^2\varphi-b^2\cos^2\varphi\right)^3}} \tag{4.6}$$

$$R_{\theta}(\varphi)=\frac{a^2}{\sqrt{a^2\sin^2\varphi-b^2\cos^2\varphi}}+\frac{R_S}{\sin\varphi}, \tag{4.7}$$

where
a, *b* are the length of the semi-transverse and semi-conjugate axes of the hyperbolic meridian, respectively. Specially,

$$b=\frac{aL}{\sqrt{R_0^2-a^2}-\sqrt{R_1^2-a^2}} \tag{4.8}$$

$$\varphi_0=\arctan\left[\frac{b(R_0-R_S)}{a\sqrt{(R_0-R_S)^2-a^2}}\right] \tag{4.9}$$

$$\varphi_0=\arctan\left[\frac{b(R_0-R_S)}{a\sqrt{(R_0-R_S)^2-a^2}}\right]. \tag{4.10}$$

In this paper, the structure motion equation of inversely coupled composite laminated shells is obtained using first-order shear deformation theory. Using this theory, the displacement of any point in the shell with index ζ is divided into the average surface and the cross-sectional rotation component

$$u_{\zeta}(\varphi,\theta,z,t)=u_{\zeta}^{0}(\varphi,\theta,t)+z\phi_{\varphi,\zeta}(\varphi,\theta,t)$$

$$\upsilon_{\zeta}(\varphi,\theta,z,t)=\upsilon_{\zeta}^{0}(\varphi,\theta,t)+z\phi_{\varphi,\zeta}(\varphi,\theta,t)$$

$$\omega_{\zeta}(\varphi,\theta,z,t)=\omega_{\zeta}^{0}(\varphi,\theta,t), \tag{4.11}$$

where
u_{ζ}^{0}, υ_{ζ}^{0}, ω_{ζ}^{0} are the displacements along the meridional, circumferential and radial direction at any point in middle surface of shell with index ζ;

$\varphi_{\phi\zeta}$ and $\varphi_{\theta\zeta}$ are the rotation ones along θ and ϕ direction.

Deformations at any point of the shell with index ζ can be determined through displacements and rotations of the middle surface as

$$\varepsilon_{\varphi,\zeta} = \varepsilon^0_{\varphi,\zeta} + z\chi_{\varphi,\zeta}, \quad \varepsilon_{\theta,\zeta} = \varepsilon^0_{\theta,\zeta} + z\chi_{\theta,\zeta}$$

$$\gamma_{\varphi\theta,\zeta} = \gamma^0_{\varphi\theta,\zeta} + z\chi_{\varphi\theta,\zeta}, \quad \gamma_{\varphi z,\zeta} = \gamma^0_{\varphi z,\zeta}, \quad \gamma_{\theta z,\zeta} = \gamma^0_{\varphi z,\zeta}, \qquad (4.12)$$

where

$\varepsilon_{\phi,\zeta}$, $\varepsilon_{\theta,\zeta}$ and $\gamma_{\phi\theta,\zeta}$ denote the normal and shear strains at any point of the shell with index ζ;

$\gamma_{\phi z,\zeta}$ and $\gamma_{\theta z,\zeta}$ denote transverse shear strains;

$\varepsilon_{\varphi,\zeta}{}^0$, $\varepsilon_{\theta,\zeta}{}^0$ and $\gamma_{\varphi\theta,\zeta}{}^0$ denote the meridional, circumferential and shear strains in the middle surface of the shell with index ζ;

$\chi_{\phi,\zeta}$, $\chi_{\theta,\zeta}$ and $\chi_{\phi\theta,\zeta}$ present the mid-plane curvature and mid-plane twist changes, respectively;

$\gamma_{\varphi z,\zeta}{}^0$ and $\gamma_{\theta z,\zeta}{}^0$ denote the transverse shear strains in the middle surface. the membrane strains of middle surface are defined as

$$\varepsilon^0_{\varphi,\zeta} = \frac{1}{A}\frac{\partial u^0_\zeta}{\partial \varphi_\zeta} + \frac{\upsilon^0_\zeta}{AB}\frac{\partial A}{\partial \theta_\zeta} + \frac{\omega^0_\zeta}{R_{\varphi,\zeta}}, \; \varepsilon^0_{\theta,\zeta} = \frac{1}{B}\frac{\partial \upsilon^0_\zeta}{\partial \theta_\zeta} + \frac{u^0_\zeta}{AB}\frac{\partial B}{\partial \varphi_\zeta} + \frac{\omega^0_\zeta}{R_{\theta,\zeta}}$$

$$\gamma^0_{\varphi\theta,\zeta} = \frac{A}{B}\frac{\partial}{\partial \theta_\zeta}\left(\frac{u^0_\zeta}{A}\right) + \frac{B}{A}\frac{\partial}{\partial \varphi_\zeta}\left(\frac{\upsilon^0_\zeta}{B}\right), \; \chi_{\varphi,\zeta} = \frac{1}{A}\frac{\partial \phi_{\varphi,\zeta}}{\partial \varphi_\zeta} + \frac{\phi_{\theta,\zeta}}{AB}\frac{\partial A}{\partial \theta_\zeta}$$

$$\chi_{\theta,\zeta} = \frac{1}{B}\frac{\partial \phi_{\theta,\zeta}}{\partial \theta_\zeta} + \frac{\phi_{\varphi,\zeta}}{AB}\frac{\partial B}{\partial \varphi_\zeta},$$

$$\chi_{\varphi\theta,\zeta} = \frac{A}{B}\frac{\partial}{\partial \theta_\zeta}\left(\frac{\psi_{\varphi,\zeta}}{A}\right) + \frac{B}{A}\frac{\partial}{\partial \varphi_\zeta}\left(\frac{\phi_{\theta,\zeta}}{B}\right)$$

$$\gamma^0_{\varphi z,\zeta} = \frac{1}{A}\frac{\partial \omega^0_\zeta}{\partial \varphi_\zeta} - \frac{u^0_\zeta}{R_{\varphi,\zeta}} + \phi_{\varphi,\zeta}, \; \gamma^0_{\theta z,\zeta} = \frac{1}{B}\frac{\partial \omega^0_\zeta}{\partial \theta_\zeta} - \frac{\upsilon^0_\zeta}{R_{\theta,\zeta}} + \phi_{\theta,\zeta}, \quad (4.13)$$

where A, B are the Lamé parameters.

The relationship between the resulting force components and the midsurface deformation components is expressed as follows

$$\begin{bmatrix} N_{\varphi,\zeta} \\ N_{\theta,\zeta} \\ N_{\varphi\theta,\zeta} \\ M_{\varphi,\zeta} \\ M_{\theta,\zeta} \\ M_{\varphi\theta,\zeta} \end{bmatrix} = \begin{bmatrix} A_{11} & A_{12} & A_{16} & B_{11} & B_{12} & B_{16} \\ A_{12} & A_{22} & A_{26} & B_{12} & B_{22} & B_{26} \\ A_{16} & A_{26} & A_{66} & B_{16} & B_{26} & B_{66} \\ B_{11} & B_{12} & B_{16} & D_{11} & D_{12} & D_{16} \\ B_{12} & B_{22} & B_{26} & D_{12} & D_{22} & D_{26} \\ B_{16} & B_{26} & B_{66} & D_{16} & D_{26} & D_{66} \end{bmatrix} \cdot \begin{bmatrix} \varepsilon^0_{\varphi,\zeta} \\ \varepsilon^0_{\theta,\zeta} \\ \gamma^0_{\varphi\theta,\zeta} \\ \chi^0_{\varphi,\zeta} \\ \chi^0_{\theta,\zeta} \\ \chi^0_{\varphi\theta,\zeta} \end{bmatrix}$$

$$\begin{bmatrix} Q_{\varphi,\zeta} \\ Q_{\theta,\zeta} \end{bmatrix} = \kappa \begin{bmatrix} A_{55} & A_{45} \\ A_{45} & A_{44} \end{bmatrix} \cdot \begin{bmatrix} \gamma^0_{\varphi z,\zeta} \\ \gamma^0_{\theta z,\zeta} \end{bmatrix}. \tag{4.14}$$

The relationship between force components and deformation components can be expressed through stiffness coefficients

$$A_{ij} = \sum_{k=1}^{N} \overline{Q}_{ij}^{k} \left(Z_{k+1} - Z_k \right)$$

$$B_{ij} = \frac{1}{2} \sum_{k=1}^{N} \overline{Q}_{ij}^{k} \left(Z_{k+1}^2 - Z_k^2 \right)$$

$$D_{ij} = \frac{1}{3} \sum_{k=1}^{N} \overline{Q}_{ij}^{k} \left(Z_{k+1}^3 - Z_k^3 \right), \; i, j = 1, \ldots, 6, \tag{4.15}$$

where $\overline{Q}_{ij}^{k}$ are the elastic coefficients.

Haar wavelet series are used to discretize derivatives in the governing equations of the entire system, including boundary and constraint conditions. A number of Haar wavelets are defined in the region [0, 1]. Therefore, linear transfer is necessary for the actual shell length region [0, L].

That is,

$$\xi = \frac{x}{L_x}. \tag{4.16}$$

The Haar wavelet series determines the higher order derivatives of the displacement components, and the lower order derivatives can be obtained by integrating this wavelet series. The higher order derivative of displacements in the basic equations of motion and expressions of boundary conditions is of second order. The derivative value can be obtained using the Haar wavelet series

$$\frac{d^2U_\zeta(\xi)}{d\xi^2} = \sum_{i=1}^{2M} a_i h_i(\xi), \quad \frac{d^2V_\zeta(\xi)}{d\xi^2} = \sum_{i=1}^{2M} b_i h_i(\xi),$$

$$\frac{d^2W_\zeta(\xi)}{d\xi^2} = \sum_{i=1}^{2M} c_i h_i(\xi), \quad \frac{d^2\Phi_\zeta(\xi)}{d\xi^2} = \sum_{i=1}^{2M} d_i h_i(\xi)$$

$$\frac{d^2\Theta_\zeta(\xi)}{d\xi^2} = \sum_{i=1}^{2M} e_i h_i(\xi), \tag{4.17}$$

where

a_i, b_i, c_i and d_i are unknown coefficients of the Haar wavelets.

The first-order derivatives of displacements and displacement functions for transformation type U are written as follows

$$\frac{dU_\zeta(\xi)}{d\xi} = \sum_{i=1}^{2M} a_i P_{1,i}(\xi) + \frac{dU_\zeta(0)}{d\xi}$$

$$U_\zeta(\xi) = \sum_{i=1}^{2M} a_i P_{2,i}(\xi) + \xi\frac{dU_\zeta(0)}{d\xi} + U_\zeta(0). \tag{4.18}$$

Similar relations can be written for such types of transformations as V, W, Φ and Θ.

Let us write matrix forms for U

$$\frac{d^2\mathbf{U}_\zeta}{d\xi^2} = \mathbf{H}_1\mathbf{a} + \mathbf{H}_{11}\mathbf{f},$$

$$\frac{d\mathbf{U}_{\zeta}}{d\xi} = \mathbf{P}_1\mathbf{a} + \mathbf{P}_{11}\mathbf{f}$$

$$\mathbf{U}_{\zeta} = \mathbf{P}_2\mathbf{a} + \mathbf{P}_{22}\mathbf{f}, \tag{4.19}$$

where **H**, $\mathbf{P_1}$ and $\mathbf{P_2}$ are the Haar wavelet and its integrals defined as

$$\mathbf{H}_1 = \begin{bmatrix} h_1(\xi_1) & h_2(\xi_1) & \cdots & h_n(\xi_1) \\ h_1(\xi_2) & h_2(\xi_2) & \cdots & h_n(\xi_2) \\ \vdots & \vdots & \ddots & \vdots \\ h_1(\xi_n) & h_2(\xi_n) & \cdots & h_n(\xi_n) \end{bmatrix} \tag{4.20}$$

$$\mathbf{H}_{11} = \begin{bmatrix} 0 & 0 \\ 0 & 0 \\ \vdots & \vdots \\ 0 & 0 \end{bmatrix} \tag{4.21}$$

$$\mathbf{P}_1 = \begin{bmatrix} P_{1,1}(\xi_1) & P_{1,2}(\xi_1) & \cdots & P_{1,n}(\xi_1) \\ P_{1,1}(\xi_2) & P_{1,2}(\xi_2) & \cdots & P_{1,n}(\xi_2) \\ \vdots & \vdots & \ddots & \vdots \\ P_{1,n}(\xi_n) & P_{1,n}(\xi_n) & \cdots & P_{1,n}(\xi_n) \end{bmatrix} \tag{4.22}$$

$$\mathbf{P}_{11} = \begin{bmatrix} 1 & 0 \\ 1 & 0 \\ \vdots & \vdots \\ 1 & 0 \end{bmatrix} \tag{4.23}$$

$$\mathbf{P}_2 = \begin{bmatrix} P_{2,1}(\xi_1) & P_{2,2}(\xi_1) & \cdots & P_{2,n}(\xi_1) \\ P_{2,1}(\xi_2) & P_{2,2}(\xi_2) & \cdots & P_{2,n}(\xi_2) \\ \vdots & \vdots & \ddots & \vdots \\ P_{2,1}(\xi_n) & P_{2,1}(\xi_n) & \cdots & P_{2,1}(\xi_n) \end{bmatrix} \tag{4.24}$$

$$\mathbf{P}_{22} = \begin{bmatrix} \xi_1 & 0 \\ \xi_2 & 0 \\ \vdots & \vdots \\ \xi_n & 0 \end{bmatrix} \tag{4.25}$$

The following notations are used in the above formulas

$$\mathbf{U}_\zeta = \left[U_\zeta(\xi_1), U_\zeta(\xi_2), \ldots, U_\zeta(\xi_n)\right]^T$$

$$\mathbf{a} = \left[a_1, a_2, \ldots, a_n\right]^T, \qquad \mathbf{f} = \left[\frac{dU_\zeta(\xi_0)}{d\xi}, U_\zeta(\xi_0)\right]^T$$

$$\mathbf{V}_\zeta = \left[V_\zeta(\xi_1), V_\zeta(\xi_2), \ldots, V_\zeta(\xi_n)\right]^T$$

$$\mathbf{b} = \left[b_1, b_2, \ldots, b_n\right]^T, \qquad \mathbf{g} = \left[\frac{dV_\zeta(\xi_0)}{d\xi}, V_\zeta(\xi_0)\right]^T$$

$$\mathbf{W}_\zeta = \left[W_\zeta(\xi_1), W_\zeta(\xi_2), \ldots, W_\zeta(\xi_n)\right]^T$$

$$\mathbf{c} = \left[c_1, c_2, \ldots, c_n\right]^T, \qquad \mathbf{h} = \left[\frac{dW_\zeta(\xi_0)}{d\xi}, W_\zeta(\xi_0)\right]^T$$

$$\mathbf{\Phi}_\zeta = \left[\Phi_\zeta(\xi_1), \Phi_\zeta(\xi_2), \ldots, \Phi_\zeta(\xi_n)\right]^T$$

$$\mathbf{d} = \left[d_1, d_2, \ldots, d_n\right]^T, \quad \mathbf{k} = \left[\frac{d\Phi_\zeta(\xi_0)}{d\xi}, \Phi_\zeta(\xi_0)\right]^T$$

$$\mathbf{\Theta}_\zeta = \left[\Theta_\zeta(\xi_1), \Theta_\zeta(\xi_2), \ldots, \Theta_\zeta(\xi_n)\right]^T$$

$$\mathbf{e} = \left[e_1, e_2, \ldots, e_n\right]^T, \quad \mathbf{l} = \left[\frac{d\Theta_\zeta(\xi_0)}{d\xi}, \Theta_\zeta(\xi_0)\right]^T, \text{(4.26)}$$

where
f, **g**, **h**, **k** and ***l*** indicate the integral constants, which can be obtained by applying the boundary condition.

The first order is the highest order of the displacements of the boundary condition equations, and the derivatives and first-order displacements in equation (4.18) are calculated at $\xi = 0$ and $\xi = 1$.

The discretization of the boundary conditions equation can be written in matrix form as follows

$$\frac{d\,\mathbf{U_b}}{d\xi} = \mathbf{P_{b1}a} + \mathbf{P_{b11}f}, \quad \frac{d\,\mathbf{V_b}}{d\xi} = \mathbf{P_{b1}b} + \mathbf{P_{b11}g}$$

$$\frac{d\,\mathbf{W_b}}{d\xi} = \mathbf{P_{b1}c} + \mathbf{P_{b11}h}, \quad \frac{d\,\mathbf{\Phi_b}}{d\xi} = \mathbf{P_{b1}d} + \mathbf{P_{b11}k}$$

$$\frac{d\,\mathbf{\Theta_b}}{d\xi} = \mathbf{P_{b1}e} + \mathbf{P_{b11}}\,\boldsymbol{l} \quad \text{(4.27)}$$

$$\mathbf{U_b} = \mathbf{P_{b2}a} + \mathbf{P_{b22}f}, \quad \mathbf{V_b} = \mathbf{P_{b2}b} + \mathbf{P_{b22}g}$$

$$\mathbf{W_b} = \mathbf{P_{b2}c} + \mathbf{P_{b22}h}, \quad \mathbf{\Phi_b} = \mathbf{P_{b2}d} + \mathbf{P_{b22}k}$$

$$\mathbf{\Theta_b} = \mathbf{P_{b2}e} + \mathbf{P_{b22}}\,\boldsymbol{l}, \quad \text{(4.28)}$$

where notations are defined as follows

$$\mathbf{P_{b11}} = \begin{bmatrix} p_{1,1}(0) & p_{1,2}(0) & \cdots & p_{1,n}(0) \\ p_{1,1}(1) & p_{1,2}(1) & \cdots & p_{1,n}(1) \end{bmatrix},\ \mathbf{P_{b1}} = \begin{bmatrix} 1 & 1 \\ 1 & 1 \end{bmatrix} \quad (4.29)$$

$$\mathbf{P_{b22}} = \begin{bmatrix} p_{2,1}(0) & p_{2,2}(0) & \cdots & p_{2,n}(0) \\ p_{2,1}(1) & p_{2,2}(1) & \cdots & p_{2,n}(1) \end{bmatrix},\ \mathbf{P_{b2}} = \begin{bmatrix} \xi_0 & 1 \\ \xi_1 & 1 \end{bmatrix} \quad (4.30)$$

The continuity equations can be expressed similarly to the equations for boundary conditions

$$\frac{d\,\mathbf{U_c}}{d\xi} = \mathbf{P_{c1}a} + \mathbf{P_{c11}f}, \quad \frac{d\,\mathbf{V_c}}{d\xi} = \mathbf{P_{c1}b} + \mathbf{P_{c11}g}$$

$$\frac{d\,\mathbf{W_c}}{d\xi} = \mathbf{P_{c1}c} + \mathbf{P_{c11}h}, \quad \frac{d\,\mathbf{\Phi_c}}{d\xi} = \mathbf{P_{c1}d} + \mathbf{P_{c11}k}$$

$$\frac{d\,\mathbf{\Theta_c}}{d\xi} = \mathbf{P_{c1}e} + \mathbf{P_{c11}}\,\mathbf{I} \quad (4.31)$$

$$\mathbf{U_c} = \mathbf{P_{c2}a} + \mathbf{P_{c22}f}, \quad \mathbf{V_c} = \mathbf{P_{c2}b} + \mathbf{P_{c22}g}$$

$$\mathbf{W_c} = \mathbf{P_{c2}c} + \mathbf{P_{c22}h}, \quad \mathbf{\Phi_c} = \mathbf{P_{c2}d} + \mathbf{P_{c22}k}$$

$$\mathbf{\Theta_c} = \mathbf{P_{c2}e} + \mathbf{P_{c22}}\,\mathbf{I}, \quad (4.32)$$

where notations are defined as follows

$$\mathbf{P_{c11}} = \begin{bmatrix} p^c_{1,1}(0) & p^c_{1,2}(0) & \cdots & p^c_{1,n}(0) \\ p^c_{1,1}(1) & p^c_{1,2}(1) & \cdots & p^c_{1,n}(1) \end{bmatrix},\ \mathbf{P_{c1}} = \begin{bmatrix} 1 & 1 \\ 1 & 1 \end{bmatrix} \quad (4.33)$$

$$\mathbf{P_{c22}} = \begin{bmatrix} p^c_{2,1}(0) & p^c_{2,2}(0) & \cdots & p^c_{2,n}(0) \\ p^c_{2,1}(1) & p^c_{2,2}(1) & \cdots & p^c_{2,n}(1) \end{bmatrix},\ \mathbf{P_{c2}} = \begin{bmatrix} \xi_0 & 1 \\ \xi_1 & 1 \end{bmatrix} \quad (4.34)$$

Thus, the equations of motion of entire systems of inversely coupled composite laminated shells, including boundary conditions, are discretized using Haar wavelet transforms and can be expressed in matrix form as

$$\begin{bmatrix} \mathbf{K}_{db} & \mathbf{K}_{dd} \\ \mathbf{K}_{bb} & \mathbf{K}_{bd} \end{bmatrix} \cdot \begin{bmatrix} \mathbf{A}_d \\ \mathbf{A}_b \end{bmatrix} - \omega^2 \begin{bmatrix} \mathbf{M}_{db} & \mathbf{M}_{dd} \\ 0 & 0 \end{bmatrix} \cdot \begin{bmatrix} \mathbf{A}_d \\ \mathbf{A}_b \end{bmatrix} = 0$$

$$\mathbf{A}_d = [\mathbf{a}, \mathbf{b}, \mathbf{c}, \mathbf{d}, \mathbf{e}]^T, \quad \mathbf{A}_b = [\mathbf{f}, \mathbf{g}, \mathbf{h}, \mathbf{k}, \mathbf{l}]^T, \tag{4.35}$$

where

b, *d* are subscripts that indicate the discrete equilibrium equations of motion and the boundary conditions.

Numerical evaluations suggested that certain parameters, such as geometric size, direction of reinforced inclusions, and composite material properties, influence the free vibration of back-bonded composite laminated shells. First, a convergence study is conducted to test the robustness of the proposed method. Then, several parameters such as geometric size, fiber direction and material properties are investigated at the natural frequency of the inversely bonded composite laminated shells.

A comparison of the results obtained in this work (A) with the results of the finite element method (B) is presented in the following tables for boundary conditions of the type: C-C, C-F, S-S and C-S.

Table 5. Spectral distribution for a connected composite layered spherical-cylindrical shell

	C-C		C-F		S-S		C-S	
f, Hz	A	B	A	B	A	B	A	B
1	332.58	332.06	66.67	66.20	314.58	314.58	316.15	315.83
2	364.77	366.14	97.02	97.13	320.62	321.05	349.82	350.50
3	378.72	380.01	124.97	124.85	346.62	347.17	361.36	362.21
4	455.70	454.72	126.26	126.16	442.53	441.44	447.22	446.18
5	449.04	494.92	208.83	208.89	478.98	479.15	488.06	488.88
6	506.88	507.94	217.50	217.48	479.55	480.22	494.64	495.24
7	555.62	555.84	302.51	303.13	555.62	555.43	555.62	555.63
8	643.65	643.94	317.45	317.23	635.77	635.82	638.70	638.83
9	676.34	678.14	320.77	322.85	660.25	661.23	669323	670.54
10	700.09	701.91	342.36	342.18	700.09	701.27	700.09	701.59

Table 6. Spectral distribution for a coupled composite layered elliptical-cylindrical shell

	C-C		C-F		S-S		C-S	
f, Hz	A	B	A	B	A	B	A	B
1	207.64	207.85	36.85	35.47	199.78	199.22	203.41	203.58
2	210.17	210.35	60.92	60.98	199.48	199.21	204.19	204.79
3	259.11	259.78	80.71	80.97	253.51	253.22	256.98	256.34
4	314.11	313.25	83.88	83.77	304.82	304.33	306.31	306.15
5	314.90	315.26	150.52	150.33	308.25	307.44	314.40	314.05
6	321.16	321.49	151.40	151.45	313.13	313.88	317.27	317.19
7	323.84	323.99	202.44	202.30	323.90	323.80	323.78	323.65
8	404.74	405.42	232.89	233.32	386.74	387.06	388.13	388.48
9	404.81	405.22	274.48	274.11	389.75	389.94	404.14	405.08
10	406.22	406.57	313.51	313.54	404.87	405.19	405.57	406.08

Table 7. Spectral distribution for a coupled composite layered parabolic-cylindrical shell

	C-C		C-F		S-S		C-S	
f, Hz	A	B	A	B	A	B	A	B
1	356.59	356.98	30.46	29.80	337.31	337.50	337.97	338.10
2	402.98	401.13	38.92	37.80	365.94	364.84	402.78	401.67
3	404.01	403.51	55.63	55.59	384.65	383.93	404.07	403.50
4	471.44	469.50	126.38	126.41	459.09	456.58	460.51	458.26
5	531.66	532.84	168.21	169.13	467.08	467.81	531.66	532.81
6	583.64	584.07	204.55	206.81	535.31	536.89	583.64	583.15
7	617.61	620.10	208.83	209.34	583.64	583.12	617.61	620.87
8	643.28	644.63	301.98	303.96	618.35	620.44	643.87	644.05
9	709.26	712.18	403.97	402.15	643.15	644.28	709.25	712.67
10	753.90	754.24	405.31	404.29	707.80	710.19	716.12	719.88

For ease of calculation, it is assumed that the individual shells are made from the same laminated composite material and have the same thickness. The following properties of laminated composites were used for calculations: E_1 = 150 GPa, E_2 = 10 GPa, μ = 0.25, $G_{12} = G_{13} = G_{23}$ = 5 GPa, ρ = 1500 kg/m^3, α_f = [0^0/90^0].

Table 8. Spectral distribution for a coupled composite layered hyperbolic-cylindrical shell

	C-C		C-F		S-S		C-S	
f, Hz	A	B	A	B	A	B	A	B
1	223.54	223.69	16.48	16.08	216.13	216.20	217.34	217.42
2	323.36	321.74	27.93	22.48	313.33	311.88	313.54	312.08
3	332.45	332.58	33.38	32.59	332.78	332.49	332.37	332.28
4	375.23	374.89	83.71	83.24	356.45	356.20	371.19	371.67
5	388.62	389.01	150.51	150.93	364.95	365.06	374.47	373.12
6	394.65	395.18	166.79	167.53	371.19	371.67	388.62	389.01
7	431.35	432.33	195.37	196.08	403.36	404.13	403.38	404.15
8	471.47	472.68	232.53	234.15	449.36	449.59	449.83	450.05
9	483.47	485.39	329.74	335.39	453.27	454.81	453.21	454.83
10	526.25	526.67	353.54	355.39	511.92	512.78	511.93	513.37

In all numerical results *m* denotes the meridional wavenumber and *n* denotes the circular wavenumber. In addition, for convenience of expression, the dimensionless frequency is introduced ($\Omega = \omega R_C(\rho/E_2)^{1/2}$.

The following tables show the results of numerical calculations of the dimensionless frequencies of some inversely coupled composite layered shells.

Table 9. Dimensionless frequencies for a three-layer elliptical-cylindrical shell: 0^0- 90^0 - 0^0

		Boundary conditions									
m	n	C-C	C-F	C-S	S-S	S-F	E1-C	E2-C	E3-C	E1-E1	E2-E2
1	1	0.263	0.082	0.257	0.252	0.081	0.169	0.259	0.169	0.113	0.255
	2	0.428	0.190	0.422	0.416	0.187	0.249	0.425	0.246	0.239	0.421
	3	0.761	0.440	0.745	0.736	0.431	0.433	0.744	0.434	0.262	0.737
	4	0.806	0.616	0.795	0.778	0.616	0.585	0.790	0.587	0.386	0.766
	5	0.109	0.808	1.072	1.057	0.781	0.807	0.998	0.807	0.574	0.969
2	1	0.265	0.045	0.257	0.250	0.045	0.256	0.260	0.257	0.245	0.257
	2	0.410	0.257	0.402	0.393	0.248	0.283	0.406	0.276	0.281	0.403
	3	0.649	0.442	0.609	0.607	0.435	0.437	0.601	0.439	0.285	0.599
	4	0.651	0.627	0.650	0.611	0.593	0.622	0.650	0.622	0.457	0.603
	5	0.985	0.725	0.939	0.933	0.724	0.733	0.843	0.737	0.651	0.833
3	1	0.387	0.102	0.379	0.373	0.102	0.234	0.385	0.221	0.234	0.382
	2	0.450	0.396	0.442	0.431	0.385	0.397	0.447	0.398	0.234	0.443
	3	0.616	0.460	0.577	0.575	0.454	0.461	0.557	0.463	0.411	0.554
	4	0.631	0.619	0.624	0.579	0.574	0.620	0.624	0.620	0.466	0.562
	5	0.949	0.674	0.898	0.888	0.673	0.706	0.790	0.712	0.692	0.785

Table 10. Dimensionless frequencies for a four-layer parabolic-cylindrical shell: 30^0: (-30^0): 30^0: (-30^0)

		Boundary conditions									
m	n	C-C	C-F	C-S	S-S	S-F	E1-C	E2-C	E3-C	E1-E1	E2-E2
1	1	0.518	0.095	0.505	0.489	0.094	0.272	0.420	0.049	0.162	0.391
	2	0.718	0.453	0.683	0.679	0.435	0.322	0.603	0.211	0.234	0.510
	3	0.821	0.587	0.807	0.787	0.587	0.658	0.723	0.278	0.291	0.615
	4	0.930	0.710	0.895	0.886	0.711	0.715	0.831	0.587	0.538	0.746
	5	1.052	0.785	1.050	0.963	0.777	0.853	0.930	0.659	0.650	0.855
2	1	0.431	0.063	0.427	0.408	0.063	0.266	0.376	0.062	0.256	0.370
	2	0.720	0.428	0.699	0.691	0.408	0.351	0.647	0.254	0.267	0.605
	3	0.861	0.683	0.841	0.829	0.678	0.725	0.749	0.343	0.340	0.675
	4	0.988	0.828	0.944	0.940	0.817	0.831	0.871	0.687	0.701	0.771
	5	1.126	0.990	1.126	1.029	0.984	0.963	0.988	0.814	0.817	0.881
3	1	0.609	0.130	0.594	0.594	0.130	0.104	0.594	0.129	0.089	0.574
	2	0.702	0.633	0.700	0.665	0.630	0.609	0.614	0.158	0.104	0.597
	3	0.895	0.706	0.874	0.868	0.672	0.773	0.845	0.633	0.646	0.793
	4	1.103	0.880	1.055	1.052	0.876	0.905	0.930	0.783	0.783	0.875
	5	1.216	1.122	1.215	1.131	1.102	1.102	1.106	0.891	0.924	0.951

Table 11. Dimensionless frequencies for a four-layer parabolic-cylindrical shell: 15^0: (-30^0): 15^0: (-30^0)

		Boundary conditions									
m	n	C-C	C-F	C-S	S-S	S-F	E1-C	E2-C	E3-C	E1-E1	E2-E2
1	1	0.641	0.182	0.614	0.595	0.181	0.258	0.482	0.253	0.234	0.454
	2	0.796	0.489	0.772	0.740	0.474	0.475	0.696	0.475	0.257	0.521
	3	1.114	0.677	1.043	1.029	0.677	0.725	0.827	0.739	0.311	0.757
	4	1.198	0.860	1.164	1.076	0.809	0.853	1.147	0.853	0.680	0.840
	5	1.641	0.948	1.604	1.596	0.947	0.936	1.329	0.937	0.759	1.281
2	1	0.534	0.105	0.509	0.488	0.104	0.273	0.449	0.263	0.274	0.405
	2	0.723	0.469	0.708	0.683	0.442	0.472	0.658	0.473	0.281	0.566
	3	1.142	0.712	1.055	1.044	0.701	0.765	0.788	0.772	0.338	0.757
	4	1.192	1.019	1.170	1.074	0.979	1.069	1.165	1.075	0.778	0.801
	5	1.705	1.155	1.640	1.639	1.089	1.191	1.338	1.197	0.975	1.317
3	1	0.633	0.142	0.598	0.585	0.142	0.097	0.538	0.036	0.083	0.520
	2	0.675	0.640	0.662	0.629	0.597	0.642	0.658	0.643	0.111	0.564
	3	1.182	0.703	1.097	1.084	0.699	0.760	0.841	0.768	0.708	0.837
	4	1.219	1.193	1.203	1.115	1.095	1.196	1.200	1.196	0.784	0.846
	5	1.815	1.196	1.728	1.718	1.193	1.347	1.402	1.367	1.314	1.383

Table 12. Dimensionless frequencies for a three-layer hyperbolic-cylindrical shell: 45^0: (-45^0): 45^0

		Boundary conditions									
m	n	C-C	C-F	C-S	S-S	S-F	E1-C	E2-C	E3-C	E1-E1	E2-E2
1	1	0.507	0.078	0.495	0.475	0.075	0.276	0.429	0.274	0.107	0.393
	2	0.839	0.384	0.812	0.808	0.366	0.280	0.725	0.280	0.239	0.653
	3	0.926	0.722	0.903	0.897	0.721	0.695	0.844	0.702	0.288	0.743
	4	0.967	0.795	0.967	0.917	0.794	0.782	0.927	0.782	0.668	0.856
	5	1.093	0.858	1.079	1.074	0.850	0.913	1.046	0.914	0.684	0.986
2	1	0.460	0.073	0.457	0.453	0.073	0.297	0.453	0.287	0.259	0.445
	2	0.663	0.452	0.646	0.641	0.448	0.452	0.649	0.453	0.297	0.597
	3	1.052	0.637	1.026	1.024	0.632	0.643	0.951	0.643	0.441	0.882
	4	1.100	0.914	1.083	1.078	0.913	0.953	1.061	0.959	0.606	0.957
	5	1.211	1.074	1.193	1.160	1.071	1.044	1.105	1.048	0.914	1.066
3	1	0.531	0.166	0.515	0.515	0.166	0.081	0.529	0.150	0.081	0.489
	2	0.844	0.541	0.840	0.827	0.541	0.531	0.812	0.531	0.094	0.799
	3	0.994	0.846	0.981	0.981	0.833	0.846	0.994	0.849	0.542	0.944
	4	1.207	0.993	1.186	1.179	0.993	0.992	1.165	0.992	0.850	1.093
	5	1.343	1.181	1.324	1.308	1.174	1.212	1.282	1.213	1.009	1.194

Table 13. Dimensionless frequencies for a four-layer parabolic-cylindrical shell: 30^0 - 60^0 - 30^0 - 60^0

		Boundary conditions									
m	n	C-C	C-F	C-S	S-S	S-F	E1-C	E2-C	E3-C	E1-E1	E2-E2
1	1	0.787	0.180	0.782	0.768	0.178	0.241	0.726	0.239	0.241	0.703
	2	1.200	0.536	1.177	1.176	0.527	0.513	1.042	0.513	0.281	1.004
	3	1.266	1.043	1.253	1.209	1.043	1.037	1.206	1.043	0.307	1.067
	4	1.431	1.206	1.375	1.361	1.200	1.163	1.3368	1.163	1.006	1.219
	5	1.570	1.265	1.564	1.545	1.216	1.351	1.456	1.353	1.099	1.391
2	1	0.614	0.114	0.610	0.603	0.114	0.299	0.595	0.291	0.279	0.579
	2	0.865	0.536	0.852	0.849	0.529	0.575	0.860	0.576	0.302	0.831
	3	1.314	0.881	1.255	1.255	0.877	0.873	1.254	0.873	0.491	1.112
	4	1.461	1.246	1.461	1.415	1.246	1.266	1.328	1.271	0.904	1.259
	5	1.596	1.460	1.570	1.545	1.414	1.362	1.468	1.365	1.282	1.400
3	1	0.733	0.207	0.716	0.715	0.202	0.041	0.731	0.114	0.041	0.689
	2	0.854	0.754	0.849	0.841	0.752	0.738	0.845	0.738	0.138	0.834
	3	1.290	0.862	1.235	1.235	0.855	0.891	1.290	0.893	0.782	1.131
	4	1.454	1.336	1.454	1.412	1.336	1.291	1.418	1.290	0.903	1.417
	5	1.829	1.454	1.742	1.745	1.421	1.507	1.540	1.515	1.434	1.471

Table 14. Dimensionless frequencies for a four-layer parabolic-cylindrical shell: 15^0 - 75^0 - 15^0 - 75^0

		Boundary conditions									
m	n	C-C	C-F	C-S	S-S	S-F	E1-C	E2-C	E3-C	E1-E1	E2-E2
1	1	0.645	0.167	0.629	0.629	0.166	0.166	0.626	0.252	0.229	0.607
	2	0.963	0.405	0.953	0.953	0.402	0.402	0.963	0.379	0.247	0.962
	3	1.262	0.931	1.219	1.219	0.918	0.918	1.140	0.922	0.300	1.103
	4	1.461	1.099	1.392	1.392	1.098	1.098	1.349	1.090	0.734	1.205
	5	1.672	1.327	1.671	1.671	1.259	1.259	1.556	1.342	1.114	1.478
2	1	0.544	0.092	0.525	0.525	0.091	0.091	0.530	0.305	0.312	0.516
	2	0.699	0.501	0.691	0.691	0.490	0.490	0.699	0.501	0.315	0.698
	3	1.217	0.735	1.171	1.171	0.732	0.732	1.181	0.735	0.439	0.171
	4	1.387	1.192	1.313	1.313	1.190	1.190	1.284	1.187	0.768	1.217
	5	1.507	1.245	1.555	1.555	1.209	1.209	1.425	1.261	1.139	1.357
3	1	0.689	0.202	0.683	0.683	0.202	0.202	0.689	0.113	0.152	0.689
	2	0.727	0.698	0.714	0.714	0.692	0.692	0.725	0.699	0.152	0.742
	3	1.224	0.750	1.174	1.174	0.746	0.746	1.215	0.761	0.726	1.210
	4	1.357	1.229	1.281	1.281	1.197	1.197	1.309	1.253	0.775	1.279
	5	1.657	1.355	1.566	1.566	1.323	1.323	1.430	1.399	1.295	1.384

The calculation results show the possibility of studying the behavior of free vibrations of inversely coupled composite laminated shells under generalized boundary conditions. Two lenticular shells were back-connected at both ends of the cylindrical shell. Individual shells were connected by a continuous condition, and the boundary and continuous conditions were generalized by the artificial spring method.

The displacement field at an arbitrary point of the connected shell was determined using the theory of first-order shear deformation, and the displacement function was expanded by Haar wavelet series in the meridional direction and trigonometric series in the circumferential direction. A boundary condition was added to the control function of the main system to satisfy the Haar wavelet integral constant.

The accuracy and reliability of the proposed method were verified through convergence studies and precision testing. The influence of certain parameters on the free vibration behavior of inversely coupled composite shells was then investigated. Based on the study of parameters, the following conclusions can be drawn.

The critical value of the stiffness of the composite laminated shell material has been determined. This value can be considered as a free boundary condition. The excess of the stiffness over the critical value corresponds to a fully clamped boundary condition. In addition, if the stiffness value of the laminated composite

material is less than the critical value, then this state can be considered as an elastic boundary condition.

As the length of the cylindrical shell in the middle part increases, regardless of the coupling design and boundary conditions, it initially increases slightly, but when the length exceeds a certain value, the frequency decreases quickly.

The frequency of the coupled shell structure changed symmetrically along the 90° fiber direction as the fiber direction changed from 0° to 180°.

As the number of layers increased, the frequency increased or decreased depending on the boundary conditions.

All fundamental frequencies were in the region in which the circumferential wave number was $0 \leq n \leq 4$.

Relative changes $\varepsilon' = f_{max}/f_{min}$ of dimensionless frequencies of four-layer and three-layer shells for all types of boundary conditions from C – C and to E2 – E2 corresponded to the following characteristic numerical intervals (A: 15^0-75^0-15^0-75^0 and B: 45^0-(–45^0)-45^0):

A) $\varepsilon' \in (2.3 \div 2.6)$, $m = 1$; $\varepsilon' \in (2.6 \div 2.7)$, $m = 2$; $\varepsilon' \in (2.0 \div 2.4)$, $m = 3$

B) $\varepsilon' \in (2.1 \div 2.5)$, $m = 1$; $\varepsilon' \in (2.4 \div 2.6)$, $m = 2$; $\varepsilon' \in (2.4 \div 2.5)$, $m = 3$.

CHAPTER 5
WAVELET TRANSFORMS

In numerous works [123 – 187] devoted to the continuous wavelet transform, the potential field was introduced and widely used as an effective tool for estimating the source parameters of homogeneous fields: the depth to the source z_0 and the structural index N. It is often defined as the rate of decay of the field with distance from the source. It can be argued that methods using continuous wavelet transform belong to the class of multiscale methods for estimating source parameters. The construction of a wavelet basis for operator equations was carried out in the work of Dahmen.

Assuming a two-dimensional function $f(x, y) \in L^2(\boldsymbol{R}^2)$ and an analyzing wavelet $\psi(x, y) \in L^2(\boldsymbol{R}^2)$, its continuous wavelet transform Wf with L^1 norm is defined as

$$Wf\left(b,a,\theta\right)=\frac{1}{a^2}\int R^2\, f\left(\mathrm{r}\right)\overline{\psi}\left[\frac{r_{-\theta}\left(\mathrm{r}-b\right)}{a}\right]dr\,, \tag{5.1}$$

where
$r\,(x, y)$ is the position vector;
$a \in \boldsymbol{R}^+$ is the scale or dilation of the wavelet ψ;
$\overline{\psi}$ is its complex conjugate;
$r_{-\theta}$ the rotation of the wavelet with respect to the angle θ;
$b \in \boldsymbol{R}^2$ is the position of the wavelet.

Equation (5.1) means that for any extension, a continuous wavelet transform can be expressed as a convolution of the field by any admissible wavelet y. In fact, we can write equation (5.1) as

$$Wf\left(b,a,\theta\right)=\ f\ *\psi\,, \tag{5.2}$$

where symbol "*" denotes convolution.

Thanks to the properties of the convolution integral, we can write for any wavelet $\psi_x^k = \partial^k\phi/\partial x^k$

$$W_{x,a}^{k}\,f\ =a^k\ \frac{\partial^k}{\partial x^k}\left(f\ *\phi\right), \tag{5.3}$$

where
ϕ is the so-called smoothing function;
k is the derivation order;

a is the scale or dilatation.

Therefore, in the Fourier domain we can write

$$\widehat{W}_{x,a}^{k} f = \hat{f}\hat{\psi}_{a}^{k}, \tag{5.4}$$

where

$\widehat{W}_{x,a}^{k} f$, $\hat{f}$ and $\hat{\psi}_{a}^{k}$ are the Fourier transforms of *f*, $W_{x,a}^{k}$ and $\hat{\psi}_{a}^{k}$, respectively.

Similar relationships are obtained when choosing wavelets such as

$$\psi_{y}^{k} = \frac{\partial^{k}\phi}{\partial y^{k}} \text{ or } \psi_{x,z}^{k} = \frac{\partial^{k}\phi}{\partial x \partial z^{k-1}} \text{ or } \psi_{y,z}^{k} = \frac{\partial^{k}\phi}{\partial y \partial z^{k-1}}. \tag{5.5}$$

The continuous wavelet transform of potential fields has a special property when wavelets constructed on the kernel of the Poisson semigroup are used. In fact, *Wf* is mathematically equivalent to the well-known upward continuation of the k^{th} order horizontal derivative of *f*, except for the scale factor. In order to continue considering the analogy, let us write down a mathematical expression for the following wavelet

$$\psi_{x}^{k}(r) = \frac{\partial^{k} p}{\partial x^{k}}, \tag{5.6}$$

where p is the smoothing function for the Poisson kernel

$$p(r) = \frac{1}{2\pi} \frac{1}{\left(1 + x^{2} + y^{2}\right)^{3/2}}, \tag{5.7}$$

where for the Fourier transform we can write

$$\hat{P}(\rho) = \exp(-\alpha \rho), \tag{5.8}$$

where

$\hat{P}$ is the Fourier transform of *p*;

$\rho = (\alpha^{2} + \beta^{2})^{1/2}$;

α and β are the wave numbers in the frequency domain.

The wavelet transform *f* with respect to $\psi_{x,a}^{k}$ can be written in the following form

$$w_{x,a}^{k} f = f * \psi_{x,a}^{k} = f * \left(a^{k} \frac{\partial^{k} p_{a}}{\partial x^{k}} \right) =$$

$$= a^{k} \frac{\partial^{k}}{\partial x^{k}} \left(f * p_{a} \right) = a^{k} \frac{\partial^{k}}{\partial x^{k}} f(r,a). \qquad (5.9)$$

Formula (5.9) allows us to conclude that the value $W_{x,a}^{k} f$ can be considered as the k^{th} derivative with respect to *x* of *f*, which is calculated for parameters from z_1 to *z*, with the exception of the scale factor a^k, where z_1 is the measurement level for the field *f*, and *z* is the fixed trend parameter. For a simple ideal source such as a pole, and assuming the *z*-axis is positive downward from $z_1 = 0$, we can accordingly say that a field f, singular at z_0, will have an extension $a = |z - z_0|$ at any level *z*.

Likewise

$$W_{y,a}^{k} = a^{k} \frac{\partial^{k}}{\partial y^{k}} f(r,a). \qquad (5.10)$$

Continuous wavelet transform analysis allows the detection and characterization of features contained in a signal. The wavelet transform is analyzed using the so-called maximum lines of the wavelet transform modulus. These lines are formed by connecting the maxima of the absolute values of the continuous wavelet transform at several scales.

In the case of a potential field, the singularities correspond to the positions of the source: in fact, the field at the source level is singular and its derivatives are not defined. In this case, we can say that the singularities of the potential field are located far from the measurement plane. So, in order to obtain the initial parameters of a homogeneous potential field from their continuous wavelet transformations, it is necessary to compare the value of $\log(W_{x,a}^{k} f / a^{k})$ not just in comparison with $\log(a)$, but in comparison with the scaled value $\log(a + z^{\wedge}_0)$, where $z^{\wedge}_0$ is the estimated source depth. For general extended sources, the lines of maxima of the modulus of the wavelet transform intersect each other at the boundary of the body under study for the case when a sufficiently high order is chosen *k*.

Since the field is measured at some distance from the source, it can be assumed that it is highly non-singular on the measurement scale. Let's assume that in the Cartesian coordinate system the z-axis has a positive downward direction.

Next, we can place the origin of coordinates in the measuring surface, so that z_1 = 0. Let us now consider the force field $f(x, y, z_1)$, created by a bipolar source at point Q (x_0, y_0, z_0).

The field $f(x, y, z_1)$ under study can be considered as a field f_Q, singular at point Q, extended to the interval $a_1 = |z_1 - z_0|$

$$f_1 = f(x, y, z_1) f_{Q^* P a_1}. \tag{5.11}$$

Poisson wavelet can be represented in the following form

$$\psi_{p,x}^{k}(r) = \frac{\partial^k p}{\partial x^k}. \tag{5.12}$$

Then for any extension $a > a_1$ we can write

$$W_{x,a}^{k,\{p\}} f = a^k \frac{\partial^k}{\partial x^k}\left(f_1 * p_{a-a_1}\right) = a^k \frac{\partial^k}{\partial x^k}\left(f_Q * p_{a_1} * p_{a-a_1}\right) =$$

$$= a^k \frac{\partial^k}{x^k}\left(f_Q * p_a\right). \tag{5.13}$$

Equation (5.13) shows that $W_{x,a}{}^k f$, obtained at a-scale a using Poisson wavelets does not depend on whether it is calculated in steps, for example, using a single convolution step allocated to two scales a_0 and a, or multiple convolution , relating first to the scales $\{a_0, a_1\}$, and then to the scales $\{a_1, a\}$, where $a > a_1$.

Let us now consider some other form of admissible wavelet

$$\psi_x^k(r) = \frac{\partial u}{\partial x^k}, \tag{5.14}$$

where
u is the corresponding smoothing function.

Wavelets built on the smoothing function u allow one to analyze the measured field for a continuous wavelet transform

$$W_{x,a}^{k,\{u,p\}} f = a^k \frac{\partial^k}{\partial x^k}\left(f_1 * u_{a-a_1}\right) = a^k \frac{\partial^k}{\partial x^k}\left(f_Q * p_{a_1} * u_{a-a_1}\right). \tag{5.15}$$

It can be argued that this time the continuous wavelet transform includes more types of wavelets and can only be defined as a multiple convolution, this time associated with wavelet mixing, namely a Poisson wavelet for the expansion from a_0 to a_1 and any wavelet u for extensions from a_1 to a.

In order to remove the restriction in choosing wavelets other than those belonging to the Poisson kernel, a new method can be proposed called the composite continuous wavelet transform, which consists of changing the definition of $W_{x,a}{}^k f(u)$ by introducing a composite wavelet operator

$$\nu_{a_1} = p_{a_1}^{-1} * u_{a_1}. \tag{5.16}$$

This operator is the convolution between the inverse Poisson smoothing function (for example, the continuation-down operator $P^{\wedge}(r) = e^{a\rho}$) and any scaling function u. Applying this transformation to the potential field on the measurement plane, on a scale a_1, we can replace the measured field $f(p, a_1) = f_Q * p_{a1}$ with the corresponding function $f(u, a_1) = f_Q * u_{a1}$, obtained on the same scale by dilation with wavelet other than the Poisson wavelet.

Now we can write the following relation for any scale $a > a_1$

$$W_{x,a}^{k,\{u,p\}} f = a^k \frac{\partial^k}{\partial x^k}\left(f * \nu_{a_1} * u_{a-a_1}\right) =$$

$$= a^k \frac{\partial^k}{\partial x^k}\left(f_Q * p_{a_1} * p_{a_1}^{-1} * u_{a_1} * u_{a-a_1}\right) = a^k \frac{\partial^k}{\partial x^k}\left(f_Q * u_a\right). \tag{5.17}$$

Equation (5.17) is similar to equation (5.13). However, the entire field can now be treated as a fully expanded field using any scaling function u_a. It should be noted that in equation (5.13) this field has been fully expanded using the Poisson operator p_a. Equation (5.15) allows us to expand the field by mixing the operators u_a and p_a, which is an inhomogeneous expansion.

Note also that due to the properties of convolution, equation (5.17) can be written equivalently as

$$W_{x,a}^{k,\{\psi,p\}} f = a^k \frac{\partial^k}{\partial x^k}\left(f_Q * u_a\right) = a^k\left(f * p_{a_1}^{-1} * \frac{\partial^k}{\partial x^k} u_a\right) =$$

$$= a^k \left(f * p_{a_1}^{-1} * \psi_{x,a}^k \right). \quad (5.18)$$

Equation (5.18) is especially useful when the composite continuous wavelet transform is performed using a wavelet formulated without a smoothing function.

The method for calculating smoothing scaling wavelets assumes that the operators p_{a1}^{-1} and u_{a1} refer to the same scale interval ranging from a_1 to a_0 for p_{a1}^{-1} and from a_0 to a_1 for u. Thus, the continuous wavelet transform operator is a combination of smoothing operators using the same scales. A consequence of these facts is that the convolution of operators will be a stable transformation.

This is confirmed by studying the frequency response of the operator v_{a1} for sources at different depths z_0. In the case of a Gaussian wavelet, the smoothing function g is expressed in the frequency domain as

$$\hat{g} = \exp\left[-\frac{(a\rho)^2}{2} \right]. \quad (5.19)$$

sing the extension from a to a_1 allows us to write the following relations

$$\hat{p}_{a_1}^{-1} = \exp\left[(a_1 - a)\rho\right], \qquad \hat{g}_{a_1} = \exp\left[-\frac{(a_1 - a)^2 \rho^2}{2} \right]. \quad (5.20)$$

Thus

$$\hat{v}_{a_1} = \hat{p}_{a_1}^{-1} \hat{g}_{a_1} = \exp\left[(a_1 - a_0)\rho - \frac{(a_1 - a_0)^2 \rho^2}{2} \right]. \quad (5.21)$$

Calculations show that the smoothing effect due to the "Gaussian" expansion is stronger than the high-frequency enhancement effect introduced by the downward extension operator p_{a1}^{-1}. Therefore, the result is a bandpass filter effect.

It is of interest to use the wavelet transformation technique to describe the dynamic response and simulate damage in a plate-shaped laminated piezoelectric composite sample. The laminated composite plate has a rather complex stress state. This state should be described by a three-dimensional elasticity matrix. In the general case, displacements at an arbitrary point of such a composite plate can be expressed by the following relations

$$u(x, y, z) = u_0(x, y) + z\varphi_x(x, y) + z^2 \alpha_x(x, y) + z^3 \beta_x(x, y)$$

$$\upsilon(x,y,z)=\upsilon_0(x,y)+z\varphi_y(x,y)+z^2\alpha_y(x,y)+z^3\beta_y(x,y)$$

$$w(x,y,z)=w_0(x,y)+z\varphi_z(x,y)+z^2\alpha_z(x,y)+z^3\beta_z(x,y), \quad (5.22)$$

where

u_0, υ_0 and w_0 are the mid-plane displacements;

φ_x, φ_y and φ_z are additional rotations due to shear deformation;

α_x, α_y, α_z, β_x, β_y and β_z are functions of variables x and y.

Based on the mechanical condition of the upper and lower free surfaces of the composite plate, i.e. $\sigma_z = \tau_{zx} = \tau_{zy} = 0$, a set of complex strain constraint conditions can be expressed as

$$\varepsilon_z=\frac{\partial w}{\partial z}\Big|_{-\frac{h}{2}}^{\frac{h}{2}}=0, \quad \gamma_{zx}=\left[\frac{\partial u}{\partial z}+\frac{\partial w}{\partial x}\right]\Big|_{-\frac{h}{2}}^{\frac{h}{2}}=0$$

$$\gamma_{yz}=\left[\frac{\partial \upsilon}{\partial z}+\frac{\partial w}{\partial y}\right]\Big|_{-\frac{h}{2}}^{\frac{h}{2}}=0, \quad (5.23)$$

where

h is the thickness of the composite plate.

Substituting (5.23) into (5.22) allows us to write the following relations for the unknown quantities α_x, α_y, α_z, β_x, β_y and β_z

$$\alpha_x=-\frac{1}{3}\frac{\partial\varphi_z}{\partial x}, \quad \alpha_y=-\frac{1}{3}\frac{\partial\varphi_z}{\partial y}, \quad \alpha_z=0$$

$$\beta_x=-\frac{4}{3h^2}\left(\varphi_x+\frac{\partial w_0}{\partial x}\right); \quad \beta_y=-\frac{4}{3h^2}\left(\varphi_y+\frac{\partial w_0}{\partial y}\right)$$

$$\beta_z=-\frac{4}{3h^2}\varphi_z. \quad (5.24)$$

In this case

$$u(x,y,z)=u_0+z\varphi_x-\frac{4z^3}{3h^2}\left(\varphi_x+\frac{\partial w_0}{\partial x}\right)-\frac{1}{3}z^2\frac{\partial\varphi_z}{\partial x}$$

$$\upsilon(x,y,z)=\upsilon_0+z\varphi_y-\frac{4z^3}{3h^2}\left(\varphi_y+\frac{\partial w_0}{\partial y}\right)-\frac{1}{3}z^2\frac{\partial\varphi_z}{\partial y}$$

$$w(x,y,z)=w_0+\left(z-\frac{4z^3}{3h^2}\right)\varphi_z\,. \qquad (5.25)$$

The ratios of deformation and displacement are determined by the expressions

$$\varepsilon_x=\frac{\partial u}{\partial x}=\frac{\partial u_0}{\partial x}+z\frac{\partial\varphi_x}{\partial x}-\frac{4z^3}{3h^2}\left(\frac{\partial\varphi_x}{\partial x}+\frac{\partial^2 w_0}{\partial x^2}\right)-\frac{z^2}{3}\frac{\partial^2\varphi_z}{\partial x^2}$$

$$\varepsilon_y=\frac{\partial\upsilon}{\partial y}=\frac{\partial\upsilon_0}{\partial y}+z\frac{\partial\varphi_y}{\partial y}-\frac{4z^3}{3h^2}\left(\frac{\partial\varphi_y}{\partial y}+\frac{\partial^2 w_0}{\partial y^2}\right)-\frac{z^2}{3}\frac{\partial^2\varphi_z}{\partial y^2}$$

$$\varepsilon_z=\frac{\partial w}{\partial z}=\left(1-\frac{4z^2}{h^2}\right)\varphi_z$$

$$\gamma_{yz}=\frac{\partial w}{\partial y}+\frac{\partial\upsilon}{\partial z}=\left(1-\frac{4z^2}{h^2}\right)\cdot\left(\varphi_y+\frac{\partial w_0}{\partial y}+\frac{z}{3}\frac{\partial\varphi_z}{\partial y}\right)$$

$$\gamma_{zx}=\frac{\partial w}{\partial x}+\frac{\partial u}{\partial z}=\left(1-\frac{4z^2}{h^2}\right)\cdot\left(\varphi_x+\frac{\partial w_0}{\partial x}+\frac{z}{3}\frac{\partial\varphi_z}{\partial x}\right)$$

$$\gamma_{xy}=\frac{\partial u}{\partial y}+\frac{\partial\upsilon}{\partial x}=\left(\frac{\partial u_0}{\partial y}+\frac{\partial\upsilon_0}{\partial x}\right)+\left(z-\frac{4z^2}{3h^2}\right)\times$$

$$\times\left(\frac{\partial\varphi_x}{\partial y}+\frac{\partial\varphi_y}{\partial x}\right)-\frac{2z^2}{3}\frac{\partial^2\varphi_z}{\partial x\partial y}-\frac{8z^3}{3h^2}\frac{\partial^2 w_0}{\partial x\partial y}. \tag{5.26}$$

For a standard specimen in the form of a composite plate, the strain–stress relationship in the k^{th} layer with anisotropic behavior is given by

$$\{\sigma\}=\left[\overline{Q}\right]\{\varepsilon\}, \tag{5.27}$$

where
$\{\sigma\}$ and $\{\varepsilon\}$ are the stress and strain vectors, respectively;
$|Q|$ is the elasticity matrix, and it depends on the elastic moduli E_1, E_2 and E_3, shear moduli G_{12}, G_{23} and G_{31}, Poisson's ratios μ_{12}, μ_{23} and μ_{31}, and the k^{th} ply fibre orientation angle θ_k.

In piezoelectric plates built into a composite plate as sensors and actuators, the direct and inverse piezoelectric equations regarding the *x* - *y* - *z* axes can be written as follows

$$\{\sigma_P\}=\left[Q_P\right]\{\varepsilon\}-\left[e\right]^T\{E\} \tag{5.28}$$

$$\{D\}=\left[e\right]\{\varepsilon\}-\left[\bar{\varepsilon}\right]\{E\}, \tag{5.29}$$

where
$\{\sigma_P\}$ and $[Q_P]$ is the stress vector and the transformed elasticity matrix of the piezoelectric material, respectively;
$\{E\}$ is the electric field strength vector;
$\{D\}$ is the electrical displacement vector;
$[\varepsilon]$ is the relative permittivity matrix;
$[e]^T$ is the transposed matrix with respect to [e].

The matrix of piezoelectric stress coefficients [*e*] is expressed through the matrix of strain coefficients [*d*] by the equations

$$\left[e\right]=\left[d\right]\left[Q_p\right]. \tag{5.30}$$

he elasticity matrix of a piezoelectric material can be represented in the following form

$$[Q_P] = \begin{bmatrix} Q_{P11} & Q_{P12} & Q_{P13} & 0 & 0 & 0 \\ Q_{P21} & Q_{P22} & Q_{P23} & 0 & 0 & 0 \\ Q_{P31} & Q_{P32} & Q_{P33} & 0 & 0 & 0 \\ 0 & 0 & 0 & Q_{P44} & 0 & 0 \\ 0 & 0 & 0 & 0 & Q_{P55} & 0 \\ 0 & 0 & 0 & 0 & 0 & Q_{P66} \end{bmatrix}. \quad (5.31)$$

Due to the approximate isotropy of the sample, a sufficiently large number of elements of the [Q_P] matrix are identical, in particular

$$Q_{P11} = Q_{P22} = Q_{P33} = \frac{E_P(1-\mu_P)}{(1+\mu_P)\cdot(1-2\mu_P)}$$

$$Q_{P44} = Q_{P55} = Q_{P66} = \frac{E_P}{2(1+\mu_P)}$$

$$Q_{P12} = Q_{P13} = Q_{P21} = Q_{P23} = Q_{P31} = Q_{P32} =$$

$$= \frac{E_P\mu_P}{(1+\mu_P)\cdot(1-2\mu_P)}, \quad (5.32)$$

where

E_P is the elastic modulus;

μ_P is the Poisson's rat io of piezoelectric materials.

The piezoelectric constant matrix [d] indicates the quantitative relationship between the excitation voltage acting on the piezoelectric material and the induced voltage in the piezoelectric material. For a three-dimensional model, the specified matrix can be written in the form

$$[d] = \begin{bmatrix} d_{11} & d_{12} & d_{13} & d_{14} & d_{15} & d_{16} \\ d_{21} & d_{22} & d_{23} & d_{24} & d_{25} & d_{26} \\ d_{31} & d_{32} & d_{33} & d_{34} & d_{35} & d_{36} \end{bmatrix}. \quad (5.33)$$

The matrix [*d*] of a piezoelectric has some features that are due to the special characteristics of the material, that is, all elements are equal to 0, with the exception of $d_{31} = d_{32} \neq 0$, $d_{15} = d_{24} \neq 0$ and $d_{33} \neq 0$.

Consider the case when the piezoelectric sensors and actuator are polarized only along the *z*-direction thickness, that is, the excitation vector {*E*} is equal to {0; 0; V_3}^{T} , where V_3 is the electric field strength acting on the piezoelectric materials along the *z*-direction for equation. Moreover, it should be noted that stresses and strains have non-zero components only along the main diagonals associated with the coordinate axes. At the same time, for quantities τ and γ only non-diagonal components should be considered as non-zero quantities.

Then (5.28) and (5.29) can be written as

$$\begin{Bmatrix} \sigma_x \\ \sigma_y \\ \sigma_z \\ \tau_{yz} \\ \tau_{zx} \\ \tau_{xy} \end{Bmatrix} = [Q_P] \begin{Bmatrix} \varepsilon_x \\ \varepsilon_y \\ \varepsilon_z \\ \gamma_{yz} \\ \gamma_{zx} \\ \gamma_{xy} \end{Bmatrix} - [Q_P]^T [d]^T \begin{Bmatrix} 0 \\ 0 \\ V_3 \end{Bmatrix} \tag{5.34}$$

$$\begin{Bmatrix} D_1 \\ D_2 \\ D_3 \end{Bmatrix} = [d][Q_P] \begin{Bmatrix} \varepsilon_x \\ \varepsilon_y \\ \varepsilon_z \\ \gamma_{yz} \\ \gamma_{zx} \\ \gamma_{xy} \end{Bmatrix} + [\bar{\varepsilon}] \begin{Bmatrix} 0 \\ 0 \\ V_3 \end{Bmatrix}. \tag{5.35}$$

According to the damage theory of composite micromechanics, when delamination occurs in the $D_l \times D_b$ region of the composite structure, a numerical damage model can be created by analyzing the microstructure. The mechanical parameters of a thin composite plate depending on the damage delamination can be expressed as

$$E_1^d = E_1^0 + 2\omega_d \left[C_3 + C_6 \left(\mu_{12}^0 \right)^2 - C_{12} \mu_{12}^0 \right],$$

$$E_2^d = E_2^0 + 2\omega_d \left[C_6 + C_3 \left(\mu_{21}^0 \right)^2 - C_{12} \mu_{21}^0 \right]$$

$$\mu_{12}^d = \mu_{12}^0 + \omega_d \frac{1 - \mu_{12}^0 \mu_{21}^0}{E_2^0} \left[C_{12} - 2C_6 \mu_{12}^0 \right]$$

$$G_{12}^d = G_{12}^0 + 2\omega_d C_9, \tag{5.36}$$

where
E_1^d , E_2^d, μ_{12}^d and G_{12}^d are the two elastic moduli, Poisson's ratio and shear modulus of the composite plate with delamination damage, respectively;
E_1^0 , E_2^0, μ_{12}^0 and G_{12}^0 are the elastic moduli, Poisson's ratio and shear modulus of the intact composite plate, respectively.

Let us denote by the symbol ω_d a variable that reflects the damage from delamination in a composite plate, and which is related to the size and distribution density of the delamination area. The expression for the delamination damage variable can be written as

$$\omega_d = \eta \, \bar{r}_C , \tag{5.37}$$

where
η is the delamination distribution density of the composite region.

The delamination distribution density of a region is equal to the ratio of all delamination areas in an element to the entire area of the element where multiple delamination areas occur. Let us denote by the symbol r_C the average radius of all delamination sections in this element. Values η and r_C can be written according to the following relations

$$\eta = \frac{\sum_{i=1}^{N_d} S_i}{D_l \times D_b}, \qquad \bar{r}_C = \sqrt{\frac{1}{\pi N_d} \sum_{i=1}^{N_d} S_i} \, . \tag{5.38}$$

The values C_3, C_6, C_9 and C_{12} are material coefficients that do not depend on deformations and damage, but depend on the configuration of the composite, i.e. geometry and fiber orientation. In addition, these values depend on the volume fraction of fibers in the sequence of laying layers.

Typically, delamination damage results in a decrease in the elastic modulus of the composite plate. Among other things, it can be argued that the smaller the

delamination area, the less the impact on the change in the mechanical characteristics of the composite plate. Consider the case where the delamination area is very small, for example, $\eta < 1\%$. Then we can assume that this delamination affects only the local mechanical properties of the plate. Therefore, it is logical to assume that in the dynamic model of a composite plate, a change in mechanical properties occurs locally only in the damage zone, and the mechanical properties of other areas do not change.

Hamilton's principle is used to derive the equations of motion of a multilayer composite plate with integrated piezoelectric sensors and actuator. Hamilton's principle can be written as follows

$$\int_{t_1}^{t_2} \left(\delta T - \delta U + \delta W \right) dt = 0, \tag{5.39}$$

where
t_1, t_2 are the two arbitrary time instants;
T is the kinetic energy;
U is the strain energy;
W is the work done by an external electric field;
δ is a first order variation.

The shift in the deformation field in an element can be expressed as the following formulas

$$u(x, y, z) = \sum_{i=1}^{n} \left\{ N_i \left[u_{0i} + \left(z - \frac{4z^3}{3h^2} \right) \varphi_{xi} \right] - \right.$$

$$\left. - \frac{\partial N_i}{\partial x} \left(\frac{1}{3} z^2 \varphi_{zi} + \frac{4z^3}{3h^2} w_{0i} \right) \right\}$$

$$\upsilon(x, y, z) = \sum_{i=1}^{n} \left\{ N_i \left[\upsilon_{0i} + \left(z - \frac{4z^3}{3h^2} \right) \varphi_{yi} \right] - \right.$$

$$\left. - \frac{\partial N_i}{\partial y} \left(\frac{1}{3} z^2 \varphi_{zi} + \frac{4z^3}{3h^2} w_{0i} \right) \right\}$$

$$w(x,y,z)=\sum_{i=1}^{n}\left\{N_i\left[\upsilon_{0i}+\left(z-\frac{4z^3}{3h^2}\right)\varphi_{zi}\right]\right\}, \qquad (5.40)$$

where
$N_i(x,y)$ is the element shape function;
n is the number of nodes in an element;
u_{0i}, υ_{0i}, w_{0i}, φ_{xi}, φ_{yi} and φ_{zi} are the values of u_0, υ_0, w_0, φ_x, φ_y and φ_z at the i^{th} node, respectively.

The elementary equations of motion satisfy the following relation

$$[M]^e\{\ddot{\Delta}\}^e+[K]^e\{\Delta\}^e=\{F_P\}^e U_P^e, \qquad (5.41)$$

where
$[M]^e$ and $[K]^e$ are the element mass and stiffness matrices;
U_p^e is the voltage applied to the piezoelectric actuator;
$\{F_P\}^e$ is the vector indicating the force magnitude produced by unit voltage applied to the piezoelectric patch, it converts the applied actuator voltage to the induced force;
$\{\Delta\}^e$ is the element's nodal displacement vector, which can be expressed using the following formula

$$\{\Delta\}^e=\left\{(\Delta_1)^T,(\Delta_2)^T,\ldots,(\Delta_n)^T\right\}^T \qquad (5.42)$$

$$\{\Delta_i\}=\left\{u_{0i},\upsilon_{0i},w_{0i},\varphi_{xi},\varphi_{yi}\right\}^T. \qquad (5.43)$$

When a piezoelectric actuator embedded in a damaged structure is driven by an input voltage signal with multiple frequency components to excite vibration of the structure, a significant difference will be observed between the dynamic response energy and the energy of the intact structure in the same frequency range. The reason for these features is that structural damage will suppress or enhance certain components of the response signal in special frequency ranges, i.e. structural damage can cause an increase in the energy of some components of the response signal, as well as a decrease in the energy of other components of the response signal.

It can therefore be argued that the energy of structural dynamic response signals with different frequency components contains extensive information about structural damage, and changes in the energy of one or more frequency components of the signals can indicate a particular structural damage status. Many

vibration parameters such as natural frequency, mode shape, modal damping can be used to determine the structural damage status.

Wavelet analysis of time-varying signal is a kind of localization analysis method in the time and frequency domain, and the time and frequency windows can be changed. This method of signal processing is characterized by higher frequency and time resolution.

The continuous wavelet transform of the function *f* (*t*) is determined using the relation

$$W_f(a,b) = |a|^{0.5} \int_R f(t)\psi^*(\xi')dt, \tag{5.44}$$

where

$\xi' = (t - b)/a$;

b is the translation parameter;

a is the scale parameter;

$\Psi(\xi)$ is the mother wavelet.

The recomposition equation can be expressed as

$$f(t)C_\Psi^{-1} \int_{-\infty}^{\infty} \int_{-\infty}^{\infty} a^{-2} W_f(a,b)\Psi(\xi')dadb, \tag{5.45}$$

where

$$C_\Psi = 2\pi \int_0^\infty |\Psi(r)|^2 \frac{dr}{r}. \tag{5.46}$$

The basic wavelet function can be represented in many ways. One of the most developed methods in practice is wavelet packet analysis of the base function. In particular, suppose that $g_j^n(t) \in U_j^n$ then the value $g_j^n(t)$ can be represented as the following relation

$$g_j^n(t) = \sum_l d_l^{j,n} u_n\left(2^j t - 1\right). \tag{5.47}$$

Calculation formulas for the quantities $\{d_l^{j,2n}\}$ and $\{d_l^{j,2n+1}\}$ have the following form

$$d_l^{j,2n} = \sum_k a_{k-2l} d_k^{j+1,n} \tag{5.48}$$

$$d_l^{j,2n+1} = \sum_k b_{k-2l} d_k^{j+1,n} . \tag{5.49}$$

In this case, the recomposition $\{d_l^{j+1,n}\}$ can be represented in the following form

$$d_l^{j+1,n} = \sum_k \left(h_{l-2k} d_k^{j,2n} + g_{l-2k} d_k^{j,2n+1} \right). \tag{5.50}$$

The choice of a fixed frequency band in accordance with the characteristics of the analyzed signal can be carried out using packet wavelet analysis. At the same time, resolution in the frequency and time domains can be improved.

Obtaining a formation about structural damage from a response signal involves preliminary decomposition of the signal into several subsignals in different frequency ranges using a packet wavelet transform. Let us assume that the original signal $S(t)$ of the structural response has the following form

$$S(t) = \sum_{j=0}^{2^{k-1}} S_{k,j}(t), \tag{5.51}$$

where
$S_{k,j}(t)$ is the decomposed wavelet sub-signal with orthogonal frequency band;
k indicates the k^{th} layer of the tree structure of wavelet decomposition.

The total number of decomposed wavelet signals does not exceed 2^{k-1}.

The signal energy with index j is equal to

$$U_{k,j} = \int_0^T \left| S_{k,j}(t) \right|^2 dt , \tag{5.52}$$

where T is the sampling time.

The response signal is characterized by a total energy

$$U = \left\{ \sum_{j=0}^{2^{k-1}} \left| U_{k,j} \right|^2 \right\}^{0.5} . \tag{5.53}$$

The dimensionless components of the intact index vector for a laminated composite plate are determined using the following formulas

$$V^0 = \left\{c_1^0, c_2^0, c_3^0, \ldots, c_{2^{k-1}}^0\right\} =$$

$$= \left\{\frac{U_{k,1}^0}{U^0}, \frac{U_{k,2}^0}{U^0}, .\frac{U_{k,2}^0}{U^0}, \ldots, \frac{U_{k,2^{k-1}}^0}{U^0}\right\} \tag{5.54}$$

$$V^d = \left\{c_1^d, c_2^d, c_3^d, \ldots, c_{2^{k-1}}^d\right\} =$$

$$= \left\{\frac{U_{k,1}^d}{U^d}, \frac{U_{k,2}^d}{U^d}, .\frac{U_{k,2}^d}{U^d}, \ldots, \frac{U_{k,2^{k-1}}^d}{U^d}\right\}, \tag{5.55}$$

where
index “0” corresponds to an undamaged composite plate;
index “d” corresponds to a damaged (detached) composite plate.

Typically, a comparison of V_0 and V_d indicates whether there is delamination of the plate. As additional information, it can be argued that the change in the relative value of V_0/V_d in each element can more clearly indicate the degree of delamination of the plate. The above serves as a basis for exploring the delamination region using a similar index vector, which is defined as follows

$$V_C = \left\{\left(1 - \frac{c_1^d}{c_1^0}\right), \left(1 - \frac{c_2^d}{c_2^0}\right), \left(1 - \frac{c_3^d}{c_3^0}\right), \ldots, \left(1 - \frac{c_{2^{k-1}}^d}{c_{2^{k-1}}^0}\right)\right\}. \tag{5.56}$$

For composite plates with different delamination zone sizes, changes in local elastic moduli can be calculated using experimental data for delamination parameters C_3, C_6, C_9 and C_{12}. Numerical modeling of the dynamic responses of composite plates with different sizes and locations of delamination zones was carried out.

The energy spectrum of the decomposed wavelet signal from the structural dynamic response may indicate a state of structural delamination. This is based on the fact that when small and local damage occurs in the structure under the same

excitation condition, the change in the contribution of each vibration mode is different, i.e., some modes are enhanced and others are weakened.

In the numerical simulation, the output signals of four piezoelectric patch sensors are decomposed into 16 sub-signals using wavelet packet analysis, and the frequency band does not overlap due to the orthogonality of the adopted Daubechies wavelet base. Time domain wavelet decomposition waveforms from intact and damaged composite plates cannot directly indicate the damage state of the plate. However, their energy spectrum can clearly reflect the status of structural damage. In practical problems, one of the most interesting questions is to find the smallest degree of detectable structural damage.

Wavelet analysis was applied to the results of a basic stress clamp experiment on a composite plate that consisted of a glass fiber and epoxy matrix material with 17 layers with orientation angles of 0 and 90°. The elasticity parameters of the intact composite were in the range $E^0 \in (4.58 \div 47.52)$ GPa, $G^0 = 2.2$ GPa. The density of the composite material was $\rho = 1.85 \cdot 10^3$ kg/m^3.

One piezoelectric sensor mounted in a composite plate was used as a signal source-actuator, and four more piezoelectric sensors were used as receivers. The results of the experiment are presented in Table 15 (parameter β is equal to the ratio of the delamination area to the total area of the composite plate, *N* is the wavelet serial number).

Table 15. Damage index vector V_C (%) of a composite plate for different sizes of the delamination zone

N	β, %							
	0.003	0.018	0.030	0.060	0.100	0.120	0.167	0.212
	Vc, %							
0	0.005	0.130	0.389	0.765	1.277	2.096	2.434	2.005
1	0.601	2.791	4.914	7.323	7.642	5.528	5.957	13.31
2	-0.072	-0.359	-0.662	-0.576	0.157	1.249	3.668	2.218
3	-0.043	-0.113	-0.214	-1.129	-1.110	1.021	2.160	0.757
4	0.602	2.594	3.951	1.790	-8.499	-27.82	-44.33	-31.11
5	0.819	3.974	7.507	12.38	12.58	7.341	5.212	18.21
6	0.062	0.325	0.470	-0.089	0.043	1.103	1.519	2.514
7	0.481	2.164	3.903	6.813	7.298	4.598	5.441	11.89
8	-0.128	-0.612	-1.013	-0.694	0.454	1.918	3.031	0.582
9	0.516	2.344	4.003	4.917	3.784	1.813	-0.045	3.172
10	-0.142	-0.589	-0.929	-1.108	-0.155	2.585	4.544	1.944
11	-0.055	-0.328	-0.651	-0.575	0.041	0.447	1.226	0.132
12	0.348	1.405	1.878	-0.487	-7.626	-19.97	-31.15	-23.84
13	0.549	2.420	4.108	5.765	4.383	-0.665	-2.673	5.849
14	-0.131	-0.579	-0.932	-0.896	-0.062	1.819	3.910	2.169
15	-0.039	-0.142	0.192	-0.276	0.130	1.896	3.312	7.829

Numerical data indicate that variations in multiples of the damage index vector *Vc* indicate the presence of a delamination zone in the composite plates. If the maximum absolute value of an element in the index vector exceeds some threshold, such as 20%, this data set can be used to indicate delamination damage to a certain extent. Thus, it can be found that the smallest detectable delamination area *S'* will be $S' \leq 0{,}12$ % of the total area of the composite plate.

The set of all data, which contains all the sizes and locations of damage from delaminations, was created using numerical modeling. Such a set can be used for online detection of damage to structures in service, subject to the necessary condition of sufficient accuracy of the simulations. A comparison of the results of numerical simulation A and experiment B (deviation C') is given in Table 16.

Table 16. Vector of delamination index V'c (%) of composite plate obtained by simulation and experiment

N	β, %								
	0.11			0.167			0.22		
	A	B	C'	A	B	C'	A	B	C'
	V'_C, %								
0	1.543	1.703	10.3	2.433	2.491	2.35	0.895	0.908	1.4
1	7.162	8.053	12.4	5.956	6.078	2.04	21.13	21.32	0.9
2	0.377	0.403	6.79	3.668	3.178	1.38	-0.991	-1.005	0.9
3	-0.569	-0.634	11.4	2.160	2.197	1.70	-1.759	-1.818	3.3
4	-13.79	-14.10	2.24	-44.32	-45.38	2.38	-6.506	-6.603	1.4
5	11.38	12.83	12.7	5.212	5.221	0.17	35.48	36.42	2.6
6	0.381	0.395	3.52	1.518	1.546	1.80	3.599	3.626	0.7
7	6.593	6.811	3.28	5.441	5.449	0.15	17.18	17.76	3.4
8	0.863	0.961	11.3	3.030	3.068	1.24	-2.687	-2.736	1.8
9	3.262	3.575	9.58	-0.045	-0.045	0.91	8.339	8.691	4.2
10	0.551	0.561	1.77	4.543	4.663	2.62	-1.228	-1.279	4.1
11	0.164	0.165	0.15	1.226	1.226	0.04	-2.321	-2.389	2.9
12	-11.02	-12.30	11.6	-31.15	-31.89	2.30	-7.936	-8.129	2.4
13	3.063	3.143	2.58	-2.673	-2.751	2.91	16.31	17.04	4.4
14	0.397	0.412	3.88	3.910	4.026	2.97	-1.147	-1.193	4.0
15	0.554	0.602	8.59	3.311	3.390	2.36	0.218	0.225	3.1

The results shown in Table 16 indicate that the larger the maximum absolute value $V'_{c,\,max}$ of an element in the index vector, the smaller the deviation between simulations and experiments will be. These phenomena mean that only differences in the wavelet energy spectrum between undamaged and damaged composite plates are noticeable, and the simulation results are reliable.

CHAPTER 6
LAMB WAVES

Such features of composite material samples as homogeneity on the one hand and the presence of deformations on the other have traditionally been assessed using non-destructive testing. Monitoring the condition of structures can be considered as a modernization of this technique and the purpose of ensuring guarantees of the operability of structures. For active diagnostics, which use ultrasonic transient waves for damage detection, localization and subsequent damage assessment, understanding the wave propagation characteristics of composites is essential for the successful application of these techniques.

Wave propagation in composites is complex due to the nature of the inhomogeneity of the components, the intrinsic anisotropy of the material and the multilayer structure, which leads to the fact that the speed of the wave mode macroscopically depends on the laying of the laminate and the direction of the wave. conditions of its distribution and frequency.

In the case of wave propagation in isotropic plate structures, they will experience repeated reflections alternately on the upper and lower surfaces, and the resulting wave propagation as a result of their mutual interference is directed by the surfaces of the plates. A guided wave can be modeled by imposing surface boundary conditions on the equations of motion.

A significant disadvantage of this approach is the presence of dispersion, that is, the speed of propagation of a directed wave along the plate is a function of frequency or wavelength. Dispersion relations for an inelastic isotropic plate with an infinitely extended plane-strain state were first obtained by Lamb. As a rule, directed waves propagating along the plane of an elastic plate with boundaries free from mechanical stress are called Lamb waves.

Wave interactions in multilayer composites depend on the properties of the composite layers, geometry, direction of propagation, frequency and interfacial conditions. In the case where the wavelengths significantly exceed the dimensions of the components of the composites, namely, the diameters of the fibers and the distance between them, each plate can be considered as an equivalent homogeneous and isotropic material with an axis of symmetry parallel to the fibers. A fairly large number of works are devoted to wavelet transforms using the Lamb wave algorithm [188 – 202]. Damage assessment in composites using Lamb waves was carried out by Paget, Su and Lemister. The theoretical basis of the interaction of Lamb waves with deformations in composite structures was discussed in the work of Alleyne and Cawley.

Symmetric laminar composites are characterized by symmetric and antisymmetric Lamb wave modes. For symmetric modes, one type is designated quasi-extended (qS_n), where the dominant component of the polarization vector is along the propagation direction, and the other type is quasi-horizontal shear

(qSH_{2n}), where the polarization vector is predominantly parallel to the plane of the plate. It can also be argued that for antisymmetric types of wave modes, quasi-flexural (qA_n) and quasi-horizontal shear (qSH_{2n-1}) are generated.

In general, in composite materials there are transient waves that propagate in an arbitrary direction, and which generally cause disturbances involving all three displacement components, namely, the generalized plane strain due to the anisotropy of the material.

Consider a Cartesian coordinate system in which the *Z*-axis is perpendicular to the midplane of the composite laminate, spanned by the *X* and *Y*. The two outer surfaces of the laminate are at $z = \pm h/2$. The propagation of a Lamb wave packet in the θ-direction can be considered as occurring counterclockwise with respect to the *x*-axis. Each layer of a composite laminate with an arbitrary orientation in the global Cartesian coordinate system (*x*, *y*, *z*) is considered as a monoclinic material having an *x*-*y* symmetry plane. Taking this into account, the dependence of stress on strain can be represented in the following matrix form

$$\begin{Bmatrix} \sigma_x \\ \sigma_y \\ \sigma_z \\ \tau_{yz} \\ \tau_{xz} \\ \tau_{xy} \end{Bmatrix} = \begin{bmatrix} C_{11} & C_{12} & C_{13} & & & C_{16} \\ C_{12} & C_{22} & C_{23} & & & C_{26} \\ C_{13} & C_{23} & C_{33} & & & C_{36} \\ & & & C_{44} & C_{45} & \\ & & & C_{45} & C_{55} & \\ C_{16} & C_{26} & C_{36} & & & C_{66} \end{bmatrix} \cdot \begin{Bmatrix} \varepsilon_x \\ \varepsilon_y \\ \varepsilon_z \\ \gamma_{yz} \\ \gamma_{xz} \\ \gamma_{xy} \end{Bmatrix}. \quad (6.1)$$

When the global coordinate system (*x*, *y*, *z*) does not coincide with the main material coordinate system (*x*′, *y*′, z) of each layer, but makes an angle ϕ with the *x*-axis, the stiffness matrix C_{ij} (*i, j* = 1, 2, 3, , 6) in the syste (*x*, *y*, *z*) can be obtained from the plate stiffness matrix C'_{ij} in the system (*x*′, *y*′, *z*) using the transformation matrix method. The composite plate is orthotropic or transversely isotropic with respect to the principal axes of the material at (*x*′, *y*′, *z*), and its plate stiffness matrix C'_{ij} can be calculated from the elastic properties of the plate material E_k, ν_{kl} and G_{kl} (*k, l* = 1, 2, 3).

The relationship between the deformation and displacement coefficients is as follows

$$\varepsilon_x = \frac{\partial u}{\partial x}, \quad \varepsilon_y = \frac{\partial \upsilon}{\partial y}, \quad \varepsilon_z = \frac{\partial w}{\partial z}, \quad \gamma_{yz} = \frac{\partial \upsilon}{\partial z} + \frac{\partial w}{\partial y} \quad (6.2)$$

$$\gamma_{xz} = \frac{\partial u}{\partial z} + \frac{\partial w}{\partial x}, \qquad \gamma_{xy} = \frac{\partial u}{\partial y} + \frac{\partial \upsilon}{\partial x}, \tag{6.3}$$

where
u, υ and w are the displacements in the x, y, and z-directions, respectively.

For the case of the absence of mass forces, the equations of motion have the following form

$$\frac{\partial \sigma_x}{\partial x} + \frac{\partial \tau_{xy}}{\partial y} + \frac{\partial \tau_{xz}}{\partial z} = \rho \ddot{u} \tag{6.4}$$

$$\frac{\partial \tau_{xy}}{\partial x} + \frac{\partial \sigma_y}{\partial y} + \frac{\partial \tau_{yz}}{\partial z} = \rho \ddot{\upsilon} \tag{6.5}$$

$$\frac{\partial \tau_{xz}}{\partial x} + \frac{\partial \tau_{yz}}{\partial y} + \frac{\partial \sigma_z}{\partial z} = \rho \ddot{w}, \tag{6.6}$$

where
ρ is the mass density of composite.

The boundary conditions on the upper and lower faces have the form

$$\sigma_z = \tau_{xz} = \tau_{yz} = 0, \quad \text{at} \quad z = \pm h/2. \tag{6.7}$$

Wave motion can be expressed as a superposition of plane harmonic waves due to the fact that Lamb waves propagate along the plane of the plate with boundaries free from adhesion forces, but are standing waves in the z direction of the plate. For each plane harmonic wave that propagates in the direction normal to the wave front, we can write the following relation

$$\{u, \upsilon, w\} = \{U(z), V(z), W(z)\} \exp\{i[(k_x x + k_y y) - \omega t]\}, \tag{6.8}$$

where
$\boldsymbol{k} = [k_x, k_y]^T$,
$k = |\boldsymbol{k}| = (k_x^2 + k_y^2)^{0.5} = \omega / c_P = 2\pi / \lambda$ is the wave number;
λ is the wavelength;
ω is the angular frequency;
c_P is the phase velocity.

Substituting (6.8) into (6.1) and (6.3) allows one to obtain relations for mechanical stresses in each layer of the composite

$$\sigma_x = \left[C_{11}k_xU + C_{12}k_yV - iC_{13}W' + \right.$$

$$\left. + C_{16}\left(k_yU + k_xV\right)\right]\cdot i\exp\left\{i\left[\left(k_xx + k_yy\right) - \omega t\right]\right\} \qquad (6.9)$$

$$\sigma_y = \left[C_{12}k_xU + C_{22}k_yV - iC_{23}W' + \right.$$

$$\left. + C_{26}\left(k_yU + k_xV\right)\right]\cdot i\exp\left\{i\left[\left(k_xx + k_yy\right) - \omega t\right]\right\} \qquad (6.10)$$

$$\sigma_z = \left[C_{13}k_xU + C_{23}k_yV - iC_{33}W' + \right.$$

$$\left. + C_{36}\left(k_yU + k_xV\right)\right]\cdot i\exp\left\{i\left[\left(k_xx + k_yy\right) - \omega t\right]\right\} \qquad (6.11)$$

$$\tau_{yz} = \left[C_{44}\left(V' + ik_YW\right)\right] + C_{45}\left(U' + ik_xW\right)\right]\times$$

$$\times i\exp\left\{i\left[\left(k_xx + k_yy\right) - \omega t\right]\right\} \qquad (6.12)$$

$$\tau_{xz} = \left[C_{45}\left(V' + ik_YW\right)\right] + C_{55}\left(U' + ik_xW\right)\right]\times$$

$$\times i\exp\left\{i\left[\left(k_xx + k_yy\right) - \omega t\right]\right\} \qquad (6.13)$$

$$\tau_{xy} = \left[C_{16}k_xU + C_{26}k_yV - iC_{36}W' + C_{66}\left(k_yU + k_xV\right)\right] \times$$

$$\times i\exp\left\{i\left[\left(k_xx + k_yy\right) - \omega t\right]\right\} \qquad (6.14)$$

where the prime denotes the derivative with respect to *z*.

Substitution (6.9) – (6.14) into (6.4) – (6.6) allows us to write the equations of motion for each layer separately. These equations can be divided into symmetric and asymmetric, which simplifies the analytical representation

$$U_S = A_S\cos\xi z, \quad V_S = B_S\cos\xi z, \quad W_S = C_S\cos\xi z \qquad (6.15)$$

$$U_a = A_a \cos \xi z, \quad V_a = B_a \cos \xi z, \quad W_a = C_a \cos \xi z, \quad (6.16)$$

where

ξ is an unknown variable to be determined later;

subscripts «s» and «a» represent symmetric and anti-symmetric modes, respectively.

Let us consider the case of symmetric modes. Substituting (6.15) – (6.16) into the equations of motion for each layer allows us to write the relationships in matrix form

$$\begin{bmatrix} \Gamma_{11} - \rho\omega^2 & \Gamma_{12} & \Gamma_{13} \\ \Gamma_{12} & \Gamma_{22} - \rho\omega^2 & \Gamma_{23} \\ \Gamma_{13} & \Gamma_{23} & \Gamma_{33} - \rho\omega^2 \end{bmatrix} \begin{Bmatrix} A_S \\ B_S \\ C_S \end{Bmatrix} = 0, \quad (6.17)$$

where the bar indicates the complex conjugate.

The elements in the above matrix defined by ($\boldsymbol{\Gamma} - \rho\omega^2\boldsymbol{I}$) are listed as follows

$$\Gamma_{11} = C_{11}k_x^2 + 2C_{16}k_xk_y + C_{66}k_y^2 + C_{55}\xi^2 \quad (6.18)$$

$$\Gamma_{12} = C_{16}k_x^2 + (C_{12} + C_{66})k_xk_y + C_{26}k_y^2 + C_{45}\xi^2 \quad (6.19)$$

$$\Gamma_{13} = -i\left[(C_{13} + C_{55})k_x + (C_{36} + C_{45})k_y\right]\xi \quad (6.20)$$

$$\Gamma_{22} = C_{66}k_x^2 + 2C_{26}k_xk_y + C_{22}k_y^2 + C_{44}\xi^2 \quad (6.21)$$

$$\Gamma_{23} = -i\left[(C_{36} + C_{45})k_x + (C_{23} + C_{44})k_y\right]\xi \quad (6.22)$$

$$\Gamma_{33} = C_{55}k_x^2 + 2C_{45}k_xk_y + C_{44}k_y^2 + C_{33}\xi^2, \quad (6.23)$$

where $\boldsymbol{I}$ is a 3×3 identity matrix.

Relation (6.17) is a standard linear problem on the eigenvalues of the Hermitian matrix $\boldsymbol{\Gamma}$. If the matrix is positive definite, it can be shown that the eigenvalues $\rho\omega^2$ of the matrix $\boldsymbol{\Gamma}$ are positive and non-zero, moreover, the right eigenvectors satisfy the orthogonality property.

For non-trivial solutions A_s, B_s and C_s in equation (6.17), by vanishing the determinant of the matrix ($\boldsymbol{\Gamma} - \rho\omega^2\boldsymbol{I}$) we can obtain the following sixth-order polynomial in ξ

$$\xi^6 + \alpha_1 \xi^4 + \alpha_2 \xi^2 + \alpha_3 = 0, \tag{6.24}$$

where

α_i (i = 1, 2, 3) are real-valued coefficients of C_{ij}; k and $\rho\,\omega^2$.

Analysis of the ratios leads to the fact that only three positive, non-zero and discrete values of ξ_i (i = 1, 2, 3) can be obtained. For each ξ_i in symmetric modes, we can write the formal dependence of B_S and C_S on A_S in the form

$$B_S = f_1(A_S) = \frac{(\Gamma_{11} - \rho\omega^2)\Gamma_{23} - \Gamma_{12}\Gamma_{13}}{\Gamma_{13}(\Gamma_{22} - \rho\omega^2) - \Gamma_{12}\Gamma_{23}} A_S = RA_S \tag{6.25}$$

$$C_S = f_2(A_S) = \frac{\Gamma_{12}^2 - (\Gamma_{11} - \rho\omega^2)(\Gamma_{22} - \rho\omega^2)}{\Gamma_{13}(\Gamma_{22} - \rho\omega^2) - \Gamma_{12}\Gamma_{23}} A_S = iSA_S \tag{6.26}$$

Relations of a similar type ($B_a = RA_a$ and $C_a = -iSA_a$) can also be written for the antisymmetric case. Now we can write down the general solution for the system (6.15) – (6.16)

$$\{U_S, V_S, W_S\} = \sum_{j=1}^{3} A_{Sj} \{\cos\xi_j z,\ R_j \cos\xi_j z,\ iS_j \sin\xi_j z\} \tag{6.27}$$

$$\{U_a, V_a, W_a\} = \sum_{j=1}^{3} A_{aj} \{\sin\xi_j z,\ R_j \sin\xi_j z,\ iS_j \cos\xi_j z\}. \tag{6.28}$$

Substitution (6.27) into (6.9) – (6.14) allows us to write the following relation for the quantities σ_z, τ_{yz} and τ_{xz}

$$(\sigma_z, \tau_{yz}, \tau_{xz})\big|_{z=h/2} = \sum_{j=1}^{3} [H_{1j} \sin(\xi_j z + \varphi), H_{2j} \cos(\xi_j z + \varphi),$$

$$H_{3j} \cos(\xi_j z + \varphi)] A_j = 0, \tag{6.29}$$

where φ_1 = 0 and φ_2 = $\pi/2$ can be associated with symmetric and antisymmetric modes of Lamb waves, in addition

$$H_{1j} = C_{13}k_x + C_{23}k_y R_j + C_{33}\xi_j S_j + C_{36}\left(k_y + k_x R_j\right) \tag{6.30}$$

$$H_{2j} = C_{44}\left(\xi_j R_j + k_y S_J\right) + C_{45}\left(\xi_j + k_x S_j\right) \tag{6.31}$$

$$H_{3j} = C_{45}\left(\xi_j R_j + k_y S_J\right) + C_{55}\left(\xi_j + k_x S_j\right) \tag{6.32}$$

Analysis of the equations allows us to assert that the presence of a nontrivial solution to equation (6.28) is the cause of dispersion relations in closed form, such as

$$H_{11}\left(H_{22}H_{33} - H_{23}H_{32}\right)\tan\left(\frac{\xi_1 h}{2} + \varphi\right) +$$

$$+ H_{12}\left(H_{23}H_{31} - H_{21}H_{33}\right)\tan\left(\frac{\xi_2 h}{2} + \varphi\right) +$$

$$+ H_{13}\left(H_{21}H_{32} - H_{22}H_{31}\right)\tan\left(\frac{\xi_3 h}{2} + \varphi\right). \tag{6.33}$$

This solution is expressed in the form of a transcendental equation that implicitly relates the quantity *x* to *k*. For a fixed *h* a numerical iterative root-finding method is used to calculate the allowable *x* for a range of *k* values. This feature is the basis for the appearance of dispersion relations for the Lamb wave modes in the direction of its propagation. Dispersion relations assume that the frequency x of each mode is a unique function of *k*.

The appearance of Lamb waves in a laminated composite indicates that the interfaces between the layers are perfectly connected. The z-axis displacement components of each layer in equation (6.15) and (6.16) must be modified in exponential form to account for the heterogeneity of the multilayer laminate

$$U = A\exp\left(i\xi z\right), \quad V = B\exp\left(i\xi z\right), \quad W = -iC\exp\left(i\xi z\right). \tag{6.34}$$

In addition, the coefficients in (6.33) can be written in matrix form

$$\left[\Gamma - \rho\omega^2 I\right]\{A,B,C\} = 0. \qquad (6.35)$$

Further, the general solution (6.33) for each layer of the laminate can be represented as

$$\{U,V,W\} = \exp\left\{i\left[\left(k_x x + k_y y\right) - \omega t\right]\right\}. \qquad (6.36)$$

The interlaminar stress components σ_z, τ_{yz} and τ_{xz} in each plate can be expressed as

$$\{\sigma_z, \tau_{yz}, \tau_{xz}\} = ik\exp\left\{i\left[\left(k_x x + k_y y\right) - \omega t\right]\right\} \times$$

$$\times \sum_{j=1}^{6} A_j \left(H_{1j}, H_{2j}, H_{3j}\right)\exp\left(i\xi_j z\right),$$

$$H_{1(j+1)} = H_{1j},\ \ H_{2(j+1)} = -H_{2j},\ \ H_{3(j+1)} = -H_{3j},\ \ j = 1,3,5. \qquad (6.37)$$

In conventional laminar layers, symmetric and antisymmetric modes cannot exist separately. However, when creating composite structures, symmetrical laminates are practically used. Imposing boundary conditions on both the top and middle surfaces of the plane can, however, serve as a reliable method for separating the two types of wave modes. The boundary conditions for the absence of strong bonding on the top surface of the laminate are determined by the expression

$$\{\sigma_z, \tau_{yz}, \tau_{xz}\}\big|_{z=h/2} = 0. \qquad (6.38)$$

The presence of symmetrical geometry and isotropic properties of the laminate material leads to the need to take into account only half of the volume of the laminate. In this case, it seems convenient to take into account the following conditions on the stress and displacement components in the midplane for symmetrical modes

$$\{w, \tau_{yz}, \tau_{xz}\}\big|_{z=0} = 0. \qquad (6.39)$$

The presence of an antisymmetric mode is the reason for the existence of boundary conditions for the average plane of the laminate, which can be written in the form

$$\left\{u, \upsilon, \sigma_z\right\}\Big|_{z=0} = 0. \tag{6.40}$$

The dispersion relation for each Lamb wave mode can be represented as an explicit function $W'(k, \theta)$, which can be considered as a conical surface in a three-dimensional domain. In addition, to describe the dispersion relation between frequency and wave vector, we will use the function $G'(\omega, k)$. In this case, the group velocity of waves can be represented by the relation

$$c_g = -\frac{\left(\partial G' / \partial k\right)}{\left(\partial G' / \partial \omega\right)}. \tag{6.41}$$

For the Cartesian components of the group velocity we will use the following matrix relation

$$\begin{Bmatrix} c_{gx} \\ c_{gy} \end{Bmatrix} = \begin{bmatrix} \cos\theta & -\sin\theta \\ \sin\theta & \cos\theta \end{bmatrix} \begin{Bmatrix} \dfrac{\partial W'}{\partial k} \\ \dfrac{\partial W'}{k\,\partial \theta} \end{Bmatrix}, \tag{6.42}$$

where the subscripts x and y represent the components in x- and y-axes, respectively.

The moduli of group velocity c_g and angle θ are equal

$$c_g = \left(c_{gx}^2 + c_{gy}^2\right)^{0.5}, \quad \theta_g = \tan^{-1}\left(\frac{c_{gy}}{c_{gx}}\right). \tag{6.43}$$

The spatial direction of the group velocity vector for all sets c_g from the origin of the coordinate system at a given frequency can be defined as a wave curve. It is worth noting that the radius vector connecting the origin (or source point) to a point on the wave curve represents the distance traveled by the elastic disturbance per unit time. Thus, the wave curve gives the location of the wave front per unit time from the disturbance emitted by a point source acting through the origin at time $t = 0$.

The dispersion relation can be expressed as the relationship between quantities W', k and θ

$$\frac{\partial W'}{\partial k}\frac{\partial k}{\partial \theta}+\frac{\partial W'}{\partial \theta}=0. \tag{6.44}$$

Taking into account the previous relations, we can also rewrite the formula for the Cartesian components of the group velocity

$$\begin{Bmatrix} c_{gx} \\ c_{gy} \end{Bmatrix} = \begin{bmatrix} \cos\theta & -\sin\theta \\ \sin\theta & \cos\theta \end{bmatrix} \begin{Bmatrix} \dfrac{\partial W'}{\partial k} \\ -\dfrac{\partial W'}{k\,\partial k}\dfrac{dk}{d\theta} \end{Bmatrix}. \tag{6.45}$$

For practical calculation of the wave curve at a given frequency, a method can be used that consists of performing a finite difference of the exact solutions of two slowness curves. These curves represent the locus of points for two fairly close frequencies $\omega_1 \approx \omega_2$. Then the partial derivative of the quantity W' with respect to the wave vector is equal to

$$\left.\frac{\partial W'}{\partial k}\right|_{\omega=\omega_1} \cong \frac{\omega_2-\omega_1}{k_2(\theta)-k_1(\theta)}, \tag{6.46}$$

where k_1 and k_2 are explicit functions of θ.

Spectral dependences of the dimensionless group velocity $c'_g = c_g/c_T$ for fixed values of the dimensionless frequency $f' = \omega h/c_T$ along the θ direction of laminates A_1 $(+45_6/-45_6)_s$ and A_2 $(+45/-45/0/90)_s$ are given in Table 17 and Table 18. Data are given for symmetrical (index “S”) and asymmetrical (index “A”) modes.

Table 17. Spectral dependence for Lamb waves of laminate A_1 (symmetrical modes)

f'	c'_g		f'	c'_g		
	S_0	SH_0		S_1	S_2	SH_2
0.5	3.325	2.384	5.0	0.962	0.001	0.001
1.0	3.218	2.321	5.3	0.947	0.001	0.002
1.5	3.085	2.305	5.6	0.921	0.002	0.003
2.0	2.798	2.208	5.9	0.903	0.854	1.099
2.5	2.237	2.126	6.2	0.824	1.512	1.264
3.0	1.749	2.111	6.5	0.805	2.134	1.452
3.5	0.764	1.872	6.8	0.841	2.358	1.587
4.0	0.387	1.564	7.1	0.893	2.583	1.604
4.5	0.901	0.695	7.4	0.935	2.857	1.698
5.0	1.400	0.631	7.7	0.964	2.940	1.736
5.5	1.399	0.681	8.0	1.045	3.042	1.762
6.0	1.310	0.735	8.3	1.028	3.082	1.829
6.5	1.223	0.761	8.6	1.018	3.110	1.852
7.0	1.182	0.786	8.9	1.066	3.100	1.921
7.5	1.125	0.802	9.2	1.089	3.043	1.964
8.0	1.087	0.811	9.5	1.088	3.002	1.993
8.5	1.022	0.824	9.8	1.081	2.987	2.031
9.0	1.010	0.832	10.1	1.070	2.804	2.057
9.5	1.001	0.840	10.4	1.020	2.451	2.111
10.0	1.000	0.846	10.8	0.993	2.220	2.125
10.5	1.000	0.853	11.1	0.987	1.963	2.134
11.0	0.981	0.859	11.4	0.968	0.995	2.173
11.5	0.980	0.871	11.7	0.969	0.729	2.180
12.0	0.974	0.880	12.0	0.970	0.484	2.186

Table 18. Spectral dependence for Lamb waves of laminate A_1 (asymmetrical modes)

f'	c'_g	f'	c'_g	f'	c'_g		
	A_0		A_1		A_2	A_3	SH_3
0.5	0.651	2.5	0.882	8.5	0.593	0.003	0.001
1.0	0.847	2.9	2.456	8.6	0.612	0.227	0.001
1.5	0.851	3.3	2.614	8.7	0.715	0.418	0.002
2.0	0.856	3.7	2.913	8.8	0.783	0.623	0.003
2.5	0.623	4.1	3.111	8.9	0.805	0.701	0.003
3.0	0.678	4.5	3.152	9.0	0.890	0.862	0.004
3.5	0.699	4.9	3.112	9.1	0.904	0.871	0.125
4.0	0.734	5.3	3.087	9.2	0.928	0.885	0.364
4.5	0.790	5.7	2.924	9.3	0.957	0.889	0.541
5.0	0.802	6.1	2.631	9.4	0.981	0.896	0.683
5.5	0.813	6.5	2.185	9.5	1.061	0.900	0.754
6.0	0.845	6.9	1.598	9.6	1.082	0.882	0.974
6.5	0.887	7.3	1.273	9.7	1.106	0.874	1.116
7.0	0.902	7.7	0.832	9.8	1.125	0.856	1.277
7.5	0.883	8.1	0.401	9.9	1.143	0.830	1.452
8.0	0.879	8.5	0.368	10.0	1.162	0.795	1.583
8.5	0.872	8.9	0.420	10.1	1.175	0.791	1.986
9.0	0.870	9.3	0.468	10.2	1.188	0.784	2.178
9.5	0.868	9.7	0.502	10.3	1.205	0.781	2.376
10.0	0.867	10.2	0.539	10.7	1.203	0.791	2.715
10.5	0.865	10.8	0.584	11.1	1.200	0.799	2.854
11.0	0.864	11.2	0.615	11.4	1.192	0.825	3.185
11.5	0.861	11.6	0.661	11.7	1.195	0.843	3.239
12.0	0.859	12.0	0.690	12.0	1.146	0.906	3.378

The dispersion curves of Lamb waves in two types of laminated composites A_1 and A_2 are presented in Tables 17 – 20. The results are given for five symmetric (Tables 17 and 19) and five antisymmetric (Tables 18 and 20) wave modes. All Lamb waves, with the exception of the fundamental modes (A_0, S_0 and SH_0), have cutoff frequencies. Note that the interaction of Lamb waves with delamination has been most studied in the low-frequency range, where only fundamental modes exist. The SH_0 and S_0 modes have low dispersion in the low-frequency range, below the frequency $xh/cT = 0.5$.

Table 19. Spectral dependence for Lamb waves of laminate A_2 (symmetrical modes)

f'	c'_g		f'	c'_g		
	S_0	SH_0		S_1	S_2	SH_2
0.5	3.042	1.803	5.0	1.527	0.041	0.005
1.0	3.005	1.752	5.3	1.743	0.097	0.214
1.5	2.910	1.685	5.6	1.832	1.184	0.679
2.0	2.805	1.599	5.9	1.801	0.811	1.112
2.5	2.609	1.485	6.2	1.709	0.913	1.563
3.0	2.308	1.361	6.5	1.687	1.099	1.952
3.5	1.814	1.224	6.8	1.564	1.286	2.037
4.0	0.726	1.100	7.1	1.500	1.485	2.206
4.5	0.437	0.895	7.4	1.301	1.701	2.311
5.0	0.948	0.556	7.7	1.238	1.715	2.318
5.5	0.925	0.611	8.0	1.105	1.723	2.325
6.0	0.911	0.674	8.3	1.098	1.668	2.305
6.5	0.918	0.701	8.6	0.984	1.600	2.297
7.0	0.926	0.725	8.9	0.851	1.449	2.184
7.5	0.931	0.761	9.2	0.826	1.417	2.137
8.0	0.937	0.792	9.5	0.794	1.284	2.000
8.5	0.940	0.803	9.8	0.762	1.208	1.915
9.0	0.945	0.805	10.1	0.731	1.142	1.806
9.5	0.950	0.810	10.4	0.702	1.051	1.585
10.0	0.954	0.815	10.8	0.701	0.984	1.658
10.5	0.955	0.822	11.1	0.700	0.972	1.901
11.0	0.956	0.829	11.4	0.702	0.900	1.052
11.5	0.958	0.830	11.7	0.703	0.899	0.935
12.0	0.960	0.842	12.0	0.704	0.898	0.854

It should be noted that the different frequency components within the wave packet propagate at almost the same speed. This fact is the reason why the wave packet retains its shape during its movement. In addition to this desirable feature, lower attenuation compared to waves for the A_0 wave mode and high sensitivity to delamination are two other reasons that have increased interest in the use of symmetric modes as diagnostic waves.

The symmetric mode S_0 is relatively weak in magnitude compared to the A_0, mode if the two modes are excited simultaneously. As a result, the mode of using the A_0 wave mode is preferable when diagnosing damage to the structure of composites.

Table 20. Spectral dependence for Lamb waves of laminate A_2 (asymmetrical modes)

f'	c'_g	f'	c'_g	f'	c'_g		
	A_0		A_1		A_2	A_3	SH_3
0.5	0.898	2.5	1.218	8.5	0.924	0.003	0.002
1.0	0.898	2.9	1.530	8.6	0.895	0.008	0.164
1.5	0.897	3.3	1.809	8.7	0.861	0.012	0.308
2.0	0.897	3.7	2.184	8.8	0.837	0.016	0.407
2.5	0.897	4.1	2.394	8.9	0.820	0.021	0.593
3.0	0.896	4.5	2.426	9.0	0.815	0.028	0.699
3.5	0.895	4.9	2.385	9.1	0.793	0.089	0.715
4.0	0.894	5.3	2.288	9.2	0.765	0.187	0.805
4.5	0.894	5.7	2.235	9.3	0.737	0.352	0.881
5.0	0.893	6.1	1.980	9.4	0.718	0.605	0.973
5.5	0.893	6.5	1.684	9.5	0.694	0.831	1.113
6.0	0.893	6.9	1.295	9.6	0.711	0.927	1.188
6.5	0.892	7.3	1.064	9.7	0.725	1.164	1.246
7.0	0.892	7.7	0.845	9.8	0.740	1.235	1.358
7.5	0.891	8.1	0.555	9.9	0.756	1.380	1.455
8.0	0.891	8.5	0.485	10.0	0.768	1.486	1.557
8.5	0.891	8.9	0.316	10.1	0.773	1.604	1.618
9.0	0.890	9.3	0.484	10.2	0.791	1.728	1.735
9.5	0.890	9.7	0.587	10.3	0.804	1.872	1.882
10.0	0.890	10.2	0.615	10.7	0.809	1.914	1.912
10.5	0.889	10.8	0.684	11.1	0.816	2.055	1.975
11.0	0.888	11.2	0.700	11.4	0.822	2.083	1.994
11.5	0.887	11.6	0.752	11.7	0.824	2.099	2.026
12.0	0.886	12.0	0.801	12.0	0.825	2.001	2.048

The calculation results indicate that the A_0 mode provides higher resolution than the S_0 and SH_0 modes. The reason for this is the fact that the wavelength of the A_0 mode is always shorter than that of the S_0 mode, especially in the low frequency range. In the higher frequency range, Lamb wave propagation in a relatively thick symmetrical corner laminate $(+45_6/-45_6)_s$ has a rather complex behavior.

The group velocity for the SH_0 and S_0 modes has a fairly high level of dispersion. In addition, targeted analysis showed that the symmetric mode dispersion in the quasi-isotropic laminate A_2 $(+45/-45/0/90)_s$ is significantly stronger. On the other

hand, the dispersion of the antisymmetric wave mode A_0 in both laminates is weaker beyond frequency $xh/cT = 1$.

The results of calculations of group velocity dispersion surfaces for wave modes in the laminar composites used make it possible to represent the polynomial dependence $c'_g = c'_g(f')$ in matrix form

$$c'_{g,i} = d_{ik}(f')^k,\ k = 0,1,...,5,\ i \in \left(S_{0,A_1}, S_{0,A_2}, SH_{0,A_1}, SH_{0,A_2}\right) \quad (6.47)$$

$$d_{ik} = \begin{pmatrix} 0.076 & -0.631 & 1.467 & -1.514 & 3.798 \\ -0.009 & 0.182 & -1.096 & 1.813 & 2.264 \\ -0.004 & 0.092 & -0.637 & 1.231 & 1.759 \\ -0.002 & 0.047 & -0.307 & 0.469 & 1.584 \end{pmatrix}. \quad (6.48)$$

AFTERWORD

The kinetics of surface and volume localization of deformation of laminar composite structures can be studied using various wavelet analysis techniques. In particular, the results of the use of acoustic emission for wavelet analysis of laminar composites, the use of the zero-order energy moment of a pulse load to identify damage, Haar wavelet methods, the distribution of potential deformation fields under continuous wavelet transformations, as well as the kinetics of Lamb wave propagation in isotropic composite structures.

Analysis of the pulsed effect of acoustic emission on samples of carbon fiber composites with fiber filling made it possible to determine the spectral distribution of average energy, average entropy, and energy coefficient. Estimates of both the critical values of threshold values for choosing the maximum and minimum parameters “threshold max” and “threshold min” and the distribution density of wavelets in the min-max band were obtained. It should be noted that a significant number of wavelets were recorded outside the threshold values, in particular Haar- and Daubechies- wavelets. Preference analysis indicates different types of wavelets for distributions according to the specified types of parameters: Haar- and Daubechies- wavelets for *H* - distribution, Daubechies- and Dmeyers- wavelets for *E* - distribution and only Dmeyers-wavelet for η – distribution. The result of the final preferences for the min-max parameter indicates the Daubechies-wavelet.

However, the specified restriction on the choice of wavelet types is not absolutely strict and final, since, for example, the first element in the chain of ranking the distribution of wavelets within threshold values is the η-parameter. Consequently, decomposition with respect to the η-parameter can be carried out using, in particular, the Haar-wavelet. In addition, a separate study on the relative amount of spectral energy for different types of acoustic signals favors coif5- and dmey-wavelets.

Difficulties in determining local deformations in two-component laminar composites by analytical methods indicate the need to study the moduli and direction of wave propagation in composite samples. The work carried out an analysis of the first acoustic mode, which includes information on transverse deflection, phase and group velocities. The critical values of the relative frequencies at which the phase velocity reaches saturation are obtained.

Features of the spectral distribution of the applied load for plates made of a two-component composite indicate a decrease in the arrival time with increasing frequency due to an increase in group velocities. The results obtained can be used for both isotropic and anisotropic composites.

The work evaluates the influence of noise on the arrival time of signals. The spread of directions in which group velocities change complicates the numerical analysis procedure. Therefore, to solve the problem, calculated group velocities from the dispersion relations of wave propagation are used. It was found that the

presence of noise up to 2% and 5% does not have a significant effect on either the spatial distribution of the applied load or the spectral distribution of the arrival time of noisy signals.

A significant variation in the directions of group velocities causes an increase in the probability of errors occurring during numerical analysis. One of the options for overcoming these difficulties may be the use of calculated group velocities obtained from the dispersion relations of wave propagation.

Numerical evaluations based on the presence of the influence of geometric parameters of composite samples, the direction of reinforced inclusions on the free vibration of inversely bonded composite laminated shells, allowed us to identify trends in the spectral distribution for composite spherical, elliptical and cylindrical shells. The possibility of imposing generalized boundary conditions on inversely coupled laminated composites when studying free vibrations inside their volume has been discovered. In particular, in order to interface with the Haar wavelet integral constant, a boundary condition was added to the control function of the main system.

It is shown that the nature of the connections in the composite shell structure, as well as the type of boundary conditions, significantly affect the frequency within volumetric vibrations only when a fixed threshold value is exceeded. Characteristic numerical intervals of relative changes in dimensionless frequencies of three- and four-layer shells are determined for all types of boundary conditions.

The dependence of the damage index vector of the composite plate on the relative delamination area is analyzed in detail. Variations in multiple values of the damage index vector are associated with the presence of a delamination zone in composite plates. It is shown that the results of wavelet analysis of damaged composites make it possible to detect delamination areas of less than 1%.

It was found that only the fundamental modes for Lamb waves in laminated composites do not have cutoff frequencies. On the other hand, only the presence of fundamental modes in the low-frequency range makes it possible to analyze the correlation of Lamb waves with the location of delamination volumes. Low attenuation, as well as high sensitivity to stratification, are the reasons that have increased interest in the use of the symmetric A_0 mode as a diagnostic wave. It should be noted that the preferred choice of mode types is difficult for the high-frequency range of thick laminated composites, in which the propagation of Lamb waves has complex behavior.

The calculation results indicate a high level of group velocity dispersion for the symmetric modes SH_0 and S_0. In addition, a cutoff frequency was discovered, above which the dispersion of the antisymmetric wave mode A0 becomes significantly weaker. The results of wavelet analysis made it possible to present the dispersion dependences of the group velocity for symmetric and antisymmetric wave modes in polynomial form.

REFERENCES

1. Grossman A. and Morlet J. (1984) Decomposition of Hardy Functions into Square Integrable Wavelets of Constant Shape. *SIAM Journal on Mathematical Analysis*, 15, 723-736.
2. Meyer Y. “Wavelets and Operators”, *Cambridge Studies in Advanced Mathematics* v. 37, Cambridge University Press, Cambridge, England, 1992.
3. Daubechies I. (1990) The Wavelet transform time-frequency localization and signal analysis. *IEEE Transactions on Information Technology*, 36(5), 961-1005.
4. Mallat S.G. A theory for multiresolution signal decomposition: The wavelet representation. *IEEE Trans. Pattern Anal. Mach. Intell*. 1989, 11, 674-693.
5. Haar A. Zur Theorie der orthogonalen Functionsysteme, Dissertation (Gottingen, 1909); *Mathematische Annalen*, 69 (1910), 331—371, 71 (1912), 33-53.
6. Ferreira A.J.M., Castro L.M.S. and Bertoluzza S. A high order collocation method for the static and vibration analysis of composite plates using a first-order theory. *Composite structures*, 89, 424-432.
7. Castro L.M.S., Ferreira A.J.M., Bertoluzza S., Batra R.C. and Reddy J.N. A wavelet collocation method for the static analysis of sandwich plates using a layerwise theory. *Composite Structures*, 92, 1786-1792.
8. Rahimkhani P, Ordokhami Y. and Lima P.M. An improved composite collocation method for distributed-order fractional differential equations based on fractional Chelyshkov wavelets. *Applied Numerical Mathematics*, 145, 1-27.
9. Nastos C.V. and Saravanos D.A. A finite wavelet domain method for wave propagation analysis in thick laminated composite and sandwich plates. *Wave Motion*, 95, 102543.
10. Zuo H., Chen Y. and Jia F. (2020) A new C0 layerwise wavelet finite element formulation for the static and free vibration analysis of composite plates. *Composite Structures*, 254, 112852.
11. Khalili A., Jha R. and Samaratunga D. (2017) The Wavelet Spectral Finite Element-based user-defined element in Abaqus for wave propagation in one-dimensional composite structures. *Simulation: Transactions of the Society for Modeling and Simulation International*, 93(5), 397-408.
12. Zuo H. et al. (2021) Unified wavelet finite element formulation for static and vibration analysis of laminated composite shells. *Composite Structures*, 272, 114207.
13. Samaratunga D., Jha R. and Gopalakrishnan S. (2014) Wave propagation analysis in laminated composite plates with transverse cracks using the wavelet spectral finite element method. *Finite Elements in Analysis and Design*, 89, 19-32.

14. Mitra M., Gopalakrishnan S. (2006) Wavelet based spectral finite element for analysis of coupled wave propagation in higher order composite beams. *Composite Structures*, 73, 263-277.
15. Mitra M., Gopalakrishnan S. (2006) Wavelet based spectral finite element modelling and detection of de-lamination in composite beams. *Proceedings of the Royal Society Part A*, 462, 1721-1740.
16. Samaratunga D., Jha R. and Gopalakrishnan S. (2016) Wavelet spectral finite element for modeling guided wave propagation and damage detection in stiffened composite panels. *Structural Health Monitoring*, 15(3), 317-334.
17. Samaratunga D., Jha R. and Gopalakrishnan S. (2014) Wavelet spectral finite element for wave propagation in shear deformable laminated composite plates. *Composite Structures*, 108, 341-353.
18. Samaratunga D., Jha R. (2015) Wavelet spectral finite element modeling for wave propagation in adhesively bonded composite joints. *23rd AIAA/AHS Adaptive Structures Conference*, 10.2514/6.2015-1727.
19. Kamiński M.M. (2002) Wavelet-Based Finite Element Elastodynamic Analysis of Composite Beams. *5th World Congress on Computational Mechanics. WCCM V-At*: Vienna, Austria, July 7-12, 2002, 1-10.
20. Писаренко А.Н., Максименюк Я.А., Загинайло И.В. Математическое моделирование нестационарного температурного поля с учетом влагосодержания в строительных материалах. *Вісник Одеської державної академії будівництва та архітектури*. - Одеса: ОДАБА, 2015. - Вип. 57. С. 347-355.
21. Писаренко О.М., Вілінська Л.М. Моделювання нестаціонарного температурного поля з урахуванням наявності вологи в будівельних матеріалах //*Збірник наукових праць. Серія: галузеве машинобудування, будівництво*. - Полтава: ПолтНТУ, 2016. - Вип. 2 (47). С. 198-205.
22. Zaginaylo I.V., Maksimeniuk Ya.A. and Pysarenko A.N. (2017) Two-Dimensional Numerical Simulation Study of the Effective Thermal Conductivity Statistics for Binary Composite Materials. *International Journal of Heat and Technology*, 35, 2, 364 - 370.
23. Pysarenko A. and Zaginaylo I. (2021) Influence of matrix-filler thermal conductivity on macro heat transfer in two-component composites. SSDCMS 2021, *IOP Conf. Series*: *Materials Science and Engineering*, 1162, 012013.
24. Pysarenko A. and Zaginaylo I. (2019) Numerical Simulation of the Heat Conductivity of Randomly Inhomogeneous Two-Dimensional Composite Material. Hauppage, New York: Nova Science Publisher's Inc., 176.
25. Pysarenko A. N. Wavelet transform for polymer composites. *Збірник тез міжнародної науково-технічної конференції "Структуроутворення*

та руйнування композиційних будівельних матеріалів та конструкцій". Одеса: ОДАБА, 2023. С. 116-119.

26. Dong H. et al. (2022) A Mixed Wavelet-Learning Method of Predicting Macroscopic Effective Heat Transfer Conductivities of Braided Composite Materials. *Communication in Computational Physics*, 31(2), 593-625.
27. Zauner G, Mayr G. and Hendorfer G. (2006) Application of wavelet analysis in active thermography for non-destructive testing of CFRP composites. *Proceedings of SPIE*. *The International Society for Optical Engineering*. 6383.
28. Hayashi T., Wakayama S. (2008) Bending fracture behavior of 3D -woven SiCSiC composites with transpiration cooling structure characterized by ae wavelet analysis. *Journal of Acoustic Emission*, 26, 160-171.
29. Rashidi M.M., Erfani E. (2009) New analytical method for solving Burgers' and nonlinear heat transfer equations and comparison with HAM. *Computer Physics Communications*, 180, 1539-1544.
30. Dong H. et al. (2021) A wavelet-based learning approach assisted multiscale analysis for estimating the effective thermal conductivities of particulate composites. *Computer Methods in Applied Mechanics and Engineering*, 374, 113591.
31. Liu W., Yang X. and Jinxing S. (2020) An Integrated Fault Identification Approach for Rolling Bearings Based on Dual-Tree Complex Wavelet Packet Transform and Generalized Composite Multiscale Amplitude-Aware. *Shock and Vibration*, 8851310.
32. Zheng J. et. al. (2019) An ImprovedEmpirical Wavelet Transform and Refined Composite Multiscale Dispersion Entropy Based Fault Diagnosis Method for Rolling Bearing. *IEEE Access*, 2940627.
33. Cheng Y. et al. (2022) Battery State of Charge Estimation Based on Composite Multiscale Wavelet Transform. *Energies*, 15, 2064.
34. Baccar D. and Söffker D. (2017) Identification and classification of failure modes in laminated composites by using a multivariate statistical analysis of wavelet coefficients. *Mechanical Systems and Signal Processing*, 96, 77-87.
35. Denis L. et al. (2010) Scalable Intraband and Composite Wavelet-Based Coding of Semiregular Meshes. *IEEE Transactions on Multimedia*, 12 (8), 773-789.
36. Kamiński M. (2003) Wavelet-based homogenization of unidirectional multiscale composites. *Computational Materials Science*, 27, 446-460.
37. Sezer S. and Aliev I.A. (2010) A new characterization of the Riesz potential spaces with the aid of a composite wavelet transform. *Journal of Mathematical Analysis and Applications*, 372 (2), 549-558.
38. Chapa J. and Rao R.M. (2000) Algorithms for Designing Wavelets to Match a Specified Signal. *IEEE Transactions on Signal Processing*, 48 (12), 3395-3406.

39. Jeon J.Y. et Al. (2020) 2D-wavelet wavenumber filtering for structural damage detection using full steady-state wavefield laser scanning. *NDT and E International*, 116, 102343.
40. Kharrat M., Ramasso E., Placet V., Boubakar M.L. (2016) A signal processing approach for enhanced Acoustic Emission data analysis in high activity systems: Application to organic matrix composites. *Mechanic Systems and Sygnal Processing*, 70-71, 1038-1055.
41. Velayudham A., Krishnamurthy R., Soundarapandian T. (2005) Acoustic emission based drill condition monitoring during drilling of glassphenolic polymeric composite using wavelet packet transform. *Materials Science and Engineering A*, 412, 141-145.
42. Wang X. et al. (2015) Acoustic emission detection for mass fractions of materials based on wavelet packet technology. *Ultrasonics*, 60, 27-32.
43. Heidary et al. Acoustic emission signal analysis by wavelet method to investigate damage mechanisms during drilling of composite materials. *Proceedings of the ASME 2010 10th Biennial Conference on Engineering Systems Design and Analysis ESDA2010 July 12-14, 2010, Istanbul, Turkey*, 409-416.
44. Bak M., KalaiChalvan K., Vijayaraghavan and Sridhar BTN. (2013) Acoustic emission wavelet transform on adhesively bonded single-lap joints of composite laminate during tensile test. *Journal of Reinforced Plastics and Composites*, 32(2), 87-95.
45. Adamczak-Bugno A. (2019) Assessment of Destruction Processes in Fibre Cement Composites Using the Acoustic Emission Method and Wavelet Analysis. *IOP Conference Series: Materials Science and Engineering*, 471, 032042.
46. Meyer E., Tuthill T. (1995) Bayesian classification of ultrasound signals using wavelet coefficients. *IEEE Natl. Aerospace and Electronics Conf. (NAECON)*, 1, 240-243.
47. Beheshtizadeh N., Mostafapour A. (2016) Characterization of carbon fiberepoxy composite damage by acoustic emission using FFT and Wavelet analysis. *Advanced Engineering Forum* 17:77-88.
48. Qiao S. et al. (2023) Cluster analysis on damage pattern recognition in carbonepoxy composites using acoustic emission wavelet packet. *Journal of Reinforced Plastics and Composites*, 42(19-20), 1006-1021.
49. Mohammadi R. et al. (2017) Correlation of acoustic emission with finite element predicted damages in open-hole tensile laminated composites. *Composites Part B*: *Engineering*, 108, 427-435.
50. Loutas T.H., Kostopoulos V., Ramirez-Jimenez C. and Pharaon M. (2006) Damage evolution in center-holed glasspolyester composites under quasi-static loading using timefrequency analysis of acoustic emission monitored waveforms. *Composites Science and Technology*, 66, 1366-1375.

51. Qi G., Bathorst A., Hashemi J. and Kamala G. (1977) Discrete wavelet decomposition of acoustic emission signals from carbon-fiber-reinforced composites. *Composites Science and Technology*, 57, 389-403.
52. Kamala G., Hashemi J. and Barhorst A.A. (2001) Discrete-Wavelet Analysis of Acoustic Emissions During Fatigue Loading of Carbon Fiber Reinforced Composites. *Journal of Reinforced Plastics and Composites*, 20(3), 222-238.
53. Dunegan H.L., Harris D.O. and Tatro C.A. (1968) Fracture analysis by use of acoustic emission. *Engineering Fracture Mechanics*, 1, 105-122.
54. Ghoshal A. et. al. (2007) Health Monitoring of Composite Plates using Acoustic Wave Propagation, Continuous Sensors and Wavelet Analysis. *Journal of Reinforced Plastics and Composites*, 26, 95-112.
55. Tiwari K.A., Raisutis R. and Samaitis V. (2017) Hybrid Signal Processing Technique to Improve the Defect Estimation in Ultrasonic Non-Destructive Testing of Composite Structures. *Sensors (Basel)*, 17(12), 1-21.
56. Stankevych O., Skalskyi V., Klym B. and Velykyi P. (2022) Identification of fracture mechanisms in cementitious composites using wavelet transform of acoustic emission signals. *Procedia Structural Integrity*, 36, 114-121.
57. Thomas J.-H. (2008) Investigation of damage mechanisms of composite materials multivariable analysis based on temporal and wsvelet features extracted from acoustic emission signals. *Journal of the Acoustical Society of America*, 123(5): 3082.
58. Barile C. et al. (2022) Acoustic emission waveforms for damage monitoring in composite materials: Shifting in spectral density, entropy and wavelet packet transform. *Structural Health Monitoring*, 21 (4), 1768-1789.
59. Fotouhi M. et al. (2015) Investigation of the damage mechanisms for mode I delamination growth in foam core sandwich composites using acoustic emission. *Structural Health Monitoring*, 14(3), 265-280.
60. Sung D.-U., Kim C.-G. and Hong C.-S. (2002) Monitoring of impact damages in composite laminates using wavelet transform. *Composites Part B*, 33, 35-43.
61. Gang Q. (1997) On predicting the fracture behavior of CFR and GFR composites using wavelet-based AE techniques. *Engineering Fracture Mechanics*, 58(4), 363-385.
62. Loutas T.H., Sotiriades G. and Kostopoulos V. (2004) On the application of wavelet transform of AE signals from composite materials. *Conference: European Working Group on Acoustic Emission, Berlin, Germany*, 42, 433-445.
63. Beheshtizaeh N., Mostafapour A. (2017) Processing of acoustic signals via wavelet & Choi - Williams analysis in three-point bending load of carbon/epoxy and glass/epoxy composites. *Ultrasonics*, 79, 1-8.

64. Legendre S., Goyette J. and Massicotte D. (2001) Ultrasonic NDE of composite material structures using wavelet coefficients. *NDT&E International*, 34, 31-37.
65. Chengqiang G., Hangong W. and Nenjiun Y. (2010) Ultrasonic Testing System of Fiber-Reinforced Composites and Wavelet-Based Echo Signal *Processing. Engineering, Materials Science. Third International Conference on Information and Computing*, 4 June 2010, 2, 293-296.
66. Oskouei A.R., Ahmadi M. (2008) Using wavelet transform to locate acoustic emission source in composite plate with one sensor. *Journal of the Acoustic Society of America*, 123(5), 2212-2215.
67. Świt G., Adamczak A. and Krampikowska A. (2017) Wavelet Analysis of Acoustic Emissions during Tensile Test of Carbon Fibre Reinforced Polymer Composites. *IOP Conference Series: Materials Science and Engineering*, 245(2), 022031.
68. Ni Q.-Q., Iwamoto M. (2002) Wavelet transform of acoustic emission signals in failure of model composites. *Engineering Fracture Mechanics*, 69, 717-728.
69. Muñoz C.Q.G., Jiménez A.A. and Márquez F.P.G. (2018) Wavelet transforms and pattern recognition on ultrasonic guides waves for frozen surface state diagnosis. *Renewable Energy*, 116(B), 42-54.
70. Oskouei A.R., Ahmadi M. and Hajikhani M. (2009) Wavelet-based acoustic emission characterization of damage mechanism in composite materials under mode I delamination at different interfaces. *eXPRESS Polymer Letters*, 3(12), 804-813.
71. Heidary H., Ahmadi M., Rahimi A. and Minak G. (2012) Wavelet-based acoustic emission characterization of residual strength of drilled composite materials. *Journal of Composite Materials*, 47(23), 2897-2908.
72. Qi G. (2000) Wavelet-based AE characterization of composite materials. *NDT&E International*, 33, 133-144.
73. Su Zh., Ye L and Bu X. (2002) A damage identification technique for CFEP composite laminates using distributed piezoelectric transducers. *Composite Structures*, 57, 465-471.
74. Ghasemi-Ghalebahman A., Ashory M.-R. and Kokabi M.-J. (2018) A proper lifting scheme wavelet transform for vibration-based damage identification in composite laminates. *Journal of Thermoplastic Composite Materials*, 31(5), 668-688.
75. Karimi N.Z., Minak G. and Kianfar P. (2015) Analysis of damage mechanisms in drilling of composite materials by acoustic emission. *Composite Structures*, 131, 107-114.
76. Fotouhi M., Sadeghi S., Jalalvand M. and Ahmadi M. (2017) Analysis of the damage mechanisms in mixed-mode delamination of laminated

composites using acoustic emission data clustering. *Journal of Thermoplastic Composite Materials*, 30(3), 318-340.

77. Wronkowicz-Katunin A., Katunin A., Nagode A. and Klemenc J. Classification of Cracks in Composite Structures Subjected to Low-Velocity Impact Using Distribution-Based Segmentation and Wavelet Analysis of X-ray Tomograms. *Sensors*, 21(24), 10.3390/s21248342.
78. Liu Y., Li Zh. and Zhang W. (2010) Crack detection of fibre reinforced composite beams based on continuous wavelet transform. *Nondestructive Testing and Evaluation*, 25(1), 25-44.
79. Staszewski W.J., Pierce S.G., Worden K. and Culshaw B. (1999) Cross-wavelet analysis for lamb wave damage detection in composite materials using optical fibres. *Key Engineering Materials*, 167-168, 373-380.
80. Katunin A., Przystałka P. (2014) Damage assessment in composite plates using fractional wavelet transform of modal shapes with optimized selection of spatial wavelets. *Engineering Applications of Artificial Intelligence*, 30, 73-85.
81. Barile K. et al. (2019) Damage characterization in composite materials using acoustic emission signal-based and parameter-based data. *Composites Part B*, 178, 107469.
82. Khamedi R. et al. (2019) Damage characterization of carbon/epoxy composites using acoustic emission signals wavelet analysis. *Composite Interfeces*, 27(1), 1-14.
83. Marec A., Thomas J.-H. and Guerjouma R.El. (2008) Damage characterization of polymer-based composite materials Multivariable analysis and wavelet transform for clustering acoustic emission data. *Mechanical Systems and Signal Processing*, 22, 1441-1464.
84. Kessler S.S., Spearing S.M. and Soutis C. (2002) Damage detection in composite materials using Lamb wave methods. *Smart Materials and Structures*, 11, 269-278.
85. Sohn H., Park H.W., Law K.H. and Farrar C.R. (2007) Damage Detection in Composite Plates by Using an Enhanced Time Reversal Method. *Journal of Aerospace Engineering*, 20(3), 141-151.
86. Ashory M.-R., Ghasemi-Ghalebahman A. and Kokabi M.-J. (2016) Damage detection in laminated composite plates via an optimal wavelet selection criterion. *Journal of Reinforced Plastics and Composites*, 35(24), 1761-1775.
87. Cao M., Qiao P. (2008) Damage detection of laminated composite beams with progressive wavelet transforms. *Procceeding of SPIE*. *The International Society for Optical Engineering* 693402.
88. Chrysafi A.P., Athanasopoulos N. and Siakavellas N.J. (2017) Damage detection on composite materials with active thermography and digital image processing. *Intrnational Journal of Thermal Sciences*, 116, 242-253.

89. Ashory M.-R., Ghasemi-Ghalebahman A. and Kokabi M.-J. (2018) Damage identification in composite laminates using a hybrid method with wavelet transform and finite element model updating. *Proceedings of the Institution of Mechanical Engineers, Part C: Journal of Mechanical Engineering Science*, 232(5), 815-827.
90. Katunin A. (2011) Damage identification in composite plates using two-dimensional B-spline wavelets. *Mechanical Systems and Signal Processing*, 25, 3153-3167.
91. Janeliukstis R. et al. (2016) Damage Identification in Polymer Composite Beams Based on Spatial Continuous Wavelet Transform. *IOP Conference Series: Material Science and Engineering*, 111, 012005.
92. Zhou J., Li Z. and Chen J. (2018) Damage identification method based on continuous wavelet transform and mode shapes for composite laminates with cutouts. *Composite Structures*, 191, 12-23.
93. Azuara G., Ruiz M. and Barrera E. (2021) Damage Localization in Composite Plates Using Wavelet Transform and 2-D Convolutional Neural Networks. *Sensors*, 21(17), s21175825.
94. Zumpano G., Meo M. (2008) Damage localization using transient non-linear elastic wave spectroscopy on composite structures. *International Journal of Non-Linear Mechanics*, 43, 217-230.
95. Molchanov D., Safin A and Luhyna N. (2016) Damage monitoring of aircraft structures made of composite materials using wavelet transforms. *IOP Conference Series: Materials Science and Engineering*, 153, 012016.
96. Katunin A. (2010) Identification of multiple cracks in composite beams using discrete wavelet transform. *Scientific Problems of Machines Operation and Maintenance*, 2(162), 41-52.
97. Salehian A. Identifying the Location of a Sudden Damage in Composite Laminates Using Wavelet Approach. *Masters Theses Worcester Polytechnic Institute*, 2003.
98. Yu W., Shenfang Y. and Lei Q. (2011) Improved Wavelet-based Spatial Filter of Damage Imaging Method on Composite Structures. *Chinese Journal of Aeronautics*, 24, 665-672.
99. Méndez A. et al. (2015) Micromorphological Characterization of Zinc/Silver Particle Composite Coatings. *Microscopy Research and Technique*, 78, 1082-1089.
100. Gallego A., Moreno-García P. and Casanova C.F. (2013) Modal analysis of delaminated composite plates using the finite element method and damage detection via combined Ritz/2D-wavelet analysis. *Journal of Sound and Vibration*, 332, 2971-2983.
101. Katunin A. (2013) Modal-Based Non-Destructive Damage Assessment in Composite Structures Using Wavelet Analysis: A Review. *International Journal of Composite Materials*, 3(6B), 1-9.

102. Sha G. et al. (2020) Multiple damage detection in laminated composite beams by data fusion of Teager energy operator-wavelet transform mode shapes. *Composite Structures*, 235, 111798.
103. Katunin A. (2015) Nondestructive Damage Assessment of Composite Structures Based on Wavelet Analysis of Modal Curvatures: State-of-the-Art Review and Description of Wavelet-Based Damage Assessment Benchmark. *Shock and Vibration*, (735219):1-19.
104. Spagnoli A., Montanari L., Basu B. and Broderick B. (2014) Nonlinear damage identification in fiber-reinforced cracked composite beams through time-space wavelet analysis. *Procedia Materials Science*, 3, 1579-1584.
105. Yan Y.J., Yam L.H. (2002) Online detection of crack damage in composite plates using embedded piezoelectric actuatorssensors and wavelet analysis. *Composite Structures*, 58, 29-38.
106. Gerasimov V., Khandetsky V. and Gnoevoy S. (2006) Research of probability characteristics in defect detection of composite materials using wavelet transform. *International Journal of Materials and Product Technology*, 27(3/4), 210-220.
107. Gomes G.F. et al. (2018) The use of intelligent computational tools for damage detection and identification with an emphasis on composites - A Review. *Composite Structures*, 196, 44-54.
108. Yam L.H., Yan Y.J. and Jiang J.S. (2003) Vibration-based damage detection for composite structures using wavelet transform and neural network identification. *Composite Structures*, 60, 403-412.
109. Katunin A. (2014) Vibration-based spatial damage identification in honeycomb-core sandwich composite structures using wavelet analysis. *Composite Structures*, 118, 385-391.
110. Bayissa W.L., Haritos N. and Thelandersson S. (2008) Vibration-based structural damage identification using wavelet transform. *Mechanical Systems and Signal Processing*, 22, 1194-1215.
111. Yan G., Zhou L.L. and Yuan F.G. (2005) Wavelet-based built-in damage detection and identification for composites. *Conference: Smart structures and materials 2005: sensors and smart structures technologies for civil, mechanical, and aerospace systems*, SPIE, 5765, 324-334.
112. Katunin A., Kostka P. (2014) Characterisation of impact damage of composite structures using wavelet-based fusion of ultrasonic and optical images. *Advanced Composites Letters*, 23(5), 123-130.
113. Kumar M., Pandit S. (2014) A composite numerical scheme for the numerical simulation of coupled Burgers' equation. *Computer Physics Communications*, 185, 809-817.

114. Kim K. et al. (2021) Application of Haar wavelet discretization method for free vibration analysis of inversely coupled composite laminated shells. *International Journal of Mechanical Sciences*, 204, 106549.
115. Majak J. et al. (2015) Convergence theorem for the Haar wavelet based discretization method. *Composite Structures*, 126, 227-232.
116. Xie X. et al. (2014) Free vibration analysis of composite laminated cylindrical shells using the Haar wavelet method. *Composite Structures*, 109, 169-177.
117. So S.-R. et al. (2021) Haar wavelet discretization method for free vibration study of laminated composite beam under generalized boundary conditions. *Journal of Ocean Engineering and Science*, 6(1), 1-11.
118. Fan J., Huang J. (2018) Haar Wavelet Method for Nonlinear Vibration of Functionally Graded CNT-Reinforced Composite Beams Resting on Nonlinear Elastic Foundations in Thermal Environment. *Shock and Vibration*, 9597541.
119. Majak J. et al. (2018) New Higher Order Haar Wavelet Method Application to FGM Structures. *Composite Structures*, 201, 72-78.
120. Majak J. et al. (2015) On the Accuracy of the Haar Wavelet Discretization Method. *Composites Part B: Engineering*, 80, 321-327.
121. Dai Q., Qin Z. and Chu F. (2021) Parametric study of damping characteristics of rotating laminated composite cylindrical shells using Haar wavelets. *Thin-Walled Structures*, 161, 107500.
122. Chui C.K., Han N. (2021) Wavelet thresholding for recovery of active sub-signals of a composite signal from its discrete samples. *Applied and Computational Harmonic Analysis*, 52, 1-24.
123. Jeong H. (2001) Analysis of plate wave propagation in anisotropic laminates using a wavelet transform. *NDT&E International*, 34, 185-190.
124. Yahiaoui A., Med M.S.C. and Laddada S. (2016) Analysis of the composite materials using the wavelet transforms. *Journal of Scientific & Industrial Research*, 75, 344-348.
125. Ülker-Kaustell M., Karoumi R. (2011) Application of the continuous wavelet transform on the free vibrations of a steel–concrete composite railway bridge. *Engineering Structures*, 33, 911-919.
126. Eremenko V., Zaporozhets A. (2019) Application of Wavelet Transform for Determining Diagnostic Signs. *Proceedings of the 15th International Conference on ICT in Education, Research and Industrial Applications. Integration, Harmonization and Knowledge Transfer*. Volume I: Main Conference, Kherson, Ukraine, June 12-15, 2019, 20190202.
127. Altabey W.A. (2021) Applying deep learning and wavelet transform for predicting the vibration behavior in variable thickness skew composite plates with intermediate elastic support. *Journal of Vibroengineering*, 23(4), 770-783.

128. Nam K.W. (2006) Bending strength of Si_3N_4 monolithic and Si_3N_4/SiC composite ceramics and elastic wave characteristics by wavelet analysis. *International Journal of Modern Physics B*, 20(25, 26 & 27), 4279-4284.
129. Fotouhi M. Heidary H., Ahmadi M. and Pashmforoush F. (2012) Characterization of composite materials damage under quasi-static three-point bending test using wavelet and fuzzy C-means clustering. *Journal of Composite Materials*, 46(15), 1795-1808.
130. Fedi M., Cascone L. (2011) Composite continuous wavelet transform of potential fields with different choices of analyzing wavelets. *Journal of Geophysical Research: Solid Earth*, 116(7), B07104.
131. Huybrechs D., Vandewalle S. (2005) Composite quadrature formulae for the approximation of wavelet coefficients of piecewise smooth and singular functions. *Journal of Computational and Applied Mathemanics*, 180, 119-135.
132. Dahmen W., Schneider R. (1999) Composite wavelet bases for operator equations. *Mathematics of Computation*, 68(228), 1533-1567.
133. Stevenson R. (2007) Composite wavelet bases with extended stability and cancellation properties. *SIAM Journal on Numerical Analysis*, 45(1), 133-162.
134. Aliev I.A. et al. (2007) Composite Wavelet Transforms Applications and Perspectives. *eprint arXIV*:0711.1424v1.
135. Katunin A., Przystałka P. (2014) Damage assessment in composite plates using fractional wavelet transform of modal shapes with optimized selection of spatial wavelets. *Engineering Applications of Artificial Intelligence*, 30, 73-85.
136. Su C. et al. (2020) Damage assessments of composite under the environment with strong noise based on synchrosqueezing wavelet transform and stack autoencoder algorithm. *Measurement*, 156, 107587.
137. Bhattacharjee A., Nanda B.K. (2018) Damping study of composites using wavelet analysis. *Journal of Vibration and Control*, 24(21), 5141-5151.
138. Yang C., Qyadiji O. (2017) Delamination detection in composite laminate plates using 2D wavelet analysis of modal frequency surface. *Computers and Structures*, 179, 109-126.
139. Gu H., Song G. and Qiao P. (2004) Delamination Detection of Composite Plates Using Piezoceramic Patches and Wavelet Packet Analysis. *Proceedings of SPIE*, 5393, 0277-786X/04, 220-230.
140. Rautela M. et al. (202) Delamination prediction in composite panels using unsupervised-feature learning methods with wavelet-enhanced guided wave representations. *Composite Structures*, 291, 115579.
141. Jiang T. et al. (2017) Detection of Debonding between Fiber Reinforced Polymer Bar and Concrete Structure Using Piezoceramic Transducers and Wavelet Packet Analysis. *IEEE Sensors Journal*, 17, 1992-1998.

142. Yan Y.J., Yam L.H. (2004) Detection of delamination damage in composite plates using energy spectrum of structural dynamic responses decomposed by wavelet analysis. *Computers and Structures*, 82, 347-358.
143. Jang B.-W. et al. (2012) Detection of impact damage in composite structures using high speed FBG interrogator. *Advanced Composite Materials*, 21, 29-44.
144. Wei Z., Yam L.H. and Cheng L. (2004) Detection of internal delamination in multi-layer composites using wavelet packets combined with modal parameter analysis. *Composite Structures*, 64, 377-387.
145. Farahani S.D., Sefidgar M. and Kowsary F. (2011) Estimation of kinetic parameters of composite materials during the cure process by using wavelet transform and mollification method. *International Communications in Heat and Mass Transfer*, 38, 1305-1311.
146. Kim K.-B., Hsu D.K. Barnard D.J. (2013) Estimation of porosity content of composite materials by applying discrete wavelet transform to ultrasonic backscattered signal. *NDT&E International*, 56, 10-16.
147. Velayudham A., Krishnamurthy R. and Soundarapandian T. (2005) Evaluation of drilling characteristics of high volume fraction fibre glass reinforced polymeric composite. *International Journal of Machine Tools & Manufacture*, 45, 399-406.
148. Janeliukstis R. et al. (2017) Experimental structural damage localization in beam structure using spatial continuous wavelet transform and mode shape curvature methods. *Measurement*, 102, 253-270.
149. Ferreira D.B.B et al. (2004) Failure mechanism characterisation in composite materials using spectral analysis and the wavelet transform of acoustic emission signals. *Insight*, 46(5), 282-289.
150. Saponara V. et al. (2011) Fatigue damage identification in composite structures through ultrasonics and wavelet transform signal processing. *Review of Progress in Quantitative Nondestructive Evaluation*, 30, 927-934.
151. Dinç E., Baleanu D. (2010) Fractional wavelet transform for the quantitative spectral resolution of the composite signals of the active compounds in a two-component mixture. *Computers and Mathematics with Applications*, 59, 1701-1708.
152. Wu Y.-J., Shi X.-Z. and Zhuang T.G. (2000) Fusion of Wavelet Packets and Neural Network in Detection of Composites. *AIAA Journal*, 38(6), 1063-1069.
153. Zhang Z. et al. (2019) Gearbox Composite Fault Diagnosis Method Based on Minimum Entropy Deconvolution and Improved Dual-Tree Complex Wavelet Transform. *Entropy*, 21(18), e211010018.
154. Scalea F.L. et al. (2007) Health Monitoring of UAV Wing Skin-to-spar Joints using Guided Waves and Macro Fiber Composite Transducers. *Journal of Intelligent Material Systems and Structures*, 18, 373-388.

155. Zhou Y. (2018) High-precision terahertz frequency modulated continuous wave imaging method using continuous wavelet transform. *Optical Engineering*, 57(02), 023108.
156. Rajendran P, Srinivasan S.M. (2016) Identification of Added Mass in the Composite Plate Structure Based on Wavelet Packet Transform. *Strain*, 52, 14-25.
157. Ayari F., Amar C.B. (2015) Image de-noising of a metal matrix composite microstructure using sure-let wavelet and weighted bilateral filter. *11th International Conference on Information Assurance and Security* (*IAS*), *Marrakech, Morocco*, 2015, 146-151.
158. Migot A., Guirgiutiu V. (2017) Impact localization on a composite plate with unknown material properties using pwas transducers and wavelet transform. *Proceedings of the ASME 2017 International Mechanical Engineering Congress and Exposition IMECE2017, November 3-9, 2017, Tampa, Florida, USA*, 70140.
159. Sung D.-U. et al. (2000) Impact Monitoring of Smart Composite Laminates Using Neural Network and Wavelet Analysis. *Journal of Intelligent Material Systems and Structures*, 11, 180-190.
160. Ciampa F., Meo M. and Barberi E. (2012) Impact-localization-in-composite-structures-of-arbitrary-cross-section. *Structural Health Monitoring*, 11(6), 643-655.
161. Dai B. et al. (2017) Improved terahertz nondestructive detection of debonds locating in layered structures based on wavelet transform. *Composite Structures*, 168, 562-568.
162. Pepelyshev Yu.N., Tsogtsaikhan Ts. (2015) Investigation of the pulse energy noise dynamics of IBR-2M using cluster analysis. *Annals of Nuclear Energy*, 83, 50-56.
163. Zhao G. et al. (2017) Localization of impact on composite plates based on integrated wavelet transform and hybrid minimization algorithm. *Composite Structures*, 176, 234-243.
164. Faria A.W., Silva R.A. and Koroishi E.H. (2017) Matrix Damage Detection in Laminated Composite Structures by Discrete and Continuous Wavelet Transforms Using Vibration Modes. *Journal of Aerospace Technology and Management*, 9(4), 431-441.
165. Kudela P. et al. (2007) Modelling of wave propagation in composite plates using the time domain spectral element method. *Journal of Sound and Vibration*, 302, 728-745.
166. González-Carrato R.R.H. (2014) Pattern recognition by wavelet transforms using macro fibre composites transducers. *Mechanical Systems and Sygnal Processing*, 48(1-2), 339-350.
167. Geng J. et al. (2018) Predicting dynamic response of stiffened-plate composite structures in a wide-frequency domain based on Composite

B-spline Wavelet Elements Method (CBWEM). *International Journal of Mechanical Sciences*, 144, 708-722.

168. Pahuja R., Mamidala R. (2018) Process monitoring in milling unidirectional composite laminates through wavelet analysis of force signals. *Procedia Manufacturing*, 26, 645-655.
169. Lu Q., Zhou W. and Zheng Y. (2022) Regenerative Braking Control Strategy with Real-Time Wavelet Transform for Composite Energy Buses. *Machines*, 10(8), 10080673.
170. Kharintsev S.S. et al. (2005) Resolution enhancement of composite spectra using wavelet-based derivative spectrometry. *Spectrochimica Acta Part A*, 61, 149-156.
171. Tsai D.-M, Chiang C.-H. (2002) Rotation-invariant pattern matching using wavelet decomposition*. Pattern Regonition Letters*, 23, 191-201.
172. Chen Z. et al. (2023) Stress–strain-based crack damage detection of composite structures using selective kernel convolutional networks and continuous wavelet transform. *Structural Health Monitoring*, 22(4), 2785-2799.
173. Amaravadi V. et al. (2002) Structural integrity monitoring of composite patch repairs using wavelet analysis and neural networks. *Proceedings of the SPIE*, 4701, 156-166.
174. Lyashenko V. et al. (2017) Study of composite materials for the engineering using wavelet analysis and image processing technology. *International Journal of Mechanical and Production Engineering Research and Development*, 7(6), 445-452.
175. Palmer S., Hall W. (2012) Surface evaluation of carbon fibre composites using wavelet texture analysis. *Composites Part B*, 43, 621-626.
176. Kallweit R.S., Wood L.C. (1982) The limits of resolution of zero-phase wavelets. *Geophysics*, 47(7), 1035-1046.
177. Sun J., Li H. and Xu B. The morphological undecimated wavelet decomposition – Discrete cosine transform composite spectrum fusion algorithm and its application on hydraulic pumps. *Measurement*, 94, 794-805.
178. Samaratunga D., Jha R. and Gopalakrishnan S. (2015) Wave propagation analysis in adhesively bonded composite joints using the wavelet spectral finite element method. *Composite Structures*, 122, 271-283.
179. Mitra M., Gopalakrishnan S. (2006) Wave propagation analysis in carbon nanotube embedded composite using wavelet based spectral finite elements. *Smart Materials and Structures*, 15, 104-122.
180. Jeong H, Jang Y.-S. (2000) Wavelet analysis of plate wave propagation in composite laminates. *Composite Structures*, 49, 443-450.
181. Shrestha R., Chung Y. and Kim W. (2019) Wavelet transform applied to lock-in thermographic data for detection of inclusions in composite

structures Simulation and experimental studies. *Infrared Physics & Technology*, 96, 98-112.

182. Sohn H. et al. (2004) Wavelet-based active sensing for delamination detection in composite structures. *Smart Materials and Structures*, 13, 153-160.
183. Guo K. et al. (2006) Wavelets with composite dilations and their MRA properties. *Applied and Computational Harmonic Analysis*, 20, 202-236.
184. Guo K. et al. (2004) Wavelets with composite dilations. *Electronic Research Announcements of the American Mathematical Society*, 10, 78-87.
185. Harbrecht H., Stevenson R. (2006) Wavelets with patchwise cancellation properties. *Mathematics of Computation*, 75(256), 1871-1889.
186. Zalevsky Z., Ouzieli I. and Mendlovic D. (1996) Wavelet-transform-based composite filters for invariant pattern recognition. *Applied Optics*, 35(17), 3141-3147.
187. Guerrier S. et al. (2013) Wavelet-Variance-Based Estimation for Composite Stochastic Processes. *Journal of American Statistical Association*, 108(503), 1021-1030.
188. Barouni A.K., Saravanos A. (2016) A layerwise semi-analytical method for modeling guided wave propagation in laminated and sandwich composite strips with induced surface excitation. *Aerospace Science and Technology*, 51, 118-141.
189. Feng B., Ribeiro A.L. and Ramos G. (2018) A new method to detect delamination in composites using chirp-excited Lamb wave and wavelet analysis. *NDT&E International*, 100, 64-73.
190. Chen X. et al. (2013) Composite Damage Detection Based on Redundant Second-Generation Wavelet Transform and Fractal Dimension Tomography Algorithm of Lamb Wave. *IEEE Transactions of Instrunentation and Measurement*, 62(5), 1354-1363.
191. Paget C. et al. (2003) Damage assessment in composites by Lamb waves and wavelet coefficients. *Smart Materials and Structures*, 12, 393-402.
192. Su C. et al. (2020) Damage assessments of composite under the environment with strong noise based on synchrosqueezing wavelet transform and stack autoencoder algorithm. *Measurement*, 156, 107587.
193. Lemistre M. et al. (1999) Damage localization in composite plates using wavelet transform processing on Lamb wave signals. *2nd International Workshop on Structural Health Monitoring, Stanford, 8-10 Sept. 1999*.
194. Tan K.S., Guo N. and Wong B.S. (1995) Experimental evaluation of delaminations in composite plates by the use of Lamb waves. *Composites Science and Technology*, 53, 77-84.

195. Wu J. et al. (2021) Lamb wave-based damage detection of composite structures using deep convolutional neural network and continuous wavelet transform. *Composite Structures*, 276, 114590.
196. Harb M.S., Yuan F.G. (2016) Non-contact ultrasonic technique for Lamb wave characterization in composite plates. *Ultrasonics*, 64, 162-169.
197. Su Z., Ye L. (2004) Selective generation of Lamb wave modes and their propagation characteristics in defective composite laminates. *Proceedings of the Institution of Mechanical Engineers Part L Journal of Materials Design and Applications*, 218(2), 95-110.
198. Alleyne D.N., Cawley P. (1992) The Interaction of Lamb Waves with Defects. *IEEE Transactions on Ultrasonics, Ferroelectrics and Frequency Control*, 39(3), 381-397.
199. Guo N, Cawley P. (1993) The interaction of Lamb waves with delaminations in composite laminates. *Journal of Acoustical Society of America*, 94(4), 2240-2246.
200. Badcock R.A., Birt E.A. (2000) The use of 0-3 piezocomposite embedded Lamb wave sensors for detection of damage in advanced fibre composites. *Smart Materials and Structures*, 9(291), 291-297.
201. Park H.W. et al. (2007) Time reversal active sensing for health monitiring of a composite plate. *Journal of Sound and Vibration*, 302, 520-66.
202. Staszewski W.J. et al. (1997) Wavelet signal processing for enchanced Lamb wave defect detection in composite plates using optical fiber detection. *Optical Engineering*, 36(7), 1877-1888.

INDEX